UNIVERSITÀ
DEGLI STUDI
DI PADOVA

Sede amministrativa: Università degli Studi di Padova

Dipartimento di Scienze Chimiche

Scuola di Dottorato in Scienza ed Ingegneria dei Materiali

XXII CICLO

Diffusion of Iron in Lithium Niobate

for Applications in Integrated Optical Devices

Direttore: Ch.mo Prof. Gaetano Granozzi

Supervisore: Dott.ssa Cinzia Sada

Dottoranda: Maria Vittoria Ciampolillo

Abstract

In the field of optical signal processing and all-optical integrated devices, photorefractive crystals can be used because of their capability to keep memory of a spatially varying light pattern. Among them, lithium niobate is particularly interesting because its photorefractive response can be improved or inhibited by adding selected dopants: this opens the possibility of producing an integrated device in a lithium niobate single crystal, where each stage has different properties and different functions according to the doping. In particular, a photorefractive stage can be created by doping with Fe, which is known to enhance photorefractive effect. In the context of integrated devices, it is necessary to perform a local doping of lithium niobate with Fe, in order to obtain a suitable substrate for photorefractive recording. This thesis deals with the preparation and characterisation of the locally doped crystal, i.e. with an investigation of the preparation conditions and how they affect the crystal quality. Many characterisation techniques, customary in materials science, such as secondary ion mass spectrometry, spectrophotometry and others, have been used and refined specifically for Fe doped lithium niobate. Besides the practical aim to find the best preparation conditions, many basic properties and features of this material have been investigated, leading to an advance in the knowledge of this material, as well as an advance in the usage of characterisation tools.

Nel campo del trattamento di segnali ottici e dei dispositivi ottici integrati, i cristalli fotorifrattivi sono impiegati per via della loro capacità di mantenere memoria di un *pattern* di luce. Tra questi, il niobato di litio è particolarmente interessante per via del fatto che la sua risposta fotorifrattiva può essere migliorata o inibita aggiungendo determinati droganti: è quindi possibile produrre, in un cristallo singolo di niobato di litio, un dispositivo integrato in cui ciascuna parte ha differenti proprietà e differenti funzioni a seconda del drogaggio. In particolare, si può realizzare una zona fotorifrattiva drogando con Fe, che come noto aumenta l'effetto fotorifrattivo. Nel contesto dei dispositivi ottici integrati, è necessario drogare localmente con Fe il niobato di litio per ottenere un substrato adatto alla registrazione fotorifrattiva. Questa tesi tratta la preparazione e la caratterizzazione del cristallo drogato localmente, studiando le condizioni di preparazione e come esse influenzano la qualità del cristallo. Molte tecniche di caratterizzazione abituali in scienza dei materiali, come la spettrometria di ioni secondari, la spettrofotometria ed altre, sono state utilizzate ed affinate specificamente per questo materiale. Accanto all'obiettivo pratico di trovare le migliori condizioni di preparazione, molte proprietà e caratteristiche di base di questo materiale sono state approfondite, progredendo sia nella conoscenza del materiale, sia nell'uso degli strumenti di caratterizzazione.

Contents

Introduction

Fast communications, data storage and sensors are nowadays rapidly growing fields which stimulates the search for new devices and technologies. In this scenario, systems based on an all-optical signal processing schemes are attracting more and more attention because they have the potential to overcome the speed and size limits of standard electronic technology. Devices based on nonlinear light interactions are therefore of great interest and are currently object of intense study; in particular photorefractive effect, which consists of a refractive index change induced by inhomogeneous illumination, offers a promising way to realise a whole range of all-optical devices because it can be exploited in the realisation of optical memories, holographic gratings, phase conjugated devices and many other systems [1].

Photorefractive effect is due to excitation, migration and trapping of electrons giving rise to a local electric field, which in turn changes the refractive index by means of electro-optic effect. Since refractive index changes can be permanently written on the material, this effect can be exploited for permanent holographic gratings and many other applications. So far, most of the photorefractive devices are based on free propagation of light. However, concrete technological applications require the integration of optical circuits in a single substrate, where the optical signal propagates in waveguides. The integration of optical circuits on a single chip leads to reduction of the device size and of the optical power required, together with a better efficiency. It is therefore clear that the realisation of integrated photorefractive devices relies on the development of suitable optical materials and processes, whose exploitation requires a deep understanding of their structure at microscopic level.

Among photorefractive crystals, lithium niobate ($LiNbO_3$) plays a lead role because of its commercial availability and its many properties suitable for integrated optics. Photorefractive effect occurs in pure lithium niobate crystal, but can be greatly enhanced by doping with certain transition metals, among which the most used is iron. Fe:$LiNbO_3$ is sensitive to light in the visible green or blue wavelength region, but shows only little effects in the red or near infrared spectral region. Especially in the 1.3 μm and 1.55 μm wavelength band of optical communications no photorefractive effects have been observed for common continuous wave intensities. This allows the use of a light beam at visible wavelengths to "write" the material and eventually control the optical signal, which is transmitted in the infrared region, avoiding the erasure of the refractive index pattern. In $LiNbO_3$ (LN) iron can exist in two valence states, Fe^{3+} and Fe^{2+}, whose energy levels are located in the middle of the bandgap. Illumination promotes ionisation of Fe^{2+} to Fe^{3+}, then electrons migrate towards non-illuminated regions of the material by diffusion and photovoltaic effect and finally they are trapped again by Fe^{3+}. The optimization of the photorefractive response of the material is therefore primarily connected to the capability of controlling the total number of Fe impurities and their valence state.

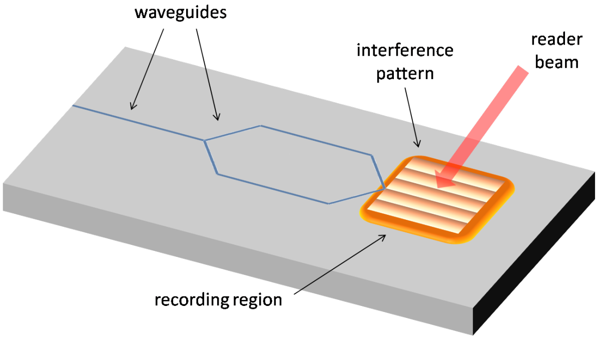

Figure 1: Scheme of a single-crystal optical device for holographic recording based on photorefractive effect. The interference pattern generated by two waveguided beams is recorded on a photorefractive planar waveguide.Fe doping is required only in the recording region.

For what concerns the realization of an integrated optical device in a single lithium niobate crystal, where different stages have different functions, the above mentioned requirements are to be fulfilled in a local fashion: thus, by doping locally with the proper element, different properties can be obtained on different parts of a crystal according to the properties provided by the dopant. In order to create a photorefractive stage in an integrated device, it is necessary to increase locally the concentration of photorefractive dopants, for instance by in-diffusion of thin deposited metal layers at high temperatures. The thermal diffusion doping technique takes advantage of the loosely-packed crystal structure of LN which results in relatively high diffusivity of impurities in this material. This technique is favourable for integrated optics because commercially available undoped LN wafers may be used. A desired region can be locally doped, whereas the rest of the substrate remains unchanged: this technology is already exploited for commercial optical modulators based on Ti:LN waveguides.

Even if the optical properties of photorefractive waveguides have been investigated by many authors [1], published literature is essentially devoted to the study of the optical properties of waveguides, without a deep understanding of the structural properties of the material at the atomic level. In particular very few works [2] explore the in-diffusion process of photorefractive dopants such as Fe from a material point of view. The aim of this work is to investigate the local doping of lithium niobate with Fe by thermal diffusion from thin film, considering both the preparation conditions and the characterisation of the doped crystal, with the aim of optimising this system for photorefractive applications. As a concrete technological application, the feasibility of a prototype of integrated phorefractive device with planar geometry, able to record a light pattern produced by two interfering beams, will be considered. An example of such device, which presents the typical requirements of an integrated device with a photorefractive stage, is shown in figure 1: two waveguides inject light in a planar waveguide (square-shaped) with photorefractive properties, where the two beams diffract and interfere giving rise to a pattern of light intensity, recorded by the crystal. The interference pattern can be read in a second moment by a reader beam. In the device, made of a LN single crystal, channel and planar waveguides are realised by means of ion implantation; the recording region is made photorefractive thanks to Fe doping. A local doping with Fe is thereby needed, in such way that dopant is present only in the square-shaped region, and its distribution is homogeneous inside the planar waveguide: thermal diffusion from thin film is the chosen doping technique. The aim of this work is to dope locally LN crystals in order to obtain a photorefractive region with the required properties.

The work was focused particularly on studying the preparation conditions and how they affect the quality and the properties of the doped crystal, defining the best processing conditions, and lastly evaluating the feasibility of the device.

The first task was to study the structural and compositional properties of the doped surface. In order to simplify those characterisations, a series of samples was doped with Fe on the whole surface, and not only in the photorefractive region. After, as a second task, Fe doping was made, with suitable masking methods, only in a square-shaped region. The properties of the samples produced were investigated by a number of complemetary characterisation techniques: Secondary Ion Mass Spectrometry (SIMS) to obtain a depth-resolved compositional characterisation for studying the diffusion process; UV-visible and IR spectrophotometry to characterise the Fe valence state and the hydrogen content; High-Resolution X-Rays Diffraction (HRXRD) to gain information about lattice quality; Rutherford Backscattering (RBS) for quantitative measurements of Fe amount; micro Raman spectroscopy and polaron luminescence for investigating the effect of Fe doping on lattice vibration and defects; Proton-induced X-ray Emission (PIXE) for lattice site location of Fe. In particular the author took care of the entire sample preparation and characterisation by means of SIMS and UV-vis-IR spectrophotometry. The other measurements were performed by collaborators: HRXRD by M. Bazzan and A. Zaltron, RBS by M. Bianconi and N. Argiolas, PIXE by N. Argiolas and D. De Salvador, AFM by N. Argiolas, Raman and polaron luminescence by S. Mignoni and M. Fontana. Since the results from those techniques are tightly connected to SIMS and spectrophotometry, they are briefly discussed, with the aim to give a thorough description.

The results obtained in this study widen and enrich the knowledge of the Fe-doped lithium niobate system, both from the standpoint of basic understanding of its features and for practical applications. Concerning basic features, the kinetics of the diffusion process has been investigated, estimating the activation energy and the diffusion coefficient in a wide range of temperatures, and discovering a new crystalline phase; the importance of the atmosphere surrounding the sample during diffusion and the role of hydrogen and water vapour have been evidenced; the structural properties of the doped layer have been investigated, discovering a relation between lattice deformation and reduction degree. Concerning the practical aim of local doping, the best processing conditions have been defined. Advances have also been done concerning the characterisation techniques: a new method for quantification of Fe in lithium niobate, based solely on optical absorption, has been set up; different measurement strategies for compositional analysis of lithium niobate with SIMS have been experimented.

This work has been supported by the University of Padova, Progetto di Ateneo CPDA073231/07, “Doping and microstructuration of lithium niobate crystals for holographic recording in integrated optics”.

Chapter 1

Lithium niobate

Lithium niobate does not exist in nature: it was synthesised for the first time in 1928 then in 1949 its ferroelectricity was discovered. The first Czochralski growths of crystalline $LiNbO_3$ gave start to a systematic study of its properties.

In this chapter the fundamental properties, necessary to understand the following chapters, are briefly described.

1.1 Phase diagram

$LiNbO_3$ is one of the four compounds obtainable starting from Li_2O and Nb_2O_5: $Li_2Nb_{28}O_{71}$, $LiNb_3O_8$, $LiNbO_3$ and Li_3NbO_4. Apart from $LiNbO_3$, only $LiNb_3O_8$ was produced and characterised as a single crystal. The phase diagram of the system Li_2O - Nb_2O_5 is shown in figure 1.1; $LiNbO_3$ is a variable composition phase. As the diagram shows, $LiNbO_3$ crystallises from the melt in a wide interval of Li_2O molar percentage (between 37 % and 60 %). Moreover, there is a wide composition interval in which $LiNbO_3$ exists as a single phase, spreading towards percentage below 50 %.

In the above mentioned interval there is a certain composition for which the solid crystallising from the melt has the same composition as the melt itself: this is called congruent composition and corresponds to the maximum melting temperature (1253 °C), called congruent melting temperature. For $LiNbO_3$ the congruent composition differs from stoichiometry: the percentage of Li_2O is 48.38 mol%.

1.2 Crystal structure

From the crystallographic point of view lithium niobate belongs to the trigonal system, to the ditrigonal pyramidal class 3m, space group R3c. This is one of the ten classes which possess at least one polar axis, necessary requirement for ferroelectricity. Two choices of lattice cell are convenient: hexagonal cell and rombohedral cell. From the standpoint of atoms arrangement, oxygen atoms form a slightly distorted hexagonal close packed structure. Each hexagonal cell contains six oxygen planes perpendicular to Z axis. The oxygen structure can also be viewed as a net of linked octahedra, containing cationic sites. One third of the octahedra are filled with Li, one third with Nb, one third is vacant.

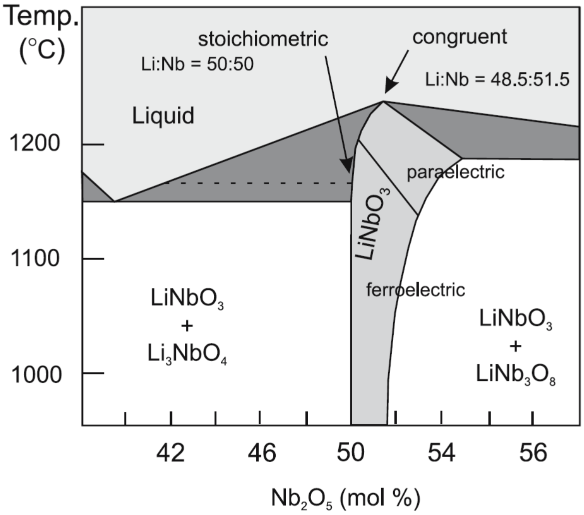

Figure 1.1: Phase diagram of the Li_2O - Nb_2O_5 system [3].

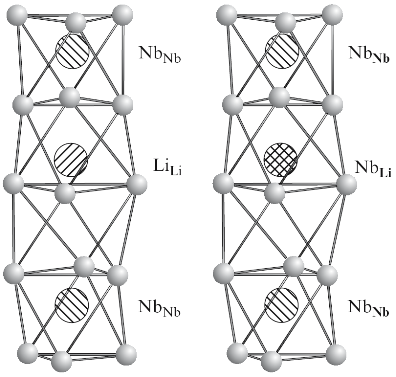

Figure 1.2: Ideal sequence of occupation in the octahedral sites (left) and antisite defect Nb_{Li} (right) [3].

1.2.1 Intrinsic defects

As already mentioned, lithium niobate congruent composition suggests that deviation from stoichiometry is energetically favoured: therefore there is a Li deficient crystalline configuration particularly stable, at least near melting temperature. This configuration accommodates some kind of defects to account for lithium deficiency. The knowledge of the configuration of these intrinsic defects is fundamental to understand transport properties and impurities arrangement. During the last 40 years of research on lithium niobate, several models of defective crystalline structures have been proposed, but none of them has been definitively confirmed by experimental data yet.

The most accounted model is the *lithium vacancy model*, which places some Nb atoms on the Li site (niobium antisite Nb_{Li}) to compensate charge unbalance, according to the following unit formula:

$$\{[\mathrm{Li}]_{1-5x}[\mathrm{Nb_{Li}}]_x[\mathrm{V_{Li}}]_{4x}\}\{[\mathrm{Nb_{Nb}}]\}\mathrm{O}_3$$

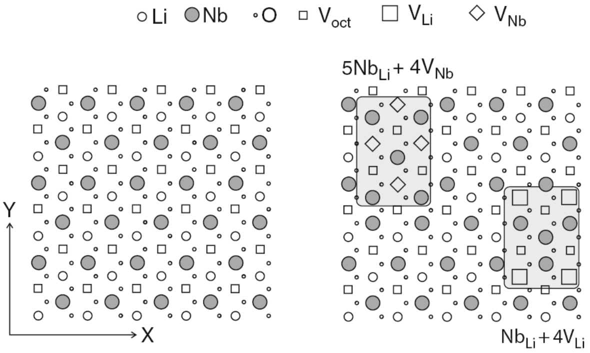

Figure 1.3: Projection on the (001) plane of ideal lithium niobate structure (left) and structure with intrinsic defect Nb_{Li} evidencing two different arrangements for charge compensation (right) [3].

where curly brackets are used to close off Li sublattice and Nb sublattice. Since in congruent $LiNbO_3$ the ratio [Li]/[Nb] equals 0.94, $x = 0.01$ in the latter formula. Another model less welcomed is the *niobium vacancy model*, in which charge compensation is accomplished by filling all Li vacancies with Nb_{Li}, according to the following formula:

$$\{[\mathrm{Li}]_{1-5x}[\mathrm{Nb_{Li}}]_{5x}\}\{[\mathrm{Nb_{Nb}}]_{1-4x}[\mathrm{V_{Nb}}]_{4x}\}\mathrm{O}_3$$

where x has the same value as before. Since truth is often in the middle, the coexistence of Li and Nb vacancies was proposed [4] according to the formula:

$$\{[\mathrm{Li}]_{1-5x}[\mathrm{Nb_{Li}}]_{5x-w}\}\{[\mathrm{Nb_{Nb}}]_{1-w}[\mathrm{V_{Nb}}]_{w}\}\mathrm{O}_3$$

where the only condition on w is $w < 4x$.

Local arrangements of intrinsic defects are schematised in figure 1.3: both the arrangements evidenced in the right part of the figure involve the presence of two Nb atoms in two neighbouring octahedral sites, which is particularly important for the electronic properties, as explained in the following section.

1.3 Electronic properties

Lithium niobate, with its 3.72 eV bandgap, can be classified as an insulating material. Its conductivity at room temperature is normally very low (10^{-18} - 10^{-16} $(\Omega\mathrm{cm})^{-1}$). For the oxidised crystal, from room temperature to 1000 °C, conductivity is due to transport of protons incorporated as impurities in the crystal matrix: the activation energy is about 1 eV and the conductivity results proportional to hydrogen concentration. When LN is doped with metal ions, another transport mechanism concurrent to protonic conductivity arise, namely electron tunneling via impurity sites. When the crystal is reduced, electronic conductivity is greatly increased due to formation of the so called bipolarons, as described in the following section.

1.3.1 Polaron, bipolaron

A polaron state is formed by coupling of an electron with the host phonons, the local deformation produced by the electron serves as potential well for the electron itself. Polarons can be distinguished in large polarons and small polarons. In the former

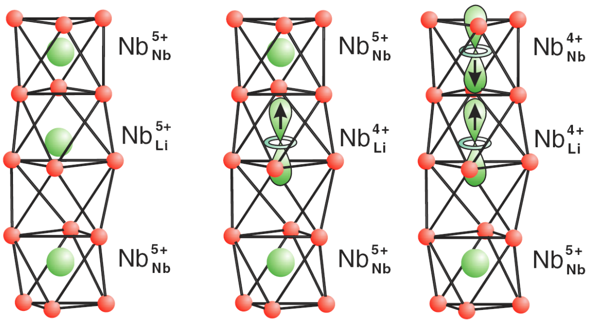

Figure 1.4: Scheme of the crystal structure surrounding a Nb antisite (left), a bound polaron (centre) and a bipolaron (right) [5].

case, the deformed region is larger than the lattice constant, and the polaron can be regarded as a free electron with a large effective mass, moving via band transport; in the latter case the coupling is stronger, the polaron radius is within a lattice site and the movement occurs by hopping. If the host contains charged defects, the polaron localises at defect sites, forming a bound small polaron. There are several experimental evidences that in lithium niobate bound polarons are formed on the antisite defect $\mathrm{Nb_{Li}}$ [5]. Polarons are created after annealing of congruent lithium niobate in inert or reducing gas according to the following mechanism:

$$3\mathrm{O}^{2-}_{\mathrm{O}} + 2\mathrm{V}_{\mathrm{Li}} + \mathrm{Nb}^{5+}_{\mathrm{Nb}} \leftrightarrow \frac{3}{2}\mathrm{O}_2 + \mathrm{Nb}^{4+}_{\mathrm{Li}} + 5\mathrm{e}^- \tag{1.1}$$

in which a unit formula of $\mathrm{LiNbO_3}$ disappears due to loss of oxygen and redistribution of $\mathrm{V_{Li}}$ and $\mathrm{Nb_{Li}}$. The released electrons are trapped by Nb. Polarons are responsible for absorption bands in the visible spectral region, which raise after reduction. Polarons are also invoked in the interpretation of the short-living electronic states arising in LN under intensive photoexcitation. The polaron model is confirmed by the following experimental observations: the density of LN increases after reduction, consistently with oxygen loss and rearrangement of cationic sublattice[1]; the intensity of the polaron absorption band strongly decreases in Li-enriched crystals, because the lack of Li vacancies inhibits the antisite formation. The polaron itself however cannot explain all the features in absorption spectra. The electrons released thanks to reaction 1.1 are captured by pre-existing or newly formed complexes $\mathrm{Nb_{Nb}} - \mathrm{Nb_{Li}}$ (shown in figure 1.4) to form a diamagnetic electron pair bound state, the bipolaron. The formation of a bipolaron is an energetically favourable self-stabilisation of an electron pair. In this framework, the broad band at 2.5 eV in the absorption spectrum is due to dissociation of a bipolaron, i.e. transfer of one of the paired electrons from the bipolaron to an isolated polaron, whereas the metastable band at 1.6 eV ascribed to optical transfer of an electron from $\mathrm{Nb^{4+}_{Li}}$. Thus the shape of absorption spectrum in the absence of strong illumination depends on temperature, which regulates the equilibrium between relative concentrations, as evidenced by the absorption spectra taken at different temperatures shown in figure 1.5: from the temperature dependence

---

[1] If there was no rearrangement of cationic sublattice, the density, as a consequence of oxygen loss, would decrease.

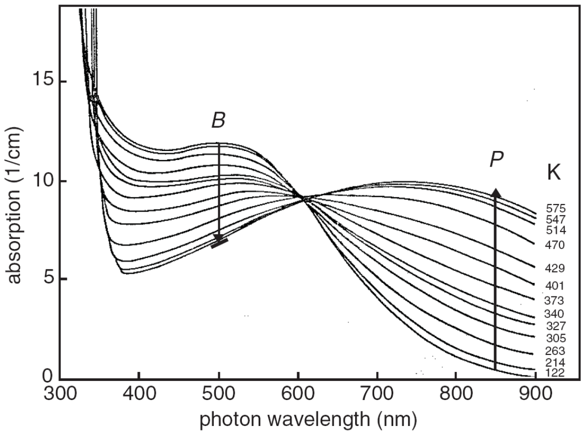

Figure 1.5: Absorption spectra of reduced lithium niobate at different temperatures, showing the decrease of bipolaron band B and the raise of polaron band P with increasing temperature [5].

of the turnover between bands, the bipolaron dissociation energy was determined to be about 0.3 eV.

1.3.2 Electronic transitions

Lithium niobate, in its oxidised state, is transparent in all the visible and near-IR region, and shows an absorption band edge in the UV, due to valnce band - conduction band transition. LN is birefringent due to its uniaxial crystal symmetry. Birefringence is negative, i.e. the extraordinary refractive index (which refers to light propagating along Z axis) is smaller than the ordinary one. The position of the edge is established, using the criterion of Kovács et al. [6], as the wavelength for which $\alpha = 20$ cm^{-1}. The expected position for congruent lithium niobate is about 320 nm for both polarisations [6].

1.3.3 Photorefractive effect

Photorefractivity means refractive index changes induced by illumination, as a result of electro-optic effect and photoconductibity. An electric field applied to an electro-optic material produces changes in its refractive index, a phenomenon also called Pockels effect. On the other hand, photoconductivity means that light of adequate wavelength is able to produce electric charge carriers that are free to move by diffusion and also by drift under the action of an electric field. The light excites charge carriers from localised states (photoactive centres) in the forbidden band gap to extended states (conduction or valence bands) where they move, are retrapped and excited again, and so on. During this process, in the case of non-homogeneous illumination, the charge carriers progressively accumulate in the darker regions of the sample. In this way, charges of one sign accumulate in the darker regions while leaving charges of the opposite sign in the brighter regions. This spatial modulation of charges produces an associated space-charge electric field (figure 1.6). The combination of both effects gives rise to the so-called photorefractive effect: the light produces a photoconduction-based electric field spatial modulation that in turn produces a refractive index modulation

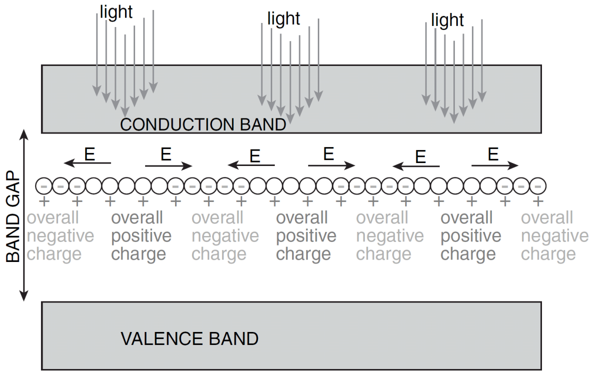

Figure 1.6: In a photoconductive crystal the charge distribution induced by inhomogeneous illumination produces a space-charge electric field modulation [7].

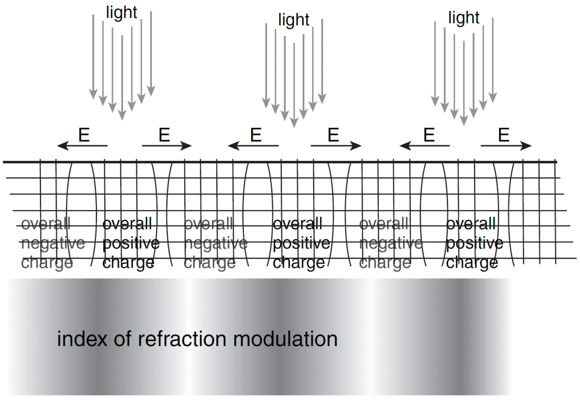

Figure 1.7: If the photoconductive material is also electro-optic, the space-charge field produces an index of refraction modulation in the crystal volume [7].

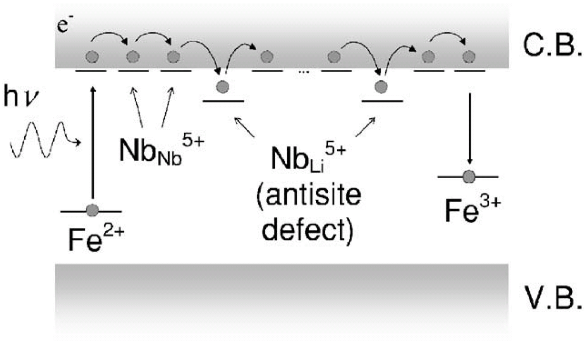

Figure 1.8: Schematics of the light induced electron excitation, transport across the lattice, and trapping at $\mathrm{Nb_{Li}}$ or $\mathrm{Fe^{3+}}$ [8].

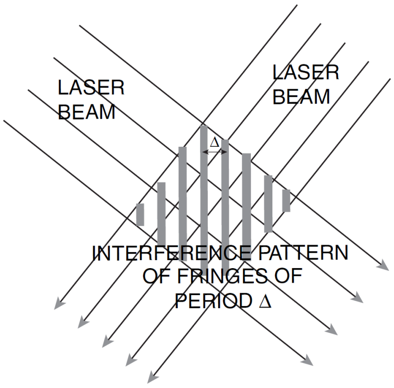

Figure 1.9: Generation of an interference pattern of fringes [7].

via the electro-optic effect, as schematised in figure 1.7. This change can be reversed by the action of light or by relaxation even in the dark.

The deep trap centres in pure lithium niobate are known to be Fe^{3+} and Fe^{2+} impurities: Fe^{2+} acts as an electron donor whereas Fe^{3+} acts as electron trap. Also other transition metals, whose energy levels locate in the middle of the band gap, act the same way, for instance Cu^{+} and Cu^{2+}. Also the polaron plays a role in photorefractive effect in LN, hence it is generally described in terms of the so called two centre model [9]: two different photorefractive centres are considered. The first centre is a deep-level impurity, namely Fe^{2+}/Fe^{3+}, and the second one is more shallow with respect to the valence band edge, namely polaron level Nb^{4+}/Nb^{5+}, each centre occurring in two different valence states. Excitation of electrons into the conduction band and recombination with free conduction band electrons are possible at both centres. Upon illumination electrons are excited from deep centres into the conduction band. These electrons migrate in the conduction band and are captured either by deep or shallow centres, as schematised in figure 1.8. Because of the low thermal activation energy, electrons are easily re-excited at shallow centres and the concentration of filled shallow traps remains small. With increasing light intensity more and more electrons are excited from deep centres and trapping at the shallow centre produces a higher Nb^{4+} concentration.

By way of simple example of application of photorefractive effect, when two laser beams interfere, an interference pattern is written in the material by means of refractive index changes (figure 1.9). After illumination is switched off, the refractive index changes decay because of dark conductivity, which restores an homogeneous charge distribution. As already mentioned, dark conductivity is due to proton transport and electron tunneling between Fe^{3+} ions. As a consequence, for permanent memory applications, Fe^{3+} concentration must be less than 0.1 mol

In order to avoid erasure of refractive index patterns, a procedure commonly called thermal fixing is employed [10]: it consists in heating the crystal during or after illumination. At enhanced temperatures, if the hydrogen concentration is large enough (comparable to the concentration of filled traps) protons migrate to compensate the electric space-charge field. After cooling the crystal to room-temperature, the concentrations of filled and empty traps maintain the modulation previously induced during illumination thanks to proton compensation. Under homogeneous illumination, spatially modulated currents arise because of spatially modulated concentrations of filled traps, hence space charge fields and refractive index modulations arise. Thus after thermal fixing homogeneous illumination develops the stored refractive-index pattern [10].

1.4 Lattice vibrations

Lithium niobate crystal belongs to the R3c space group, with two formula units per unit cell. Accordingly, 18 vibrational modes at zero wavevector are decomposed into $4A_1 + 9E + 5A_2$, where A_1 refers to symmetric one-dimensional irreducible representation, E to two-dimensional irreducible representations, and A_2 to anti-symmetric irreducible representations of the lattice vibrations. Whereas A_2 modes are Raman inactive, A_1 and E modes are both Raman and infrared active. A_1 modes are polarised along the Z axis, whereas the doubly degenerate E modes correspond to ionic motions in the XY plane.

1.4.1 OH^- stretching

$LiNbO_3$ growth from the melt is usually carried out in air: air always contains a certain degree of humidity, from which OH^- ions are incorporated into the lattice. Crystals grown under different atmospheres contain different OH^- concentration ($10^{18} \div 10^{20}$ cm^{-3}) [11]. Hydrogen can also be introduced into the lattice by annealing in water-vapour rich atmosphere; on the contrary, hydrogen can be removed from the lattice by annealing in dry atmosphere. The easiest way to characterise the presence of OH^- is to exploit the infrared absorption band arising from OH^- stretching bond. This band is found to peak at about $3500\,cm^{-1}$, the exact energy position depending on stoichiometry, doping, production method. It is strongly polarised perpendicular to the ferroelectric axis, that means, the direction of the bond lies on the oxygen plane. In congruent crystal the band has a complex structure (the major component peaks at $3482\,cm^{-1}$), interpreted in terms of several non-equivalent lattice positions. Several dopants are reported to shift the band position, likely because they form an OH^- - impurity complex that changes the OH^- local environment. The measurement of the absorption cross section presents several problems, so the OH^- concentration can not be easily measured through intensity of the OH^- stretching band.

1.5 Iron doping

As already mentioned, in Fe doped $LiNbO_3$ iron can assume two valence states: Fe^{2+} and Fe^{3+}. Photorefractive effect occurs also in nominally pure LN, because even few ppm of Fe impurities are sufficient; intentional doping has been widely employed to enhance photorefractive properties. Most of the data available concern bulk doped Fe:LN.

1.5.1 Lattice position of iron

Many works assert that Fe^{3+} substitutes for Li in bulk doped LN. Simulation of EXAFS spectrum of Fe on Li site [12] was consistent with experimental spectrum, and showed no difference between Fe^{2+} and Fe^{3+}; X-ray standing waves method applied on four reflections [13] allowed to determine the exact position of Fe ions, 0.18 Å above the Li position in ferroelectric phase, along the Z crystallographic axis. Also ion beam

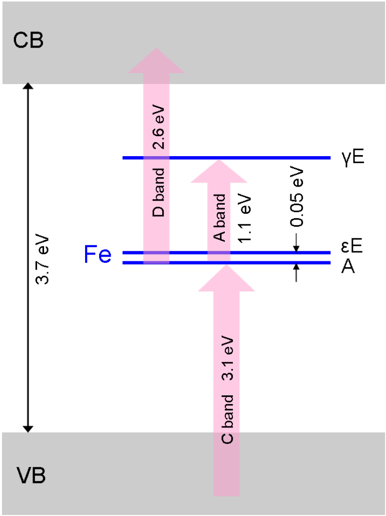

Figure 1.10: Energy level diagram of Fe:LN. Trigonal field splits *d* orbitals of Fe into three levels in the middle of the gap, which are involved in optical transitions A, C, D.

transition	E ∥ Z	E ⊥ Z
$A \rightarrow \epsilon E$	forbidden	allowed
$A \rightarrow \gamma E$	forbidden	allowed
$\epsilon E \rightarrow A$	forbidden	allowed
$\epsilon E \rightarrow \gamma E$	allowed	allowed

Table 1.1: Selection rules for transitions involving Fe orbitals in LN [15].

analysis in channeling conditions, combined with PIXE and nuclear reaction, ensured that Fe locates mainly of Li site [14].

1.5.2 Effect of iron on optical properties

The first analysis and explanation of optical absorption in bulk doped Fe:LN by means of crystal field theory is due to Clark et al. [15]. Iron lies in an octahedral site on the three-fold symmetry axis: oxygen octahedra are slightly distorted, so the exact point symmetry is C_3 with only small distortion from C_{3v}. An octahedral crystal field splits degenerate d levels of iron into two levels, a threefold degenerate level T and a twofold degenerate level E. Crystal fields are not strong in these sites, therefore high spin configurations will be preferred. Due to trigonal perturbation, T splits into two levels, E (twofold degenerate) and A, according to C_3 point symmetry: to distinguish the two E levels, the notation γE and ϵE (referring to γ - type and ϵ - type d orbitals) is used. These energy levels are located within the wide energy gap of lithium niobate and can be involved in photon induced electronic transitions, as schematised in figure 1.10. Selection rules for electric-dipole transitions are shown in table 1.1: among them, only the transition $A \rightarrow \gamma E$ is experimentally observed.

The principal features of the absorption spectra of Fe^{3+}:$LiNbO_3$ and Fe^{2+}:$LiNbO_3$ are shown in figure 1.11 (nomenclature according to [16]):

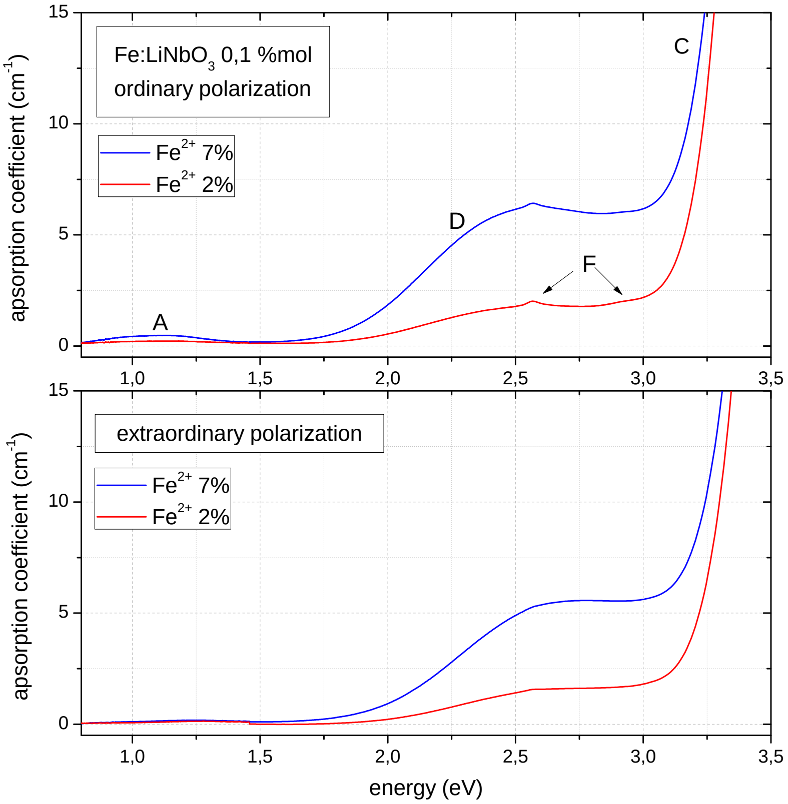

Figure 1.11: Absorption spectra of bulk iron doped lithium niobate, in both polarisations. A and D bands are ascribed to Fe^{2+}, whereas F bands are ascribed to Fe^{3+}.

- for both valence states, UV absorption edge shifted with respect to pure congruent $LiNbO_3$ to higher wavelength (340 nm instead of 310 nm). This absorption is attributed to charge transfer from valence band to an iron d level, the transition energy being 3.10 eV, lower than the energy gap of 3.8 eV. The peak of this absorption band (band C) is not visible due to large intensity and the band is not distinguishable from the energy gap band;
- only for Fe^{2+}, a wide band (D band), more intense in ordinary polarisation, centred at about 2.55 eV, which was attributed to intervalence transfer from Fe^{2+} to Nb^{5+};
- only for Fe^{3+}, ordinary polarisation, two weak narrow bands at 2.57 eV and 2.91 eV (F bands) due to spin forbidden d → d transitions of Fe electrons;
- only for Fe^{2+} a weak band at about 1.1 eV (A band), more intense in ordinary polarisation, attributed to A $\rightarrow \gamma$E transition (should be forbidden in extraordinary polarisation, it is probably allowed thanks to vibronic coupling).

Clark et al. observed qualitatively that the intensity of the wide band at 477 nm (2.55 eV) is roughly linear in Fe^{2+} concentration. Quantitative characterisation is due to the fundamental work by Kurz et al. [17], who compared experimental results obtained from different techniques to find relations between concentration and measured properties. From these data an absorption cross section of Fe^{2+} was calculated [18] for ordinarily polarised light at 477 nm ($\frac{1}{\sigma} = 2.16 \times 10^{21} \mathrm{m}^{-2}$); other authors [19] use the ordinary absorption coefficient at 532 nm to determine the Fe^{2+} absolute concentration. Other authors [20] exploited also the intensity of the narrow band at 483 nm (2.57 eV) to estimate the Fe^{3+} concentration, which combined with the intensity of the Fe^{2+} band at 532 nm should provide a way to determine the total Fe concentration. However they considered a set of only three samples and their method, calibrated on two of three samples, was unsuccessful when applied to the third one: as a consequence it is considered unreliable.

Chapter 2

Iron-diffused LN samples preparation

This chapter concerns the preparation of iron-diffused samples starting from commercial pure lithium niobate wafers. First a metallic thin film of iron was deposited on the polished surface of wafers, then an annealing was performed to obtain diffusion of the deposited metal inside the substrate.

2.1 Magnetron sputtering deposition

The deposition of an iron thin film on lithium niobate X-cut wafers was performed with magnetron sputtering technique. It consists in depositing on a substrate atoms sputtered from a target by means of accelerated ions in a vacuum chamber. Ions are supplied by the inert (or reactive) gas introduced in the chamber, and are accelerated towards the target thanks to the negative potential applied to it. The magnetic field generated by permanent magnets under the target traps the trajectories of secondary electrons close to the target, thus enhancing ionisation of the plasma and leading to higher sputter rate. The sputtered neutral atoms, unaffected by magnetic and electric field, deposit on the substrate, thus creating a film.

2.1.1 Apparatus description

The sputtering apparatus of our laboratory was made by Thin Film Technology. The cylindrical vacuum chamber is equipped with two sources, one DC magnetron for metallic targets and one RF magnetron for semiconducting targets. Vacuum is provided by a double stage vacuum system: a primary rotary pump and a turbomolecular pump.

2.1.2 Apparatus modification

The DC magnetron of our sputtering apparatus is not suitable for a ferromagnetic target. Indeed, a ferromagnetic target such an iron one affects the magnetic field generated by magnets so that the magnetic confinement of plasma no longer occurs. Ferromagnetic targets require a special magnets configuration which takes into account the target influence and generates resultant field lines that allow plasma confinement.

It was chosen not to modify magnets configuration, it was rather preferred to modify the geometry of the other pieces. Indeed it suffices to use a thinner target, thin enough to let some field lines exit from the target to succeed in confining plasma, and to modify the geometry of the target's clamp ring and ground shield. A 0.9 mm thick, 99.98 pure Fe target from Testbourne was used.

2.1.3 Process characterisation

The new iron source implementation was followed by an investigation on many aspects of the iron deposition process. Such investigation involved:

- pressure required for switching on/operation of the plasma;
- power operation range of the source;
- distance between target and samples;
- inclination of the target;
- rotation of the sampleholder.

Once all these parameters have been optimised, the final characterisation concerns the determination of time-thickness relation, i.e. the deposition rate. The deposition duration should not be too short, otherwise the sources of uncertainty (instants required for opening or closing the shutter) gain importance. On the other side, the longer the deposition lasts, the higher is the content of impurities inside the film (for instance, oxygen as residual gas brings about deposition of a certain percentage of iron oxide). Therefore the deposition rate must be properly chosen, and since it depends on all the above mentioned parameters, they must be carefully optimised.

Many test depositions were made to improve the process conditions. At last, it was found that

- plasma can be switched on at pressure no lower than about 1.5×10^{-5} bar;
- after ignition, plasma is sustainable at much lower pressure (until 4×10^{-6} bar);
- at 5×10^{-3} bar, the minimum power to sustain plasma is about 6 W, while the maximum power is limited by the maximum potential difference supplied by the generator (800 V), and by unwanted heating of the source;
- the optimum position of the sampleholder is the one closest to the source (the distance between target and sample is about 4 cm);
- rotation of the sampleholder is necessary to improve homogeneity.

The optimal inclination of the target is determined as the one which allows the most homogeneous thickness distribution. To this aim, systematic test depositions on small samples placed in different points of the sampleholder were performed, then the samples thickness was measured. The optimal inclination was chosen as the one which gives samples with the same thickness at least in the central part of the sampleholder. With rotation of the sampleholder, it sufficed to place the samples at different radii. Given the optimal distance from the target, the optimal inclination of the target that was found allows for homogeneous thickness within a diameter of about 5 cm in the centre of the sampleholder.

deposition time s	Fe fluence $\times 10^{15}$ at/cm^2	thickness nm	density $\times 10^{22}$ at/cm^3	pressure before deposition $\times 10^{-9}$ bar
120	51 ± 2	8.3 ± 0.2	6.2 ± 0.3	1.7
240	104 ± 3	14.8 ± 0.5	7.0 ± 0.3	2.0
180	73 ± 2	12.2 ± 0.3	6.0 ± 0.2	6.3
300	129 ± 3	21.4 ± 0.1	6.0 ± 0.2	7.0
158	67 ± 2	13.1 ± 0.2	5.0 ± 0.2	7.7
160	65 ± 2	9.5 ± 0.2	6.9 ± 0.2	1.2
160	73 ± 2	10.7 ± 0.1	6.8 ± 0.2	1.0
60	29 ± 1	6.6 ± 0.4	4.4 ± 0.3	1.8

Table 2.1: List of results of RBS and thickness measurements. The uncertainty on density values is calculated from propagation of the experimental error on fluence and thickness.

2.1.4 Experimental procedure

Samples are cut from commercial (purchased from Crystal Tech.), two face polished wafers of X-cut congruent lithium niobate, with thickness 1 mm and diameter 76 mm. Rectangular samples are obtained, whose dimensions depend on the purpose. Samples were treated with hydrofluoric and nitric acid for few minutes to remove residues from cutting, then immersed for few minutes in acetone in ultrasonic cleaner, and finally cleaned with 2-propanol. Samples are then fixed on the sampleholder just by steel springs.

Apart from test depositions, samples were deposited one at a time, placed at the centre of the sampleholder. After the chamber has reached the best vacuum as possible, typically 10^{-9} bar, it was filled with pure Ar (pressure $p = 5 \times 10^{-6}$ bar) and the plasma was switched on. The target was typically presputtered for 1 -2 minutes with a shutter covering it, then the shutter was opened and the sample was exposed to plasma while rotating, to get a better homogeneity. After deposition, the chamber was vented with Ar.

2.2 Iron thin film characterisation

The deposited film was characterised to gain information about its properties. These properties must be investigated because they may someway affect the diffusion process. In particular thickness, density and roughness were investigated.

2.2.1 Rutherford backscattering

Samples underwent Rutherford Backscattering (RBS) measurements in order to quantify the deposition rate of iron. For a description of the technique and data analysis, see appendix C.

Seven samples with different amounts of iron, i.e. different deposition time, were measured to obtain a calibration between iron fluence (the number of deposited atoms per unit area, or areal density) and deposition time. Results are listed in table 2.1 and plotted in 2.1. Data are well fitted by a line, whose intercept is compatible with zero: the deposition rate given by the fit is $(4.15 \pm 0.02) \times 10^{14}$ atoms/(cm^{2}s).

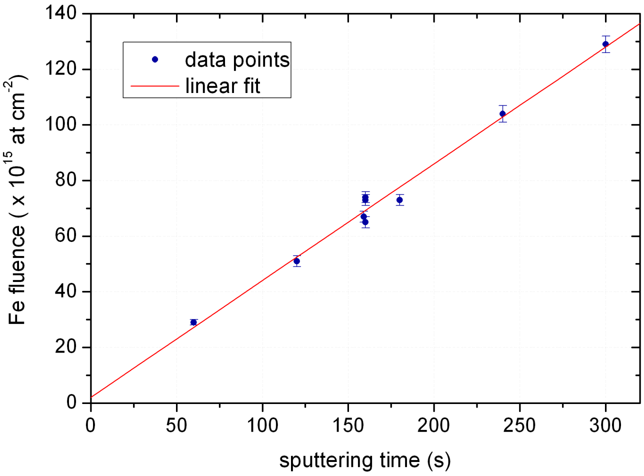

Figure 2.1: Fe fluence, measured by RBS, plotted vs sputtering time. Experimental data are linearly fitted.

2.2.2 X-ray reflectivity

This technique, described in appendix D, was used for measuring the iron film thickness with the aim of checking the homogeneity of the film and the proportionality between thickness and deposition time. Its results can be used together with RBS results to determine the film density and to check if density depends on experimental conditions. Thickness data are reported in table 2.1 together with calculated density. Whereas there is a linear relation between fluence and deposition time, thickness and deposition time are not linearly related. As a consequence, the density varies from one sample to another. A correlation (figure 2.2) can be found between density and the minimum pressure reached before deposition in the vacuum chamber: the lower the pressure, the higher the density. The most accounted reason is that residual oxygen in the vacuum chamber results in deposition of a partially oxidised film, which has lower density. Samples deposited with initial pressure lower than 4×10^{-9} bar have the highest density, except the one with the shortest deposition time (60 s): this is probably due to the fact that the film is very thin and oxidises quickly after exposure to air. In figure 2.2 the value of bulk density is indicated for comparison: the highest obtained density of thin film is about 20 % lower than bulk density.

2.2.3 Roughness and homogeneity

The roughness of the deposited film was evaluated by using atomic force microscopy (AFM). The film's surface turned out to be flat and smooth, its roughness being much less than 2 nm, as shown in the image 2.3 (the roughness of an virgin polished wafer is typically less than 1 nm). The film's homogeneity can be also evaluated from XRR spectra: the regular and well resolved peaks, as the ones shown in figure D.3 give an indication of smoothness and homogeneity.

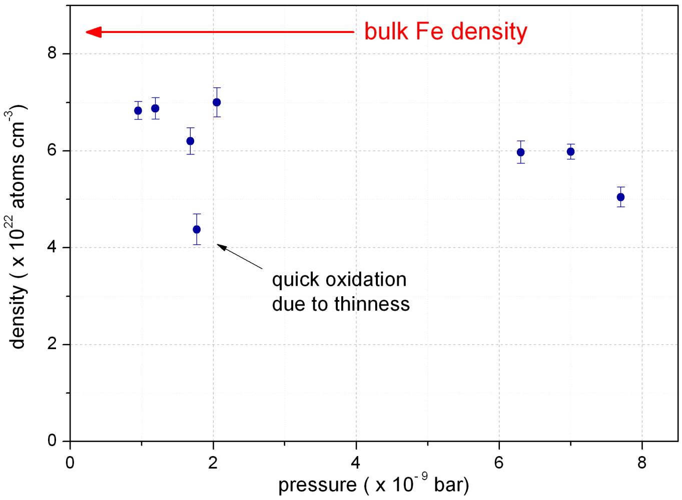

Figure 2.2: Calculated density of deposited Fe films as a function of pressure of residual gases inside the deposition chamber before deposition. Density of bulk iron is indicated for comparison.

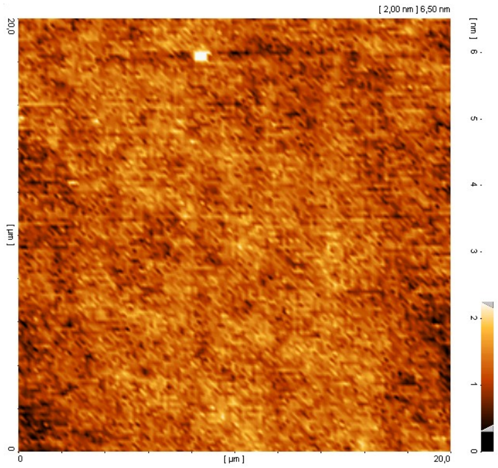

Figure 2.3: Image of the surface of an as-deposited sample obtained by atomic force microscopy. The image refers to a 20 µm × 20 µm square region; the colour scale spans 2 nm.

2.3 Thermal diffusion of Fe in $LiNbO_3$

Once the thin iron film was deposited on LN wafer, iron was made to diffuse inside lithium niobate through suitable thermal treatments, under different atmospheres. To obtain significant diffusion depth, high temperatures are required. The effect of the atmosphere surrounding the sample during diffusion was investigated by testing different gases and comparing the results. At high temperature, lithium niobate suffers from Li out-diffusion [21] and loses OH groups [11]: it is known [22] that to prevent these phenomena it is sufficient to treat $LiNbO_3$ in wet atmosphere. Wet atmosphere introduces hydrogen atoms in LN, which on one hand contribute to dark conductivity in the erasure of photorefractive patterns, on the other hand are useful for thermal fixing. Therefore both wet and dry atmosphere were tested and their effect on the material properties was investigated.

2.3.1 Apparatus

A standard tubular furnace was used, manufactured in Germany by Gero Hochtemperaturöfen Gmbh (model F-VS 100-500/13): the heating element is made of CrFeAl alloy, the maximum operation temperature is 1300 °C. The equipment for vacuum or inert gas treatments consists of: water-cooled vacuum flanges, gas inlet, two rotameters with metering valve for adjustment of gas flux, a manometer which displays the internal pressure, gas outlet connected to aspiration system. The two rotameters are furnished with calibration certificate for nitrogen and argon gases. Calibration refers to an inlet pressure equal to 1.2 bar; scale is in NL/h[1].

The following gases were used: oxygen, argon, argon + 4 % hydrogen, nitrogen + 4 % hydrogen. They are stored in gas cylinders with volume 40 L, pressure 160 ÷ 200 bar, purity 5.0. The gases undergo two pressure reduction stages to reach 1.2 bar, the pressure required by the calibrated rotameters. For providing wet atmosphere, the gas bubbles through pure water in a sealed glass bottle before entering the rotameter.

The furnace is capable of heating or cooling rates up to 600 °C/h. A thermal characterisation of the furnace was made: setting a constant temperature, the internal temperature of the furnace was measured by an R-type thermocouple as a function of position inside the furnace's pipe. It was found that the region of homogenous highest temperature extends few centimetres in the centre of the furnace, and this temperature is 20 °C lower than the set temperature. Therefore samples were always put in the same central position and temperature was set 20 °C higher than the desired one. From now on, the indicated temperature values refer to the effective temperature.

2.3.2 Experimental procedure

The sample arrangement consists in laying the sample, with the iron film upwards, on an alumina piece which is curved to minimise the LN-alumina contact surface[2]. The alumina piece lays on a quartz boat to introduce all inside the furnace.

Since lithium niobate suffers from too quick heating/cooling rates, all samples were brought to high temperature with rates of 300 °C/h. Temperatures ranged from 800 °C to 1000 °C, the treatment's duration, exclusive of heating and cooling, ranged

---

[1] The normal-liter is a unity of measure for gases defined in the following way: 1 NL of a certain gas is the volume that contains the same mass of 1 L of air in the same pressure and temperature conditions.

[2] Contact should be minimised because of Na contamination by alumina and Si contamination by quartz [23].

from 1 h to 40 h. Thermal treatments occurred under continuous gas flow (including heating and cooling). The Ar calibrated rotameter was used both for Ar and for Ar + H_2. Oxygen flow was usually set to 90 NL/h, whereas argon flow (which affects the reduction degree of the material, as will be largely argued in the following chapters) ranged from 50 NL/h to 250 NL/h.

Some samples were treated first in oxygen, then in argon, or in other gases. It must be specified that this kind of treatment occurs under oxygen flow during the heating up and the first high temperature hold, then after the cooling ramp gas is swapped and the treatment proceeds under Ar, or Ar + H_2, or N_2 + H_2 flow during the second temperature hold and the cooling down.

2.3.3 Thermal treatments

A large number of experiments was performed to achieve different purposes. In view of the lack of data and models in literature, the first purpose is to study the diffusion of iron in lithium niobate. Therefore systematic experiments were done, varying the most important parameters (time and temperature) in order to study the surface behavior and to derive, if possible, a diffusion coefficient and extract a phenomenological law for diffusion of iron. The second purpose is to study how the different atmospheres affect iron inside lithium niobate. The third, final purpose is to find the optimum treatment to produce samples for the application.

Regarding the second purpose, first of all it is important to get information from literature about atmospheres used to treat iron doped lithium niobate: in the past the material was treated in oxygen, in argon, in vacuum, in order to get different valence state for iron. In the present work, also other gases were used, e. g. a mixture of Ar 96% and H_2 4%.

Regarding the first purpose, studying of iron diffusion, systematic experiments were performed on namely identical samples varying the temperature (in the range 800 °C - 1050 °C) at constant duration, and varying the duration (in the range 1 h - 40 h) at constant temperature. These experiments were performed both in oxygen and argon, at constant flow. Another systematic study was made on the effect of argon flow: namely identical samples underwent the same treatment (900 °C, 10 h), but with different gas flows.

Before thermal treatment, the iron film, though very thin, is clearly visible and appears as a metallic reflective surface. At the end of the treatment, samples extracted from the furnace are transparent, and may be differently coloured depending on the kind of treatment:

- oxygen treated samples are fully oxidised, the matrix is unaltered and contains only Fe^{3+}, or a negligible amount of Fe^{2+}, therefore they are colourless just like the virgin material;
- argon treated samples contain a variable amount of Fe^{2+}, and show a red-brown colour, more or less intense depending on concentration and reduction degree;
- samples treated in Ar + H_2 at high temperature show a metallic grey colour, their surface is irreversibly damaged both structurally and chemically;
- after short treatments, some non-diffused iron remains on the surface, but it lost its metallic appearance, indeed the sample is transparent with an ochre colour clearly distinguishable on oxidised samples.

As will be discussed thoroughly in the following chapters, diffusion in oxygen proved to be the best choice due to its reproducibility and maintenance of $LiNbO_3$ properties. Diffusion in argon resulted to be faster but less controllable and gives a non sufficient reduction degree. In order to vary the reduction degree of samples diffused in oxygen, a method was experimented which consists in treating samples under a reducing gas at temperatures much lower than those required for diffusion. To this aim, the mixtures $Ar + H_2$ or $N_2 + H_2$ at 500 °C do not damage the material and succeed in obtaining the desired reduction degree. Moreover, this treatment is reversible: with a suitable treatment in oxygen, the reduction degree can be lowered again. This method has a further advantage: since it is performed at low temperature, it does not promote further diffusion of Fe. This means that it is possible to vary the reduction degree at wish, without changing the distribution of Fe.

Differential thermal analysis

Differential thermal analysis (DTA) allows to detect endothermic or exothermic changes in the sample relative to an inert reference, by recording temperature difference between sample and reference during identical thermal cycles. In order to investigate possible changes in composition or phase in the Fe film during the heating ramp, a differential thermal analysis experiment was performed using about 200 mg of $Fe{:}LiNbO_3$ as deposited and 100 mg of kaolin as reference sample, which underwent a heating ramp from room temperature to 800 °C at constant heating rate (10 °C/min) in air. The thermogram showed a broad peak at about 300 °C, which was attributed to Fe oxidation.

Chapter 3

Study of iron diffusion

The knowledge of how iron diffuses in lithium niobate is important for our final application because it allows to forecast the dopant distribution, given a certain diffusion treatment. Studying the diffusion of iron has also a basic theoretical importance, since few works have been done until now. In most of these works, diffusion is analysed phenomenologically, giving the diffusion coefficient and how it changes by changing the diffusion conditions, i.e. temperature, composition, etc. A great part of them are focused on diffusion of intrinsic species, that is, Li and Nb, particularly Li enrichment to get from the congruent composition to the stoichiometric one [24]. In the framework of proton exchange waveguides, diffusion of hydrogen and its isotopes was also studied [11]. There are some papers about diffusion of elements chemically similar to Li and Nb: alkali and Ta. Among the other metal cations mostly used as dopants for lithium niobate, Ti is the most investigated, due to its importance in waveguide fabrication [25]. Particularly iron diffusion was rarely investigated before: only two articles give its diffusion coefficient [26] [27].

As already introduced in section 2.3.3, this work involves many systematic diffusion experiments, varying the most important parameters: temperature, duration, concentration, gas flow, and, above all, atmosphere. The diffusion atmosphere is the most accounted factor responsible for different diffusivity values obtained in different processes. Few studies have been done in the past, and the effect of different atmospheres is still unknown [24].

In the great majority of works devoted to diffusion of transition metal ions, the diffusion profiles have been inferred indirectly from refractive index variations upon formation of in-diffused optical waveguides, assuming that the refractive index changes linearly with concentration of impurity atom. In this work instead, a direct compositional method, Secondary Ion Mass Spectrometry (SIMS), was exploited to investigate the diffusion profiles. This chapter contains the results and preliminary discussion, while experimental details and data analysis are reported in appendix A.

3.1 Diffusion in lithium niobate: general considerations

3.1.1 Phenomenological approach

One of the main approaches to diffusion is to treat diffusing substances as a continuum, ignoring the atomistic nature of the process. According to Fick's first law, the diffusion flux J of a species is related to the gradient of its concentration C in a purely phenomenological way by:

$$J = -D\nabla C$$

where the diffusion coefficient D is, in general, a second rank tensor. The concentration varies with time, in the absence of sinks and sources of diffusing species, according to Fick's second law:

$$\frac{\partial C}{\partial t} = \nabla(-J) = \nabla \cdot (D \cdot \nabla C) \tag{3.1}$$

The diffusion coefficient may depend on temperature, position, concentration, crystal defects, concentration of other impurities, etc. The temperature dependence is usually found to obey an Arrhenius relation:

$$D = D_0 \exp\left(-\frac{E_A}{kT}\right) \tag{3.2}$$

characterised by the prefactor D_0 and the activation energy E_A.

The evolution of the concentration with time can be found by solving Fick's second law with appropriate initial and boundary conditions. Experimental conditions usually correspond to the two basic setups described below, for which analytical solutions exist, provided that D is constant. Although the assumption of a constant diffusion coefficient is justified only in the case of low impurity distribution, these analytical solutions can be used often for first order estimations.

In the present case a crystal is considered with initial impurity concentration $C = 0$. The crystal surface is then exposed to a source of impurity atoms. Atoms will diffuse in the direction perpendicular to the surface, therefore a one-dimensional case of equation 3.1 can be considered:

$$\frac{\partial C}{\partial t} = D\frac{\partial^2 C}{\partial x^2} \tag{3.3}$$

that holds when D does not depend on concentration, as in the case of dilute systems. If the source of diffusion species is infinite, the analytical solution of equation 3.3 is

$$C = C_{x=0} \cdot \operatorname{erfc}\left(\frac{x}{\sqrt{4Dt}}\right) \tag{3.4}$$

where $\operatorname{erfc}(x)$ stands for the complementary error function. For a given time t, the amount of impurity atoms having entered the crystal is

$$N = \int_0^\infty C(x,t) \cdot dx = C_{x=0} \cdot \sqrt{\frac{4Dt}{\pi}} \tag{3.5}$$

The second important case is when the initial distribution of atoms at $t = 0$ can be represented by a delta function at the surface, then the solution is a Gaussian distribution:

$$C = \frac{N}{\sqrt{\pi dt}} \cdot \exp\left(-\frac{x^2}{4Dt}\right) \tag{3.6}$$

In real applications the initial distribution is not exactly a delta function, anyhow it becomes a Gaussian distribution if the standard deviation at the end of the process is much larger than that of the initial profile:

$$\sigma\left(t = t_{\mathrm{end}}\right) = \sqrt{2Dt_{end}} \gg \sigma\left(t = 0\right)$$

Since the total amount of atoms does not change with time, the surface concentration varies with time as

$$C_{x=0} = \frac{N}{\sqrt{\pi D t}}$$

3.1.2 Atomistic approach

Due to the particular intrinsic defect structure of congruent lithium niobate, care must be taken when applying general mathematical treatments, often used for diffusion in other media. A diffusion model must be thought specifically for this material, taking into account its particularities. The first attempt to give a microscopical model for diffusion in LN was done by D. P. Birnie III [24].

Whichever the defect structure is, the charge neutrality equation

$$4[\mathrm{Nb_{Li}}] = [\mathrm{V_{Li}}] + [(\mathrm{Nb_{Li}V_{Nb}})] + 5[\mathrm{V_{Nb}}]$$

must hold. According to experimental data and energy minimisation considerations, the most probable defect is the lithium vacancy at high temperature, and the cluster $(\mathrm{Nb_{Li}V_{Nb}})$ at low temperature. The transition from low temperature to high temperature is governed by the reaction

$$(\mathrm{Nb_{Li}V_{Nb}}) \longleftrightarrow \mathrm{V_{Li}} + \mathrm{Nb_{Nb}}$$

with equilibrium constant K_1. The defect cluster may also dissociate to form Nb vacancies, according to the equilibrium

$$(\mathrm{Nb_{Li}V_{Nb}}) \longleftrightarrow \mathrm{V_{Nb}} + \mathrm{Nb_{Li}}$$

with constant K_2.

The conservation of cation vacancies implies that $[\mathrm{V_{Li}}] + [(\mathrm{Nb_{Li}V_{Nb}})] = C_{\mathrm{V}}$, the total cation vacancy concentration which is constant and defines the overall stoichiometry of the crystal. In the case of congruent composition, $C_{\mathrm{V}} = 3.9$ mol%, therefore a large number of cation vacancies are available for diffusion, and impurities are thought to diffuse through motion of lithium and niobium vacancies. Because of the similarity between the possible sites, impurities I probably distribute on both (with different concentrations), and site swapping must be considered according to the equilibrium $\mathrm{I_{Li}} + \mathrm{V_{Nb}} \longleftrightarrow \mathrm{I_{Nb}} + \mathrm{V_{Li}}$, with equilibrium constant K_3.

From the microscopical point of view, the shortest migration path for a substitutional impurity (either in the Li sublattice or in the Nb sublattice) winds through a normally vacant octahedral site: a projection of the migration path on the basal plane is drawn in figure 3.1. The atom starts at the normal site, passes through an oxygen triangle that defines its octahedral site and goes to a tetrahedral site, then passes through another oxygen triangle and reaches the structural vacancy; then again it passes through other two oxygen triangles to reach the vacant cationic site. Because these triangles are different in size, only the one with largest strain will define the migration enthalpy and limit the migration rate. Concerning other crystallographic

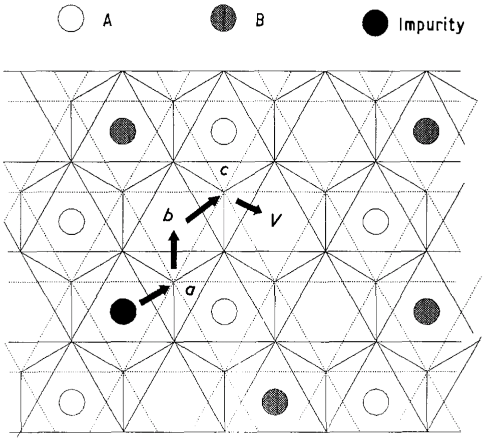

Figure 3.1: The arrangement of cations in the basal plane of lithium niobate. The surrounding oxygen sublattice is represented by lines connecting nearest neighbour oxygen centres; the two layers of oxygen atoms sandwich the cations into octahedral sites. Arrows indicate the migration path for a substitutional impurity. Because of the symmetric similarity of the lithium and niobium sublattices this migration path serves to explain motion for cations on either sublattice. Four partial jumps are represented by the short arrows. These correspond to jumps where the impurity pushes through oxygen triangles when moving between octahedral and tetrahedral sites [24].

directions, the migration path is topologically similar, passing through similar oxygen constrictions, therefore at a first approximation diffusion should be isotropic. If the impurity is distributed between both sites, the diffusion rate will be the sum of two contributions:

$$D = f_{\mathrm{Li}}[\mathrm{V}_{\mathrm{Li}}] \exp\left(-\frac{Q_{\mathrm{Li}}}{RT}\right) + f_{\mathrm{Nb}}[\mathrm{V}_{\mathrm{Nb}}] \exp\left(-\frac{Q_{\mathrm{Nb}}}{RT}\right) \tag{3.7}$$

where Q_{Li} and Q_{Nb} are activation energies for motion of Li and Nb vacancies. If the impurity prefers Li site, $D \simeq C_{\mathrm{V}} K_1 \exp\left(-\frac{Q_{\mathrm{Li}}}{RT}\right)$ in the low temperature regime, $D \simeq C_{\mathrm{V}} \exp\left(-\frac{Q_{\mathrm{Li}}}{RT}\right)$: the only difference is the factor K_1, but this will only influence the activation energy measured. It should be underlined that the diffusion coefficient varies linearly with the deviation from stoichiometry.

3.2 Surface evolution during first stages of Fe diffusion

So far, abstract considerations about diffusion have been presented. However, the real system under study passes from an initial condition, in which Fe atoms are located in the deposited metallic film, to a final condition, in which the film is disappeared and Fe atoms are distributed in the LN matrix, which can be described by the above mentioned general equations, for instance equation 3.6. An important passage to understand is how the system passes from the initial to the final condition, and how this stage affects the final result. This section just describes this passage, i.e. the evolution of the system during the diffusion treatment. In the past the evolution of an analogous system, Ti diffusing in LN, has been investigated, therefore it is useful to discuss briefly Ti diffusion for comparison.

3.2.1 Comparison with Ti diffusion

Several studies were made to understand the diffusion of titanium in lithium niobate, widely employed for waveguide fabrication. It is worth to briefly describe this subject, because Ti doping was performed in the same way as Fe doping is performed in the present work, i.e. by in-diffusing a thin metallic layer.

Ti in-diffusion process consists of three major stages, each occurring in a specific temperature range:

1. oxidation of the Ti film;
2. interaction of the Ti oxide with the $LiNbO_3$ substrate;
3. consumption of a Ti-rich oxide layer by the substrate.

It was found [28] that at 550 °C the original metallic Ti film is completely oxidised to rutile TiO_2, while $LiNb_3O_8$ starts to grow epitaxially on the $LiNbO_3$ surface under the Ti film. At 800 °C the rutile grains coarsen until the rutile film becomes fully epitaxial on the $LiNb_3O_8$ layer. With increasing annealing time, the $LiNb_3O_8$ phase is consumed by the rutile due to extensive interdiffusion between the two phases. A solid solution $LiNb_3O_8$ - TiO_2 sets up: both neighboring phases, $Ti_{1-4x}Li_xNb_{3x}O_2$ and $LiNbO_3$, have the same continuous near-hcp oxygen framework with cations occupying octahedral sites. Ti diffusion into the $LiNbO_3$ substrate is negligible at this temperature. At 1000 °C the solid solution acts as the final source for Ti in-diffusion and gets gradually consumed by the substrate [28].

In order to find out if Fe diffusion from thin film behaves in the same way as Ti before the complete diffusion of iron, a dedicated investigation was accomplished. A set of samples were annealed in dry oxygen at temperatures lower than the temperatures usually required for complete exhaustion of Fe film, and the surface was investigated with secondary ion mass spectrometry to study the distribution of iron and with X-rays diffraction to look for possible other crystalline phases than $LiNbO_3$.

3.2.2 Evidence of a new phase

When the thermal treatment is carried out at 800 °C or lower temperature, only a part of the Fe film has diffused into $LiNbO_3$, the remaining part being located in a superficial layer whose nature has been investigated by means of targeted experiments.

To the naked eye, this residual layer appears as an orange or yellow film on the surface, as shown in figure 3.2. SIMS analysis reveals straight off the presence of the residual layer, as can be seen in the profile of figure 3.3, acquired with high primary beam current with depth resolution of about 20 nm. During the erosion of first nanometres, counts for Li and Nb are few compared to the bulk, while Fe signal show a very intense peak. After 100 nm Li, Nb and O signals become constant and the Fe signal starts its usual semi-gaussian diffusion profile. This results are consistent with the presence of a superficial phase rich in iron and oxygen: compositional investigation of this phase requires however a much higher depth resolution. Evidence of a new phase stems out also from X-rays diffraction: by performing an ω - 2θ scan, as the one shown in figure 3.4, diffraction peaks are found that are not referable to any phase of

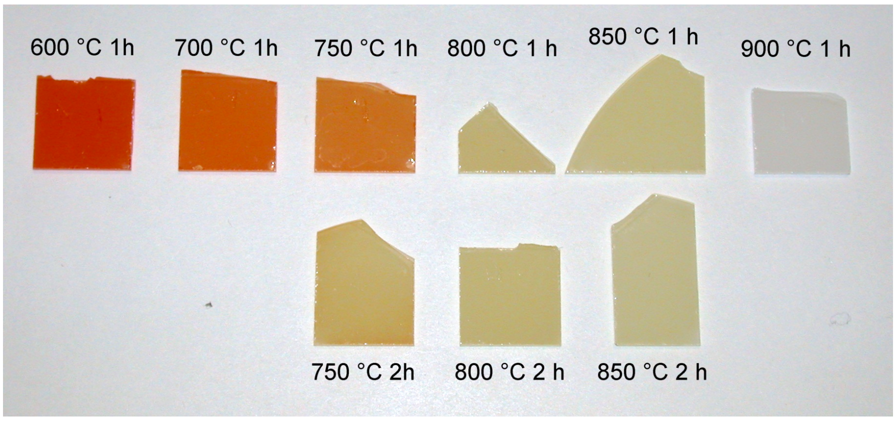

Figure 3.2: Picture of the set of samples prepared for the investigation of the residual layer. Annealing was carried out under dry oxygen, temperature and duration are indicated beside each sample.

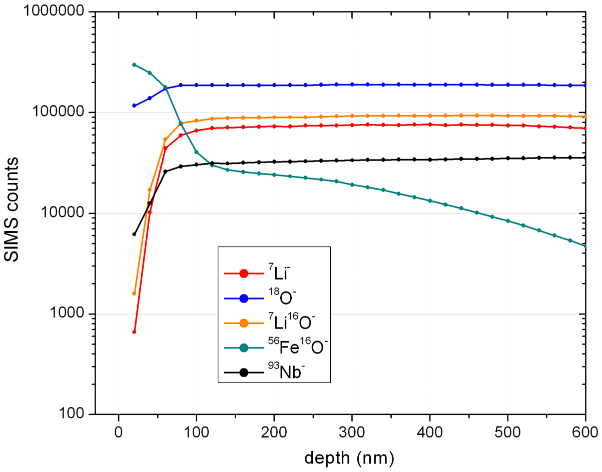

Figure 3.3: SIMS depth profile of intrinsic elements and dopant in a sample with residual layer.

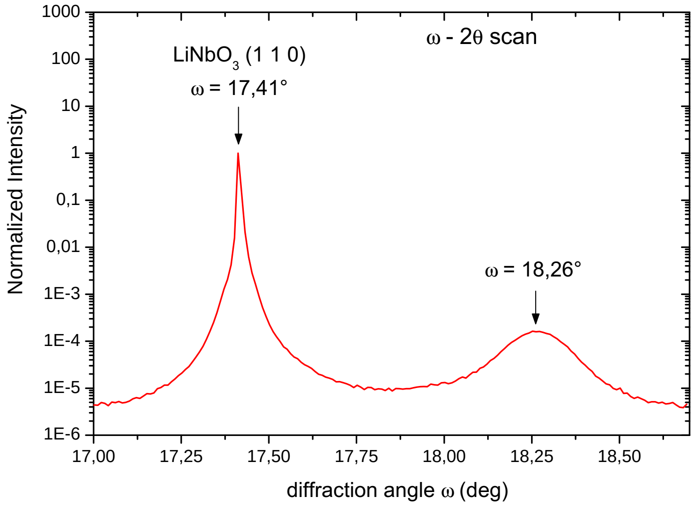

Figure 3.4: X-rays diffraction ω - 2θ scan on a sample with residual layer. Besides the (1 1 0) diffraction peak, another peak appears whose diffraction angle does not match any reflection of the Li - Nb - O system.

the Li - Nb - O system. A set of experiments were therefore designed to understand better the composition, the structure, and the formation/vanishing dynamics of this phase. A set of samples with the same Fe amount were annealed shortly (1 - 2 h) at temperatures ranging from 600 °C to 900 °C and then analysed with SIMS and XRD, in order to investigate the dependance on temperature. Another set of samples with different Fe amount were annealed at the same temperature in order to study the dependence of vanishing on the amount on Fe.

3.2.3 Compositional analysis of residual layer

The samples with residual layer were analysed by SIMS adopting different conditions and the results are compared to develop a consistent overview. Three measurement conditions were used:

- in negative mode with a 14.5 keV primary beam and electron gun for charge compensation (depth resolution 10 nm);
- in negative mode with a 7 keV primary beam, without electron gun (depth resolution 6 nm);
- in positive mode with a 5.5 keV primary beam, without electron gun (depth resolution 4 nm).

In negative mode the ions detected are $^{7}\mathrm{Li}^{-}$, $^{18}\mathrm{O}^{-}$, $^{56}\mathrm{Fe}^{16}\mathrm{O}^{-}$, $^{93}\mathrm{Nb}^{-}$; in positive mode, the ions detected are $^{133}\mathrm{Cs}^{7}\mathrm{Li}^{+}$, $^{133}\mathrm{Cs}^{16}\mathrm{O}^{+}$, $^{133}\mathrm{Cs}^{56}\mathrm{Fe}^{+}$, $^{133}\mathrm{Cs}^{93}\mathrm{Nb}^{+}$. All the experimental details are described in appendix A.

For each sample, the depth profiles obtained with different conditions are arranged in columns, in order to ease the comparison, in figures 3.5 and 3.6.

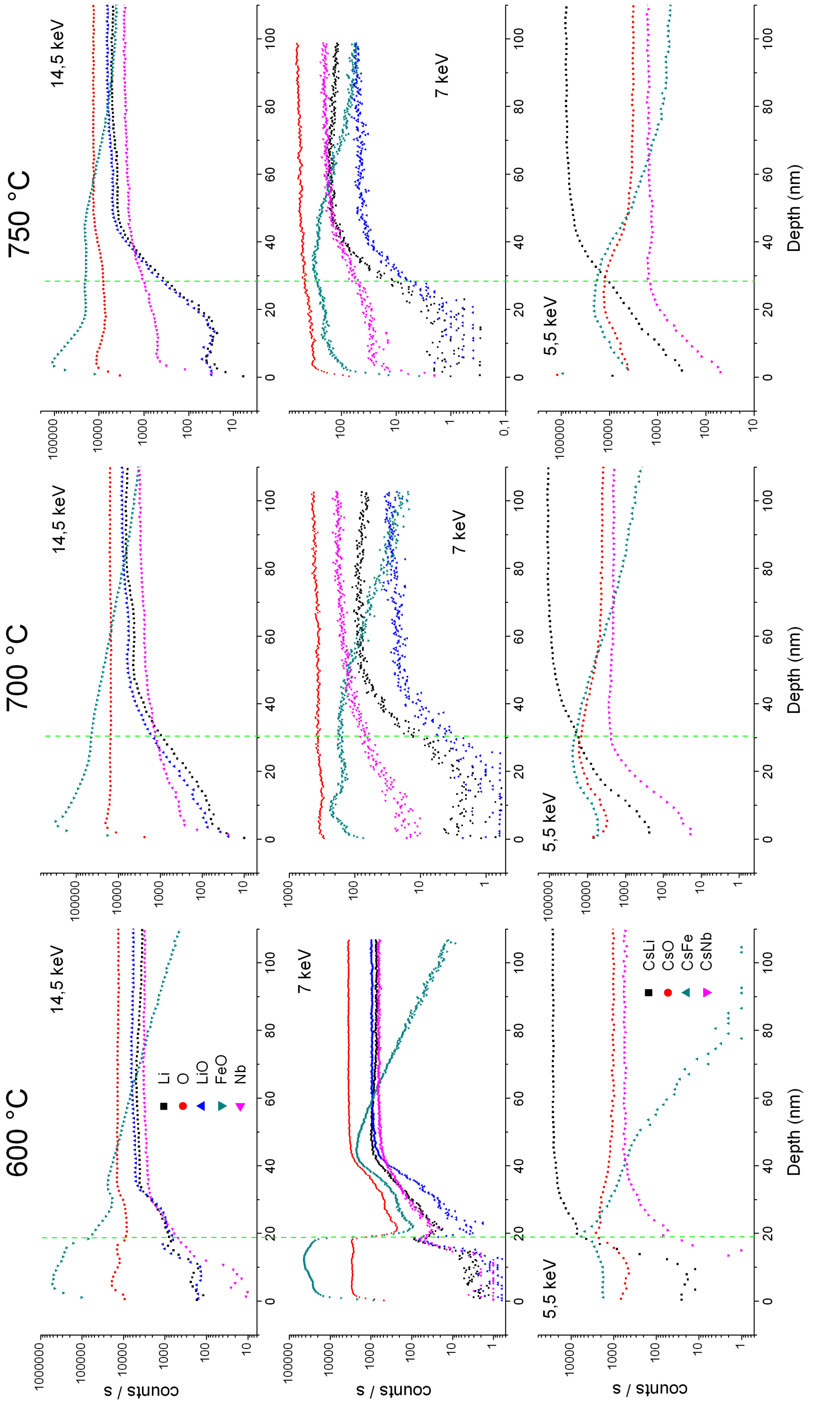

Figure 3.5: SIMS depth profiles of samples with residual layer annealed at 600 °C, 700 °C, and 750 °C. Each column includes profiles of the same sample, annealed at the temperature indicated on top; each row includes profiles obtained in the same experimental conditions (14.5 keV, 7 keV, 5.5 keV).

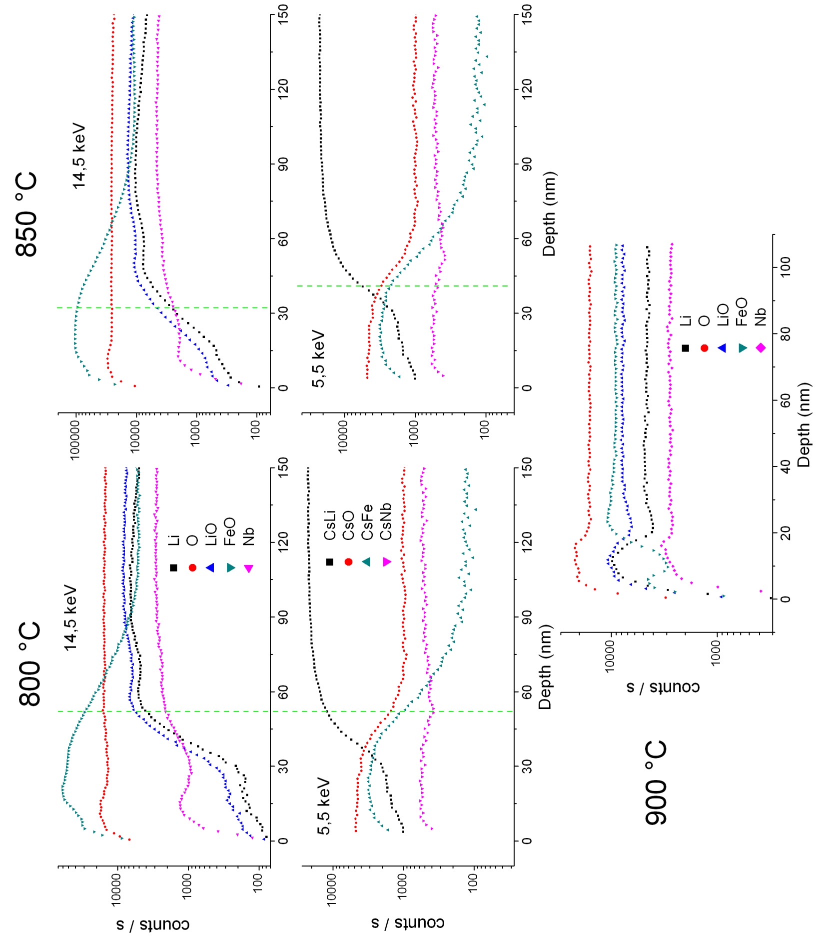

Figure 3.6: SIMS depth profiles of samples with residual layer annealed at 800 °C, 850 °C, and 900 °C.

600 °C

Charge compensation on this sample was easily achieved in all the three measurement conditions, indicating that the residual layer has a good conductivity and act as a sink for excess charges, avoiding charging up. In all the three profiles, a discontinuity can be clearly distinguished at $18 - 20$ nm, locating the interface between residual layer and substrate. In both profiles obtained in negative mode, a dip in all signals trend can be recognised, extending from the interface up to 40 nm: as explained in section A.4.3, this dip is an artefact in SIMS ion yields, probably due to the fact that the two neighbouring phases are incoherent. The dip is absent in positive mode, thus confirming that it is an artefact. After the erosion of residual layer, Fe counts are in great numbers, but their trend is different in the three depth profiles. The signal follows an exponential decay, with different decay length according to the energy of the primary beam: arguments explained in section A.4.3 prove that this exponential tail is solely due to recoil implantation from the overlying film. This implies that Fe is not actually present in the substrate. Thus at 600 °C diffusion of Fe in LN does not take place, namely the diffusion coefficient is negligible. Concerning the composition of the residual layer, the small number of counts for Li and Nb in the first 20 nm suggest that Li and Nb are negligible or absent, whereas O counts are abundant, indicating that this layer probably consists of bare iron oxide.

700 °C

Also for this sample charge compensation was easily achieved. In this case there is no clear discontinuity in any of the three profiles: in the first 20 nm Li and Nb signals are low, then from 20 nm to 50 nm both signals grow up to their bulk values, less steeply than the previous sample. The signal of Fe shows a decay much deeper than the one observed in the previous sample, indicating that Fe atoms have started to diffuse in the substrate. These features can be interpreted in the following way: the two phases became pseudomorphous (justifying the absence of any discontinuity) and started to interdiffuse, therefore the composition changes gradually from iron oxide to lithium niobate (justifying the smoother profiles of Li and Nb). In order to quantify the thickness of the residual layer, an interface has been arbitrarily placed at 30 nm, corresponding to the middle of the Li signal raise.

750 °C

This sample shows the same features of the one annealed at 700 °C, except that the diffusion of Fe is deeper (see figure 3.12).

800 °C

This sample did not allow a good charge compensation in negative mode without electron gun, therefore only two profiles are presented. The main difference with respect to the samples discussed so far is the colour, that changed from orange to yellow. The Li signal, likewise the other samples, shows a plateau up to 30 nm, then a smooth raise. The other signals instead changed their behaviour. In particular, Nb signal does not show anymore an increasing trend in the residual layer: on the contrary, in positive mode it starts with a plateau and remains practically constant from surface to depth; in negative mode, it shows a hump typical of Nb signal within surface equilibration depth (see section A.4.1 and figure A.8). The whole depth profile in

	600 °C	700 °C	750 °C	800 °C	850 °C	900 °C
Thickness	<20 nm	30 nm	30 nm	> 40 nm	< 40 nm	zero
Colour	orange	orange	orange	yellow	yellow	uncoloured
Diffraction peak	broad	narrow	narrow	narrow	narrow	absent
Interface	abrupt	smooth	smooth	smooth	smooth	none
Conductivity	very good	good	good	bad	bad	very bad
Nb signal trend	step	smooth raise	smooth raise	nearly constant	nearly constant	as bulk
Fe diffusion	absent	partial	partial	partial	partial	complete
after H_3PO_4 attack	uncoloured	yellow	yellow	yellow	yellow	uncoloured

Table 3.1: Experimental observations about residual layer sample treated at temperatures ranging from 600 °C to 900 °C: thickness was determined by SIMS depth profiling; the quality of the interface is argued from SIMS signals trend; the conductivity was estimated qualitatively through the ease in reaching charge compensation during SIMS measurements; last row refers to the appearance after treatment in aqueous solution of phosphoric acid.

positive mode, less affected by artefact than the other, indicate a constant composition in the residual layer, with a non negligible amount of Nb. These observations suggest that the residual layer consists of a phase containing Nb, Fe and O, with thickness about 40 nm.

850 °C

This sample is practically identical to the one annealed at 800 °C. The same considerations hold.

900 °C

For this sample charge compensation was achieved only with electron gun, indicating the absence of conductive layers: as a consequence only one depth profile is presented. This profile has the same characteristic trends of a bulk doped Fe:LN (see figure A.8 for comparison). The signals are not constant over the first 20 nm, their humps and dips being due to unsteadiness of SIMS yield, but the concentration of the corresponding elements is actually constant. The residual layer has therefore disappeared, as confirmed by the vanishing of the diffraction peak.

Summary

A summary of all the experimental observations on samples with residual layer is reported in table 3.1. It stands out that samples treated at 700 °C and 750 °C are similar and also samples treated at 800 °C and at 850 °C are similar, but show different features with respect to the former two; sample treated at 600 °C is different from all the others, and finally sample treated at 900 °C clearly has no residual film at all.

All the experimental observation are interpreted in the following way. As the annealing temperature increases, the system evolves according to the following steps:

- Until 600 °C, the Fe metallic film, exposed to oxygen, gets oxidised and iron oxide is formed. From the crystallographic standpoint, it has a non perfect order and is incoherent with the underlying LN crystal. No mass transport occurs between LN and iron oxide, because of non sufficient thermal energy.
- At 700 °C, the iron oxide rearranges and becomes pseudomorphous to the substrate. At the interface, interdiffusion of cations occurs, broadening the interface between iron oxide and LN. Fe starts to diffuse in LN substrate.
- At 800 °C, iron oxide disappears. Interdiffusion led to the formation of a crystalline layer, consisting of Fe, Nb and O atoms, thicker than the original iron oxide layer. This layer acts as diffusion source of Fe atoms diffusing inside LN.
- At 900 °C, interdiffusion proceeds and the layer gets gradually consumed until it vanishes completely, leaving a surface of Fe-doped LN monocrystal.

With the aim to confirm or discard this hypothesis, samples were treated in phosphoric acid (H_3PO_4) in aqueous solution, which should remove iron oxide, if there is any[1]. Indeed after the acid treatment the sample annealed at 600 °C became uncoloured, whereas the ones annealed at 700 °C and 750 °C lost their orange colour and became yellow as the other ones annealed at higher temperature. This indicates that probably the orange colour is due to iron oxide, and confirms the presence of an interlayer, not attacked by phosphoric acid, which gets formed above 700 °C. Probably the unknown yellow crystalline phase is $FeNbO_4$, a photoelectronic material with potential applications as gas sensor, catalyst or photodetector; further investigation by means of XRD should lead to the identification of the phase, and should also clarify why the apparently same diffraction peak is visible both when only presumed iron oxide is present and also when only the unknown yellow phase is present. These aspects will be the subject of a PhD thesis by A. Zaltron.

Consumption of the unknown phase depends both on temperature and on thickness, which in turn depends on the amount of Fe deposited. Indeed if more Fe was deposited, the residual layer is thicker and the interface, moving slowly towards the surface, will take more time to reach it. In order to determine which temperature and which duration are required for complete consumption of the residual layer, several test were done. The results are schematised in figure 3.7, where the coloured cells indicate the presence of the residual layer.

---

[1] Phosphoric acid reacts with iron oxide giving iron phosphate, soluble in water.

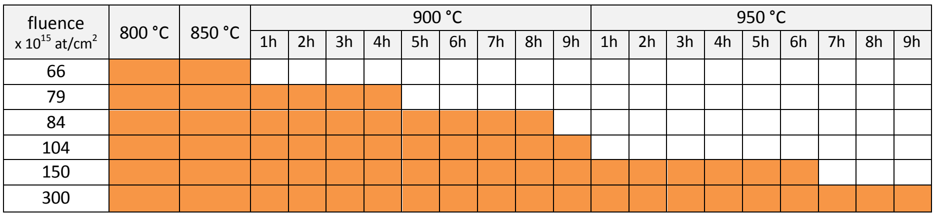

fluence x 10^{15} at/cm^2	800 °C	850 °C	900 °C									950 °C								
			1h	2h	3h	4h	5h	6h	7h	8h	9h	1h	2h	3h	4h	5h	6h	7h	8h	9h
66	🟧	🟧																		
79	🟧	🟧	🟧	🟧	🟧	🟧														
84	🟧	🟧	🟧	🟧	🟧	🟧	🟧	🟧	🟧	🟧										
104	🟧	🟧	🟧	🟧	🟧	🟧	🟧	🟧	🟧	🟧	🟧									
150	🟧	🟧	🟧	🟧	🟧	🟧	🟧	🟧	🟧	🟧	🟧	🟧	🟧	🟧	🟧	🟧	🟧			
300	🟧	🟧	🟧	🟧	🟧	🟧	🟧	🟧	🟧	🟧	🟧	🟧	🟧	🟧	🟧	🟧	🟧	🟧	🟧	🟧

Figure 3.7: Schematics indicating the occurrence of the residual layer after annealing: each column refer to annealing parameters (temperature and duration) and each row refers to the initial Fe fluence. The cell corresponding to each couple of entries is coloured if the residual layer was present, uncoloured if it was absent.

3.3 Analysis of concentration profiles

According to the former analysis, the minimum thermal treatment's duration to obtain complete vanishing of any residual phase depends on the amount of iron: e.g. at least 1 h at 900 °C for an iron film containing 66×10^{15} at/cm^2. Once the residual layer has been completely consumed, it is reasonable to assume that all the Fe atoms have entered the substrate: differential thermal analysis and PIXE measurements support this statement. Hence it is possible to extract from the Fe normalised signal profile obtained by SIMS the true concentration profile after a simple normalisation procedure. The experimental Fe signal $S(x)$ is proportional to concentration through a factor called relative sensitivity factor RSF:

$$C(x) = RSF \cdot S(x)$$

This factor can be derived by putting the integral of the profile equal to the fluence F of the deposited Fe thin film measured by RBS:

$$\int_0^d C(x)\,dx = F \qquad \text{and} \qquad RSF = \frac{F}{\int S(x)\,dx}$$

where d is the crater's depth; the fluence units are as usual at/cm^2, the concentration and RSF units are at/nm^3, and depth unit is nm. Further considerations about RSF of Fe in LN are reported in appendix A.

SIMS data were normalised and converted to concentration profiles for all the samples: the results reported in the following section are divided according to the gas used.

3.3.1 Diffusion in argon

First experiments with argon involved a study of diffusion's dependence on duration. A set of three diffusions was performed at 800 °C with flow 100 Nl/h with durations 2, 4, 8 h. SIMS profiles shown in figure 3.8 (a) indicate an anomalous behaviour: diffusion profile after 2 h is slightly deeper than diffusion profile after 4 h. This hints a lack of reproducibility of the experimental conditions. It was then hypothesised that diffusion in argon is highly sensitive to the partial pressure of the gas in the

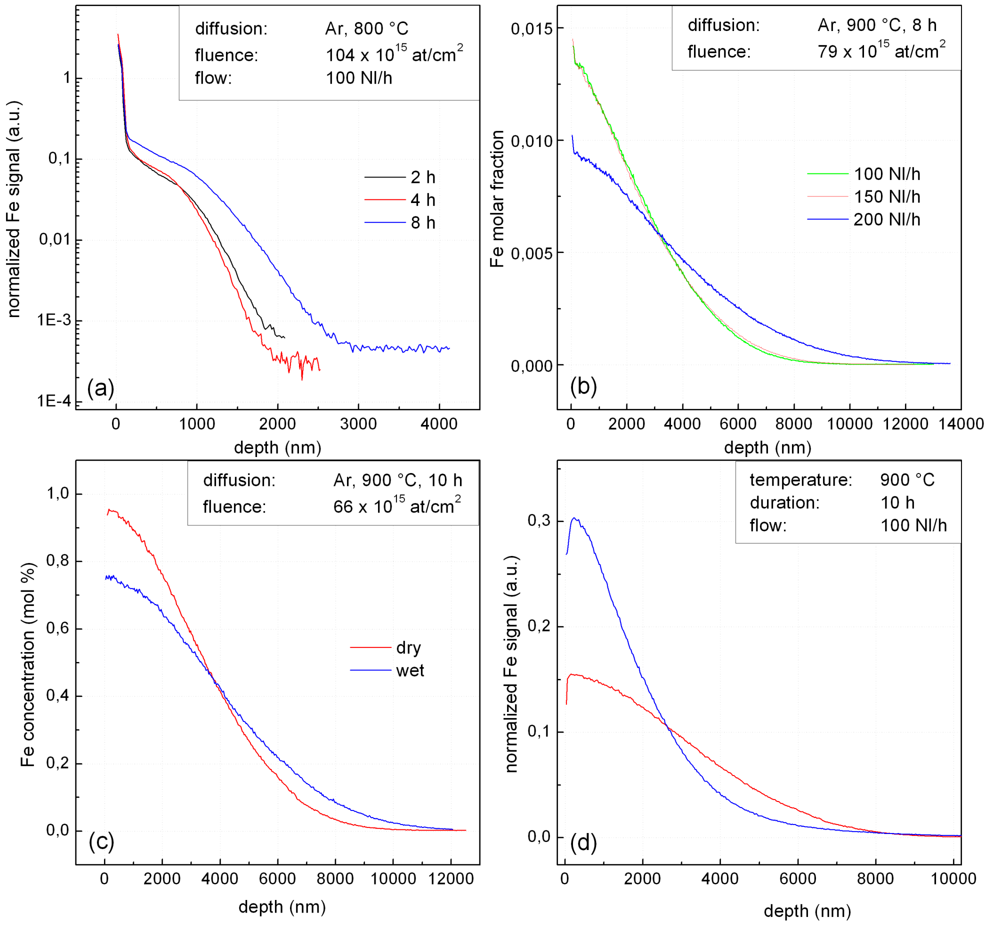

Figure 3.8: Significant comparisons of diffusion profiles obtained under argon atmosphere. (a) comparison between profiles obtained for different durations at 800 °C with the presence of the residual layer; (b) comparison between profiles obtained with different amount of gas flowing in the furnace; (c) comparison between profiles obtained under dry and wet argon atmosphere; (d) comparison between two profiles obtained under nominally identical conditions.

diffusion furnace. With the aim to check this dependence, another set of experiments were carried out at the same temperature (900 °C) and same duration (8 h) but with different gas flow. By looking at the diffusion profiles in figure 3.8 (b), there seems to exist a dependence of diffusion on gas flow: profiles obtained with 100 Nl/h and 150 Nl/h are equal, while profile obtained with 200 Nl/h is significantly deeper. It can be argued that the diffusivity under argon atmosphere is higher when the partial pressure of argon is higher. Moreover a comparison between profiles obtained after the same diffusion experiment under wet and dry atmosphere was carried out: figure 3.8 (c) shows a significant difference between the two concentration profiles obtained, suggesting that water vapour plays a role in diffusion dynamics. In order to check if all these discrepancies may be ascribed to the same lack of reproducibility noticed before, a reproducibility test was made: two namely identical samples were treated under the same conditions, obtaining two very different profiles (figure 3.8 d).

This lack of reproducibility hints that diffusion in argon depends critically on the partial pressure of argon: partial pressure was not monitored and, in spite of careful regulation of inlet flow, may vary from time to time due to changeable behaviour of extractor fan and/or extraction pipes, or due to leaks in the flanges of the furnace. A thorough investigation of this phenomena would require many tests. Since, on top of the lack of reproducibility, argon gas turned out to be inefficient in giving a significant percentage of Fe^{2+} (see section 6.1.6) and produces lattice disorder (see section 4.4.2), diffusion in argon was not further investigated and the attention was focused on diffusion in oxygen. A full examination of results obtained from many characterisation methods, followed by a final discussion about diffusion in argon, is reported in section 6.3.

3.3.2 Diffusion in oxygen

Many sets of diffusion experiments were performed under oxygen flow, investigating the diffusivity dependence on duration, fluence, temperature: the most important results are shown in figure 3.9. Diffusion at 800 °C with different durations (figure 3.9 a) shows both the residual layer presence and the diffusion profile of Fe inside $LiNbO_3$: the latter is deeper with increasing duration, as it should be. For another set of samples diffused at 950 °C with different durations (figure 3.9 b) the residual layer is absent and the diffusion profiles show a regular semigaussian shape, which gets wider the longer the duration. Concerning the dependence on temperature, figure 3.9 (c) shows diffusion profiles of samples with the same Fe fluence, diffused with the same duration, at six different temperatures in the range $800 \div 1050$ °C: the profiles obtained at 800 °C and 850 °C are narrow after the surface peak due to residual layer presence; at higher temperatures the profiles become deeper and deeper as expected from Arrhenius law. The difference between profiles obtained from dry and wet diffusion in oxygen (figure 3.9 d) is negligible. It is evident that diffusion in oxygen is more regular and foreseeable than diffusion in argon: although the experimental equipment is the same, probably the dependence of diffusivity on partial pressure is weaker for oxygen, and also leaks affect much less the composition inside the furnace, since oxygen is present also in the outer atmosphere. Moreover the profiles of samples diffused in oxygen without residual layer are well fitted with a gaussian function, on the contrary gaussian fit does not always match well profiles of samples diffused in argon.

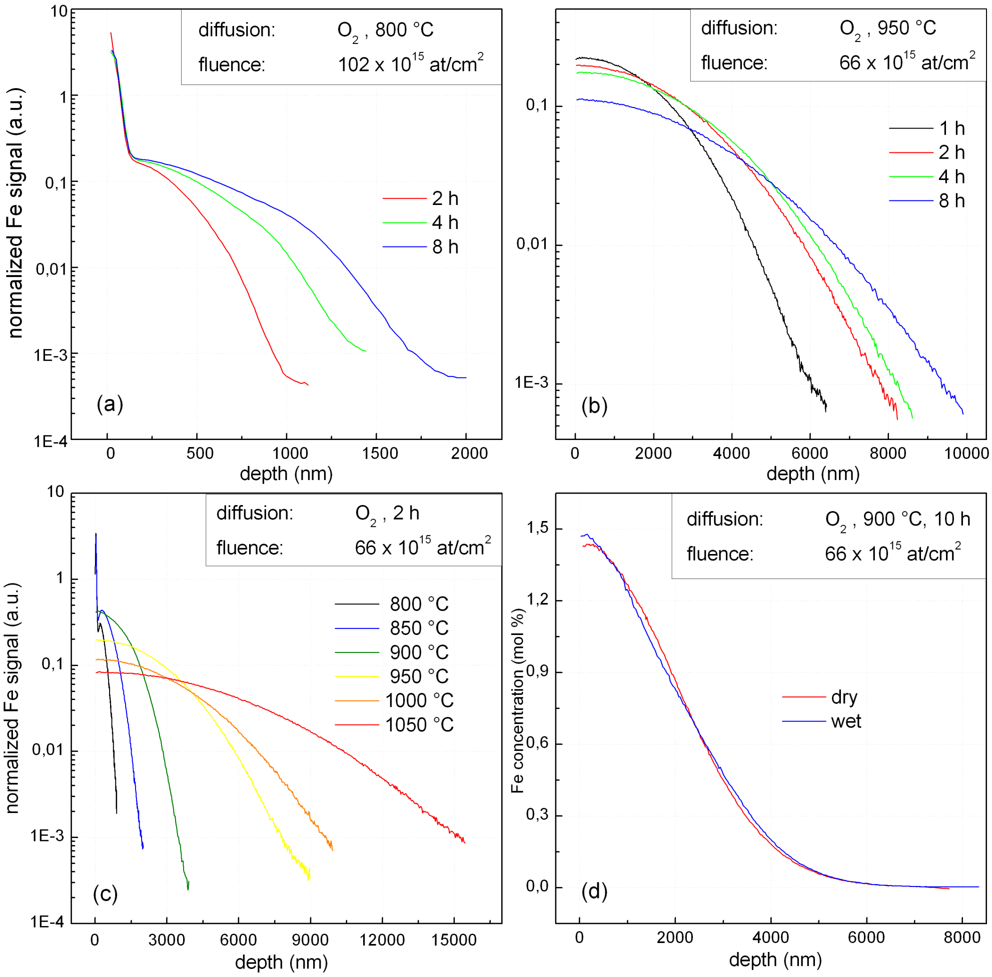

Figure 3.9: Significant comparisons of diffusion profiles obtained under oxygen atmosphere. (a) comparison between profiles obtained for different durations at 800 °C with the presence of the residual layer; (b) comparison between profiles obtained for different durations at 950 °C, with complete consumption of the Fe film; (c) comparison between profiles obtained after the same duration, at six different temperatures; (d) comparison between profiles obtained under dry and wet oxygen atmosphere.

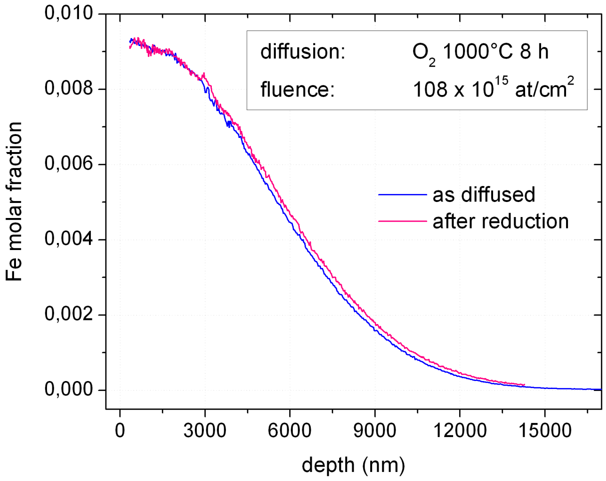

Figure 3.10: Comparison between concentration profiles of diffused Fe, before and after the reducing treatment.

3.3.3 Post treatment in Ar + H_2

As already mentioned, in order to obtain the desired reduction degree of Fe, a two-steps treatment was adopted: after diffusion in oxygen, samples are treated in Ar + H_2 at 500 °C. It is important to check if this post-treatment changes the diffusion profile. To this aim, SIMS measurements were carried out both after diffusion and after the reducing treatment. An example is shown in figure 3.10: the diffusion depths before and after reduction differ of less than 2 %, indicating that the diffusivity of Fe at 500 °C is very low. This fact is crucially important in practise, because it makes possible to vary at wish the reduction degree by varying the reducing treatment duration without affecting the concentration profile and the surface concentration, therefore a direct comparison between samples with different reduction degree can be made. The discussion of most of the results in sections 4.4.2 and 4.5 takes advantage of this possibility.

3.4 Diffusion coefficient

One of the aims of this work is to know which conditions should be adopted to produce a Fe:LiNbO$_3$ sample with the desired Fe concentration and profile. Diffusivity and activation energy are the fundamental quantities one needs to know in order to forecast diffusion. As seen above, diffusion of Fe depends strongly on the atmosphere and other parameters. Therefore, in order to calculate these fundamental quantities, efforts were concentrated to diffusion in oxygen, since it turned out to be preferable. To this aim, many diffusion experiments were performed in dry oxygen at constant flow (90 NL/h) in the temperature range 900 °C - 1050 °C. Lower temperatures were partially disregarded from this analysis because of residual phase presence, which alters SIMS measurement's conditions (see appendix A).

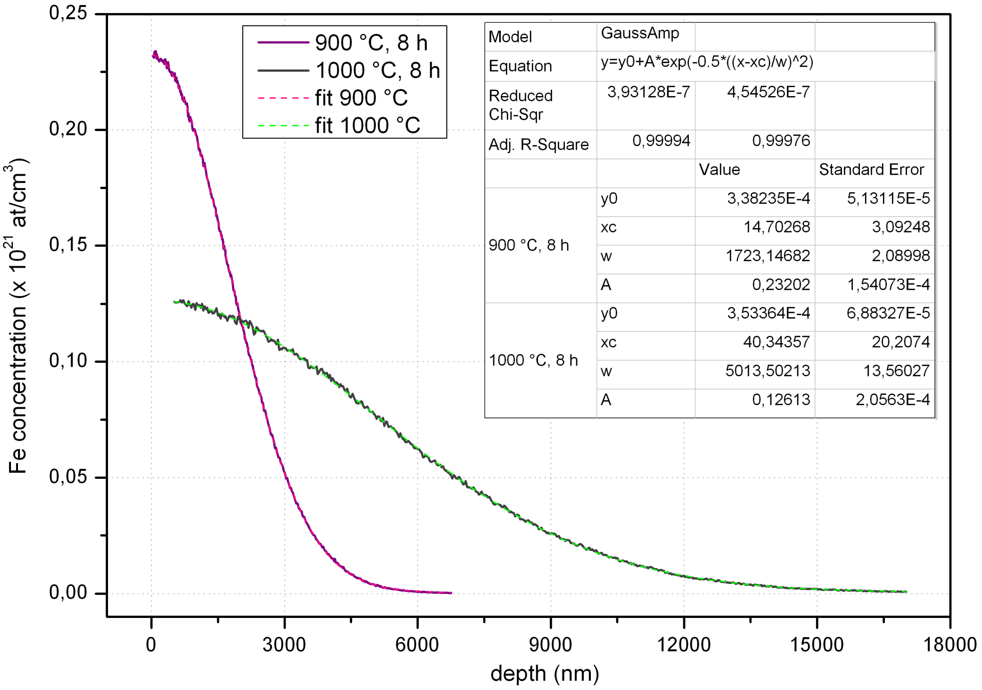

Model	GaussAmp		
Equation	y=y0+A*exp(-0.5*((x-xc)/w)^2)		
Reduced Chi-Sqr	3,93128E-7	4,54526E-7	
Adj. R-Square	0,99994	0,99976	
		Value	Standard Error
900 °C, 8 h	y0	3,38235E-4	5,13115E-5
	xc	14,70268	3,09248
	w	1723,14682	2,08998
	A	0,23202	1,54073E-4
1000 °C, 8 h	y0	3,53364E-4	6,88327E-5
	xc	40,34357	20,2074
	w	5013,50213	13,56027
	A	0,12613	2,0563E-4

Figure 3.11: Two examples of fitted depth profiles. The profiles refer to 8 h of diffusion at 900 °C and 1000 °C; they were fitted with a gaussian curve. All the fitting parameters were left free, except x_c which was constrained in the interval ($-50\,\text{nm} \div +50\,\text{nm}$). The resulting best fitting parameters are reported in the table.

3.4.1 SIMS data treatment

As a first attempt, regular Fick's diffusion was assumed, and each SIMS depth profile was fitted with a Gaussian function, with formula

$$G(x) = y_0 + A\exp(-\frac{x - x_c}{2w^2}) \tag{3.8}$$

with four free parameters y_0, A, x_c and w. Gaussian fit worked well for all the profiles considered. Some examples of fitted profiles are given in figure 3.11 and a complete list of all the samples whose profiles were fitted is given in table 3.2. The parameter x_c was not fixed for two reasons. First, experimental SIMS profiles may have an offset in the determination of surface position, due to different erosion rate at the surface; second, diffusion starts from the residual phase, which gets thinner until disappears, therefore the position of the diffusion source cannot be determined a priori. The parameter x_c was therefore allowed to vary in a reasonable range (100 nm) straddling the nominal surface position.

3.4.2 Results and uncertainty

According to formulae at the beginning of this chapter, the diffusivity is related to the parameter w by the relation

$$D = \frac{w^2}{2t}$$

Before calculating D, attention should be paid to the diffusion duration t: one must not consider just the time spent at constant high temperature, because Fe diffuses also during heating and cooling ramps. Contribution to diffusion during heating and cooling ramps was taken into account by considering an effective duration, estimated according to the following considerations. A first rough estimation of D showed that it changes of about an order of magnitude every 100 °C with an exponential fashion. Therefore, contributions from ramp parts when the temperature is below $T_\mathrm{f} - 100\,^\circ\mathrm{C}$, where T_f is the diffusion temperature, are negligible and may be disregarded. The final part of the heating ramp from $T_\mathrm{f} - 100\,^\circ\mathrm{C}$ to T_f lasts 20 minutes, during which D increases exponentially 10 times. These 20 minutes are equivalent to an effective diffusion duration t_eff equal to about 6 minutes at the final temperature T_f, in the sense that $\int D(T)dt = D_\mathrm{f} t_\mathrm{eff}$. The same consideration holds for the cooling ramp. In the end it suffices to add 12 minutes to the nominal diffusion duration to obtain an effective duration. The consistency of this assumption may be checked a posteriori by comparing values of D obtained with different durations on identical samples.

The errors associated to D values were calculated taking into account:

- uncertainty on crater's depth determination;
- SIMS depth resolution;
- error on the fitting parameter w;
- uncertainty on the effective duration of the annealing.

An uncertainty of 0.4 h on the duration, which takes abundantly into account any doubt about how to deal with heating and cooling ramps, was considered.

Temperature °C	duration h	Fe fluence $\times 10^{15}$ at/cm^2	w nm	diffusivity 10^{-5}µm^{2}s^{-1}
750	1.2	66 ± 3	81 ± 3	0.037 ± 0.02
750	2.2	66 ± 3	116 ± 4	0.042 ± 0.02
800	1.2	66 ± 3	220 ± 3	0.28 ± 0.05
800	2.2	66 ± 3	307 ± 5	0.30 ± 0.04
850	1.2	66 ± 3	388 ± 4	0.87 ± 0.09
850	2.2	66 ± 3	620 ± 2	1.21 ± 0.08
900	8.2	50 ± 2	1732 ± 1	5.1 ± 0.6
900	8.2	75 ± 2	1787 ± 3	5.4 ± 0.6
900	8.2	84 ± 2	1895 ± 9	6.1 ± 0.6
900	10.2	50 ± 2	1863 ± 6	4.7 ± 0.5
900	10.2	50 ± 2	2223 ± 21	6.7 ± 0.6
900	10.2	66 ± 3	2170 ± 11	6.4 ± 0.6
900	10.2	79 ± 3	1763 ± 2	4.2 ± 0.5
900	6.2	37 ± 2	1672 ± 4	6.3 ± 0.7
950	1.2	66 ± 2	1887 ± 7	41 ± 4
950	2.2	66 ± 2	2381 ± 4	36 ± 3
950	4.2	66 ± 2	2611 ± 6	22 ± 2
950	8.2	66 ± 2	3029 ± 5	15 ± 1
950	8.2	150 ± 6	3618 ± 63	22 ± 1
1000	8.2	27 ± 1	5128 ± 17	44 ± 2
1000	8.2	54 ± 2	5617 ± 27	53 ± 2
1000	8.2	80 ± 3	5039 ± 5	43 ± 2
1000	8.2	84 ± 3	4957 ± 17	42 ± 2
1000	8.2	100 ± 4	5859 ± 48	58 ± 2
1000	8.2	100 ± 4	5442 ± 29	50 ± 2
1000	8.2	108 ± 4	5116 ± 50	44 ± 2
1000	1.2	66 ± 3	2227 ± 4	57 ± 5
1000	2.2	66 ± 3	3066 ± 7	59 ± 4
1000	4.2	66 ± 3	3892 ± 17	50 ± 3
1000	8.2	66 ± 3	5832 ± 22	58 ± 2
1050	1.2	66 ± 3	3549 ± 14	146 ± 8
1050	2.2	66 ± 3	4942 ± 20	154 ± 6
1050	2.2	149 ± 6	4839 ± 15	148 ± 6
1050	6.2	199 ± 8	7770 ± 20	135 ± 4
1050	10.2	25 ± 1	8778 ± 84	105 ± 2

Table 3.2: List of diffusion conditions, fitting parameter and calculated diffusion coefficient, for diffusion profiles without residual phase fitted with gaussian function. Duration are corrected according to the assumption explained in the text.

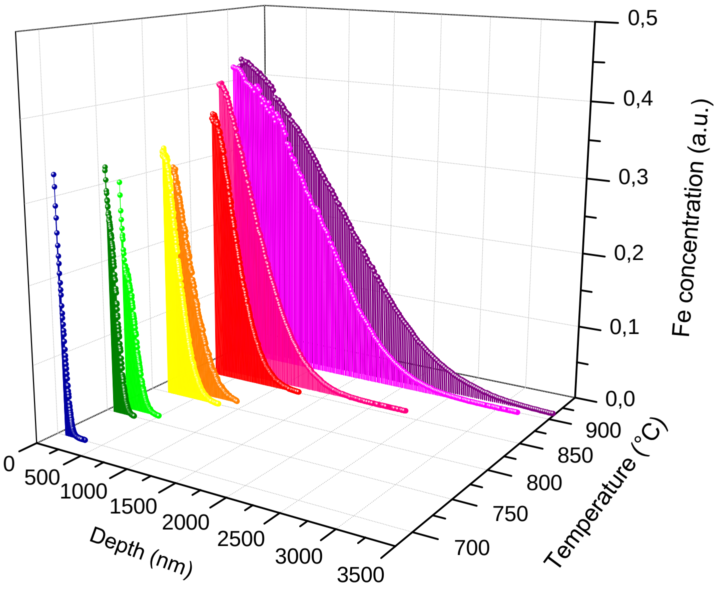

Figure 3.12: Concentration of Fe as a function of depth and temperature, in the case of non-exhausted source. The diffusion profiles get gradually deeper and higher as the temperature increases. The tail of these profiles was fitted with erfc function to derive the diffusion coefficient in the 700 °C - 850 °C temperature range.

Diffusion coefficient with non-exhausted source

All the samples with residual layer underwent SIMS measurements with high sputtering rate, as described in section A.2.1, in order to draw the whole diffusion profile of Fe after erosion of the residual layer. The results are shown in figure 3.12, where the Fe signal is plotted as a function of depth and temperature. As expected, the profile gets deeper and deeper as temperature and duration of the annealing increase. Sample annealed at 600 °C is excluded since there was no diffusion. For the samples annealed in the range 700 °C - 850 °C, the system has a non-exhausted source of diffusing species (the residual layer), therefore at a first approximation the diffusion profile should be described using equation 3.4. Unfortunately, due to the anomalous yields of secondary ions after erosion of the residual layer (see section A.4.3), the signals in the first 100 nm - 200 nm are not reliable, and erfc function did not fit them well. However, if the region with anomalous yield is discarded, and only the tails of the profiles are fitted with erfc function, the fitting curve shows a good compatibility with experimental data and, from the fitting parameter w of erfc function, the diffusion coefficient can be determined: the values are reported in table 3.2 together with values derived from gaussian fit.

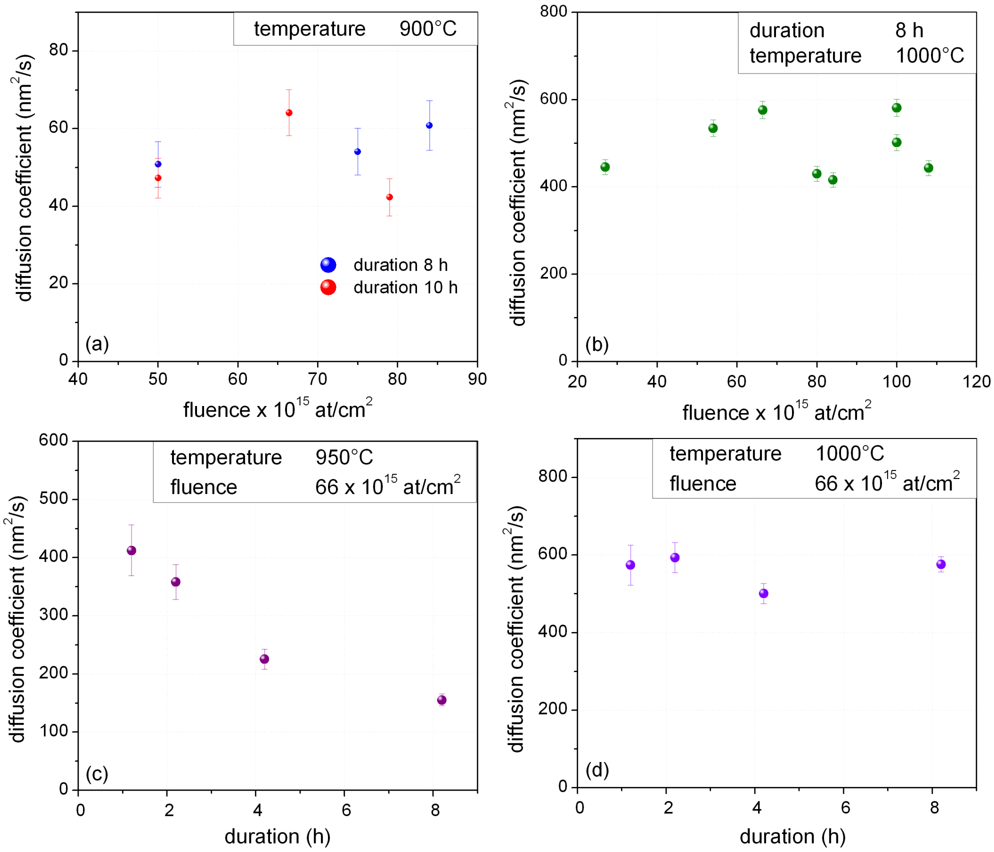

Figure 3.13: Diffusion coefficients plotted as a function of fluence at constant duration (a and b) and as a function of duration at constant fluence and constant temperature(c and d).

temperature (°C)	diffusion coefficient ($\mu m^2 s^{-1}$)
900	$(0.056 \pm 0.009)\ 10^{-3}$
950	$(0.27 \pm 0.10)\ 10^{-3}$
1000	$(0.51 \pm 0.07)\ 10^{-3}$
1050	$(1.3 \pm 0.2)\ 10^{-3}$

Table 3.3: Mean values of diffusion coefficient for the four temperatures considered.

3.4.3 Discussion

By looking at the values of D in table 3.2, it immediately stands out that data are quite scattered. Given a certain temperature, the diffusion coefficient has not the same value for all the samples. According to the phenomenological approach, equations 3.3, 3.4 and 3.6 hold only when the diffusion coefficient does not depend on concentration.

In our experiments, given the same fluence and the same temperature, the concentration of dopant at a certain point $C(x)$ gets lower as the duration of the treatment increases: thus by looking at the dependence of D on duration, there should be an indirect signature of the dependence of D on concentration. This can be made clear by plotting D for samples with the same fluence (66×10^{15} at/cm^2) and same diffusion temperature (950 °C) as a function of duration (figure 3.13 a): D decreases ad the duration increases, whereas the same plot (figure 3.13 b) for samples diffused at 1000 °C does not show any clear dependence. Also the dependence on the fluence can bring a signature of a dependence of D on concentration: it was investigated by plotting D vs fluence for samples with the same diffusion duration (8 h) and same temperature (900 °C, 1000 °C): D and fluence seem to be uncorrelated.

It stands out that the estimated experimental errors do not account the large scattering of data. Probably there are many variables which affect the diffusivity of Fe, which are not easily reproducible. For instance, the amount of vacancies, which is fundamental in determining diffusion, varies during the thermal treatment due to Li out-diffusion; the quality of the interface between the substrate and the oxidised layer may affect the dynamics of the mass transport through it; also the partial pressure of gases inside the furnace may play a role in diffusion dynamics. In conclusion, from these data no clear indication about the dependence of D on experimental parameters stems out, as a consequence no conclusion can be inferred about the presumed dependence on the concentration. Finally, the most representative values that can be extracted from this investigation are the mean values and standard deviations of D at each temperature.

The mean values of D obtained are listed in table 3.3. Unfortunately, there are only two published data to compare these values with. They refer to Fe diffusion in y-cut $LiNbO_3$ substrates, under oxidising atmosphere, prepared in two different laboratories. Since according to symmetry considerations [24], diffusion along x direction should not differ from diffusion along y, it makes sense to compare those data with the ones presented here. The first datum from Kip at al. [26] was calculated after one diffusion experiment lasted 18 h at 1000 °C in wet oxygen: the diffusion coefficient resulted $(9 \pm 1) \times 10^{-4}$ $\mu m^2 s^{-1}$. The second datum from Bashkirov and Shandarov [27] refers to diffusion in air at 1000 °C with different durations ($1 \div 5$ h) and the diffusion coefficients obtained are in the range $(3 \div 5) \times 10^{-4}$ $\mu m^2 s^{-1}$. Diffusion coefficient values at 1000 °C obtained in the present work are in the range $(4 \div 6)\ 10^{-4}$ $\mu m^2 s^{-1}$, consistent with the datum from Bashkirov and Shandarov, but smaller than the datum from Kip et al., although in the same order of magnitude. Discrepancies can be ascribed not only to different experimental conditions, but also to the fact that, since D depends exponentially on temperature, a small underestimation of temperature leads to a significantly higher diffusion coefficient: as a matter of fact, a difference of only 25 °C between real and measured temperature can account for the difference between our mean value $5\times\ 10^{-4}$ $\mu\mathrm{m}^2\mathrm{s}^{-1}$and the value from Kip et al. $9\times\ 10^{-4}$ $\mu\mathrm{m}^2\mathrm{s}^{-1}$. In conclusion, values of D here presented are reasonably in agreement with previous data.

3.5 Activation energy

As already mentioned, the diffusion coefficient should obey Arrhenius' equation 3.2, therefore the activation energy can be obtained from fitting diffusion coefficient as a function of temperature. Data points were therefore put in a semilogarithmic plot, as a function of the reciprocal thermal energy $1/kT$, in figure 3.14. As a matter of fact data points for a certain temperature span a relatively large range, but their trend as a function of $1/kT$ allows an estimation of the activation energy, although the uncertainty may be high. If only gaussian profiles are considered, the linear fit gives

$$E_{\mathrm{att}} = (2.8 \pm 0.1)\mathrm{eV}$$

If also samples with residual layer are considered, whose D values are derived by fitting only a part of the diffusion profiles, although these values are much less reliable, they are rather well aligned with the other. The linear fit of all the data points gives

$$E_{\mathrm{att}} = (3.10 \pm 0.07)\mathrm{eV}$$

however, as explained in section 3.1.2, since for lithium niobate two temperature regimes are distinguishable, it is not justifiable to hazard a fit spanning such a wide temperature range. Since significant diffusion depth can be obtained at temperatures above 900 °C, the first estimation $E_{\mathrm{att}} = (2.8\pm0.1)\mathrm{eV}$, apart from being more reliable, is more useful for practical purposes. This value can be compared with activation energies of other transition metals: 1.77 eV for Cu, 2.08 eV for Ni, 1.85 ÷ 3.08 eVfor Ti (data taken from [24]).

As already mentioned in section 3.1.2, diffusion in LN occurs through vacant sites. As a consequence, diffusivity and activation energies depend strongly on vacancies concentrations, as stated by equation 3.7, which in turn depend on temperature and stoichiometry. As a consequence, even if the molar fraction of Fe is typically very low in the samples considered (less than 1 mol%), the approximation of constant diffusivity, which often holds in the case of low impurity concentration, is not justified at all because these concentrations are comparable with vacancies concentration (3.9 mol%). Moreover, on a surface exposed to high temperature the vacancies concentration is expected to change, as will be explained in chapter 6, therefore one should monitor how the stoichiometry changes during the diffusion treatment in order to describe correctly this phenomenon. In summary, to investigate thoroughly the diffusion process more controllable conditions and more advanced equipment are required. Although diffusion of Fe could not be modelled, indicative values of diffusivity and activation energies were found, that are very useful for practical purposes.

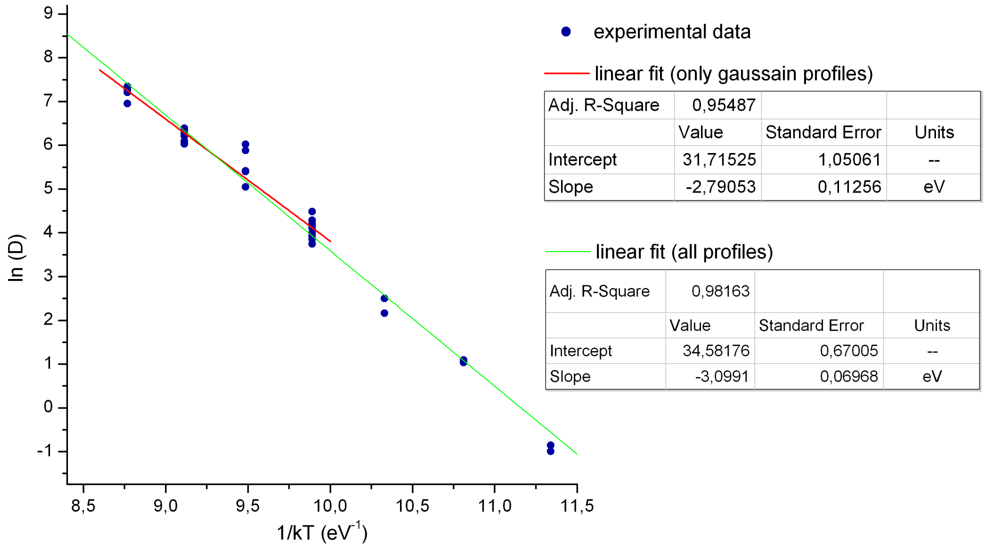

Adj. R-Square	0,95487		
	Value	Standard Error	Units
Intercept	31,71525	1,05061	--
Slope	-2,79053	0,11256	eV

Adj. R-Square	0,98163		
	Value	Standard Error	Units
Intercept	34,58176	0,67005	--
Slope	-3,0991	0,06968	eV

Figure 3.14: Diffusion coefficient data in logarithmic scale plotted vs reciprocal energy 1/kT. Red line: exponential fit of data points that refer only to gaussian profiles. Green line: exponential fit of all data points, including those obtained from profiles with residual layer fitted with erfc function. From the slope of the fitting line, the activation energy is given.

Chapter 4

Iron-diffused LN characterisation

This chapter describes all the characterisations performed on iron diffused wafers.

Known the concentration of iron from SIMS, it is necessary to evaluate its degree of reduction, i.e. to know whether it is Fe^{2+} or Fe^{3+}. As already seen in section 1.5.2, Fe^{2+} absorbs green light, while Fe^{3+} does not, so optical absorption measurements were performed. The absorption spectrum can be exploited to estimate qualitatively the valence state and, under certain conditions, also a quantitative determination of the Fe^{2+} content. The analysis of the absorption spectra suggests also a new way to determine the total Fe concentration regardless of the valence state, which was never considered before. This method may turn out to be the simplest and quickest way to measure Fe concentration, provided it is not too high.

The location of Fe in the LN lattice was also investigated. The atom location of Fe has already been done on bulk doped LN [14], establishing that Fe substitutes for Li, but doping by thermal diffusion is different from growing crystal from doped melt, therefore it should not be taken for granted that the site is the same.

The effect of iron on the matrix was also investigated from the structural point of view, using High Resolution X-Ray Diffraction (HRXRD), and looking at lattice parameter variation and lattice disorder.

Depth-resolved Raman and polaron luminescence measurements were also performed, to achieve better understanding of the defect structure and how it is changed by Fe doping or by thermal treatments. Both these measurements are made within a collaboration with the university of Metz (France).

4.1 UV-vis spectroscopic characterisation

The features in Fe:LN absorption spectra were already described in section 1.5.2. In particular, absorption spectra can be exploited to find out the reduction degree of iron, using the proportionality between Fe^{2+} concentration and ordinary absorption coefficient at two wavelengths, 532 nm and 477 nm. The absorption cross section of Fe^{2+} at 477 nm is [18]

$$\sigma_{(477)} = \frac{1}{2.16 \times 10^{21}\mathrm{m}^{-2}} = 4.63 \times 10^{-18}\mathrm{cm}^2$$

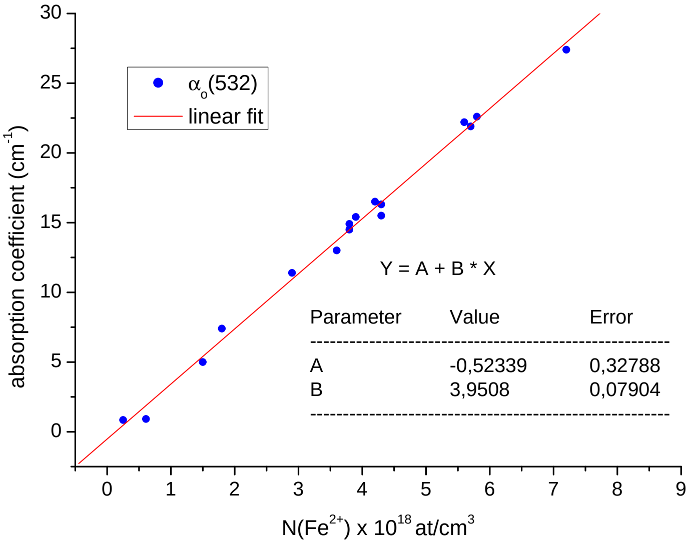

Parameter	Value	Error
A	-0,52339	0,32788
B	3,9508	0,07904

Figure 4.1: Absorption coefficient data of Fe:LiNbO$_3$ at 532 nm as a function of Fe concentration, taken from ref. [19] and fitted to a linear law.

The cross section at 532 nm may be easily calculated from data in ref. [19]. The linear fit of data of absorption coefficient plotted versus the concentration gives the following cross section:

$$\sigma_{(532)} = (3.95 \pm 0.08) \times 10^{-18}\text{cm}^2 \tag{4.1}$$

so the number of Fe^{2+} atoms is given by

$$N^{Fe^{2+}}[\text{cm}^{-3}] = \frac{\alpha[\text{cm}^{-1}]}{\sigma[\text{cm}^2]}$$

It seems preferable to exploit absorption at 532 nm rather than 477 nm to determine Fe^{2+} concentration, because this second wavelength is too close to 483 nm, wavelength at which also Fe^{3+}, if present, absorbs. Apart from the D band, the whole spectrum was studied and important features arose. Description and experimental details on the measurements and data analysis procedure are reported in appendix B.

4.1.1 Oxidised samples

Sample which underwent diffusion in oxygen without further treatments show absorption spectra as those plotted in figure 4.2. D band, the absorption band associated to Fe^{2+}, is absent or has a very low intensity, indicating that these samples contain almost only Fe^{3+}. The F band, the narrow band at 483 nm associated to a spin transition of Fe^{3+}, is present but not visible in the spectra due to the small amount of Fe atoms. Concerning the C band, as already mentioned, its intensity is high and under the present experimental conditions only the edge of this band is measurable. For this reason, it is not possible to perform a fitting to separate this band from the energy gap band, to find the centre and to estimate correctly its intensity. Nevertheless, in figure 4.2 a proportionality can be recognised between absorption in the spectral range from 330 nm to 350 nm and Fe^{3+} concentration, which in this case corresponds to total Fe

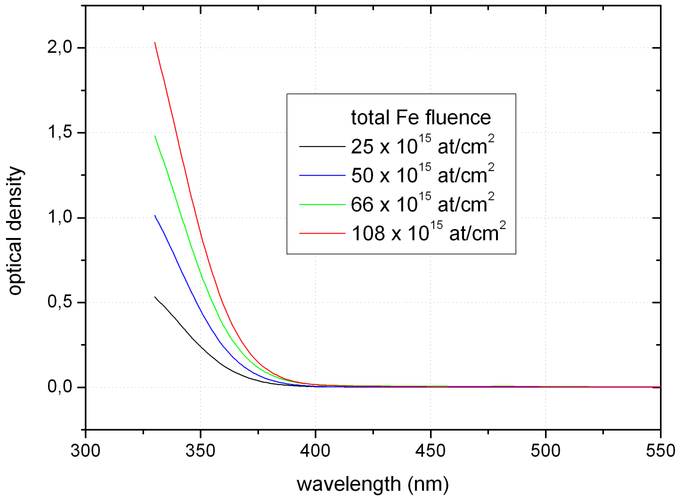

Figure 4.2: Absorption spectra of four oxidised samples with different Fe fluence.

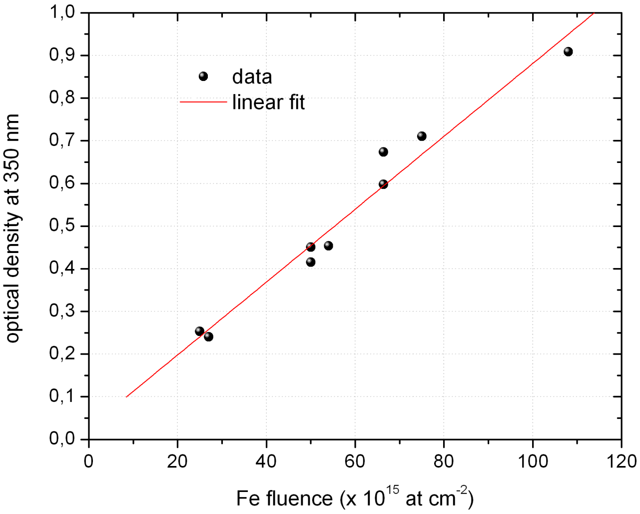

Figure 4.3: Optical density at 350 nm of oxidised samples, plotted as a function of Fe^{3+} concentration and fitted with a line.

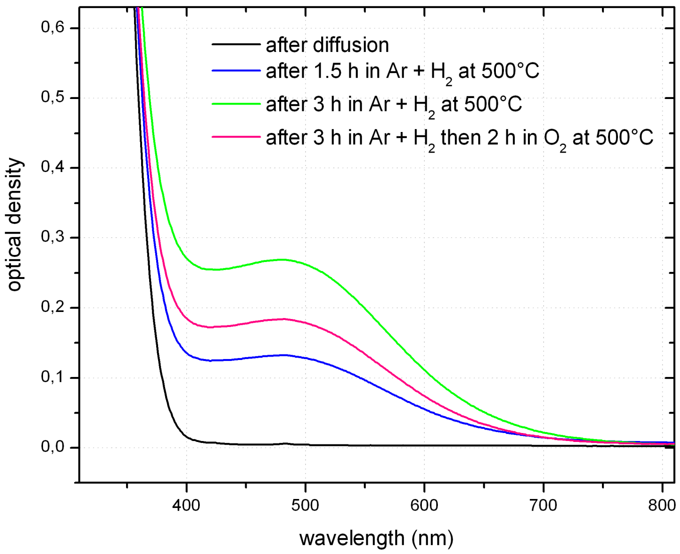

Figure 4.4: Optical density spectra of a sample right after diffusion in oxygen (black line); after first reducing treatment (blue line); after second reducing treatment (green line); after reoxidation (red line).

concentration. Since measurements are performed in transmission, the total Fe concentration to be considered is that obtained from RBS measurements[1]. For instance, on a plot (figure 4.3) of the optical density at 350 nm as a function of the nominal fluence of Fe atoms deposited, a linear relation fits well the data.

It is worth to mention that nominally pure commercial wafers of LN may contain Fe impurities up to 2 ppm. In a “pure” wafer 1 mm thick, there may be up to 3.8×10^{16} atoms per square centimetre, a number which is not negligible at all compared to the number of Fe atoms diffused (more than 2.5×10^{16}). As a consequence, one would expect the fitting line in graph 4.3 to have a large positive intercept. On the contrary the intercept of the fitting line is close to zero because, as explained in appendix B, the absorption spectra of Fe-doped wafer are normalised to a “pure” LN spectrum, thus the contribution of native Fe atoms is cancelled.

4.1.2 Reduction degree

One of the fundamental tasks of this work is to obtain a material with the desired Fe^{2+}/Fe^{3+} ratio. As already mentioned in section 1.5.2, the intensity of D band in ordinary polarisation can be used to measure Fe^{2+} concentration. The total concentration of Fe is known, therefore the Fe^{2+}/Fe^{3+} can be determined. By way of example, spectra of the same sample undergone different reducing treatments are discussed.

First, 108 $\times 10^{15}$ at/cm^2 of Fe were deposited on this sample, then diffused in oxygen at 1000 °C for 10 hours. Its absorption spectrum after diffusion is shown in figure 4.4 (black line). After a first reducing treatment performed in Ar + H_2 at 500 °C for 1.5 hours, the D band rises up (blue line); after a second treatment equal to the latter, intensity of D band further increases. In order to prove that reduction

---

[1] Here it is assumed that all the Fe atoms deposited by magnetron sputtering do diffuse in the substrate, without evaporation, as supported by DTA and PIXE measurements.

treatment	OD at 532 nm	Fe^{2+} amount	Fe^{2+}/Fe^{3+} ratio
after diffusion	0.004	1 x10^{15} at/cm^2	0.009
after 1.5 h Ar + H_2	0.111	28 x10^{15} at/cm^2	0.35
after 3 h Ar + H_2	0.228	58 x10^{15} at/cm^2	1.16
after 3 h Ar + H_2 then 2 h in O_2	0.155	39 x10^{15} at/cm^2	0.56

Table 4.1: Optical density data of a sample containing 108 x10^{15} at/cm^2 of Fe undergone several thermal treatments. By using the known cross section of D band at 532 nm, the amount of Fe^{2+} and the Fe^{2+}/Fe^{3+} ratio were calculated.

is reversible, another treatment at the same temperature was performed in oxygen for 2 hours: the D band indeed decreases. From the OD at 3532 nm the Fe^{2+} total amount can be calculated and, by using the total Fe fluence, also the ratio Fe^{2+}/Fe^{3+}: data are reported in table 4.1. As a matter of fact, the oxidised sample contains a negligible amount of Fe^{2+}; the adopted reduction/reoxidation treatments at 500 °C allow to vary Fe^{2+}/Fe^{3+} ratio in a wide range in a reversible way.

4.1.3 Isosbestic point at 342 nm

By observing the ultraviolet region of absorption spectra of the same sample with different reduction degrees, one can realise that, as the intensity of D band increase with the reduction degree, the intensity of C band seems to decrease. These two bands overlap in the range of wavelengths 330 nm - 400 nm. By comparing spectra of samples with same total Fe amount but different reduction degrees, all the spectra cross each other at approximately 342 nm: two examples are shown in figure 4.5. The same wavelength is found for all the concentrations, it can be thus concluded that it is a kind of isosbestic point, at which the rise of D band and the fall of C band compensate each other exactly.

This fact has an important implications: the absorption at 342 nm does not depend on the valence state, but depends only on the number of Fe atoms. A large number of samples, listed in table 4.2, was considered: they differ not only in fluences, but also they underwent different diffusion annealings, so they have different concentration and different profiles, and they also have different reduction degree due to the reducing post-treatments. The plot in figure 4.6, which contains all the optical density data at 342 nm of these samples versus the Fe fluence, shows that data are well fitted with a linear relation, indicating that absorption depends likely only on the fluence.

In order to verify the absence of correlation between optical density at the isosbestic point and the reduction degree, the optical density values divided by the fluence were plotted as a function of the reduction degree: the latter was calculated from the optical absorption at 532 nm as usual, and its values for each sample are reported in table 4.2, expressed as percentage of Fe^{2+} over the total Fe amount. The plot in figure 4.7 (b) shows that there is no correlation with the reduction degree, confirming our former observation. Moreover, the maximum concentration at the surface, whose values are also reported in table 4.2, ranges from 0.1 mol% to 1.8 mol%, corresponding to minimum average distances between one Fe atom and another in the range from 3.7 nm to 1.4 nm. These concentrations are much higher than those used for photorefractive applications (typically 0.01 $\div$ 0.1 mol%). To ensure that there is no

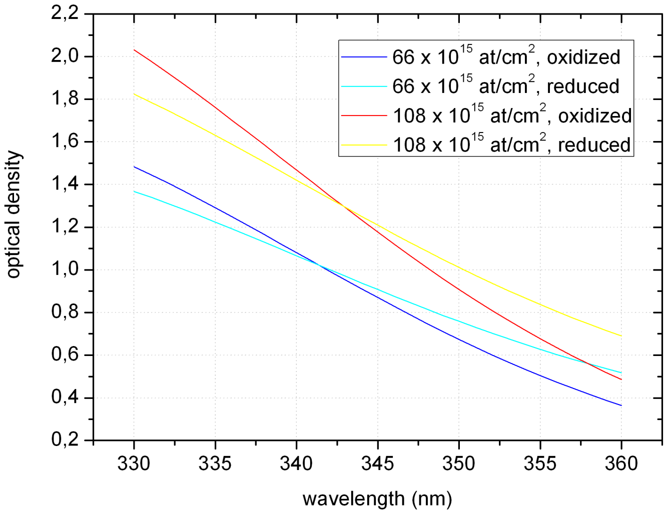

Figure 4.5: Optical density spectra of two samples with different fluences, each with two reduction degrees; the crossing point is at about 342 nm for both.

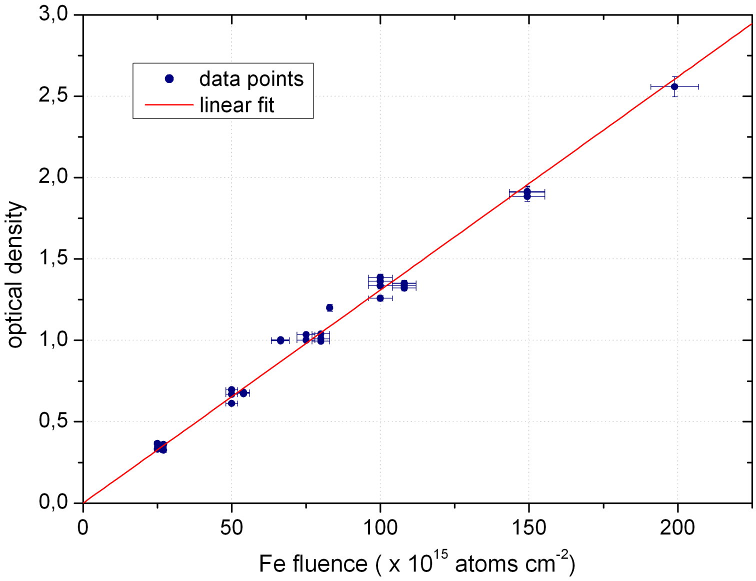

Figure 4.6: Optical density data at 342 nm for samples with different fluences and different reduction degrees, plotted as a function of Fe fluence and fitted with a line passing through the origin.

Fluence 10^{15} at/cm^2	Thermal treatments	OD at 342 nm	$C_{\mathrm{Fe\ sup}}$ 10^{20} at/cm^3	Reduction degree $\mathrm{Fe}^{2+}/\mathrm{Fe}$ %
25 ± 1	40 h at 1000 °C in O_2	0.36 ± 0.01	0.19	3
	+ 6 h at 500 °C in Ar + H_2	0.33 ± 0.01		100
27 ± 1	8 h at 1000 °C in O_2	0.36 ± 0.01	0.44	1
	+ 1.5 h at 500 °C in Ar + H_2	0.33 ± 0.01		75
50 ± 2	8 h at 900 °C in O_2	0.67 ± 0.01	2.30	0
	+ 0.5 h at 500 °C in Ar + H_2	0.69 ± 0.01		50
50 ± 2	10 h at 900 °C in O_2	0.61 ± 0.01		0
54 ± 2	8 h at 1000 °C in O_2	0.68 ± 0.01	0.78	0.5
	+ 1.5 h at 500 °C in Ar + H_2	0.68 ± 0.01		21
	+ 1.5 h at 500 °C in Ar + H_2	0.67 ± 0.01		100
66 ± 3	10 h at 900 °C in O_2	0.99 ± 0.02	2.30	1.5
	+ 1.5 h at 500 °C in Ar + H_2	1.00 ± 0.02		39
	+ 0.5 h at 500 °C in Ar + H_2	1.00 ± 0.02		58
75 ± 3	8 h at 900 °C in O_2	1.03 ± 0.02	3.40	6
	+ 1.5 h at 500 °C in Ar + H_2	1.00 ± 0.02		50
80 ± 3	8 h at 1000 °C in O_2	0.99 ± 0.02	1.26	0
	+ 1.5 h at 500 °C in Ar + H_2	1.04 ± 0.02		25
	+ 1.5 h at 500 °C in Ar + H_2	1.01 ± 0.02		96
100 ± 4	8 h at 1000 °C in O_2	1.33 ± 0.02	1.44	0
	+ 1.5 h at 500 °C in Ar + H_2	1.39 ± 0.02		36
	+ 1.5 h at 500 °C in Ar + H_2	1.36 ± 0.02		50
108 ± 4	8 h at 1000 °C in O_2	1.35 ± 0.02	1.75	1
	+ 1.5 h at 500 °C in Ar + H_2	1.33 ± 0.02		26
	+ 1.5 h at 500 °C in Ar + H_2	1.35 ± 0.02		53
	+ 3 h at 500 °C in O_2	1.32 ± 0.02		36
149 ± 6	2 h at 1050 °C in O_2	1.91 ± 0.04	2.50	0
	+ 1.5 h at 500 °C in Ar + H_2	1.91 ± 0.04		40
149 ± 6	8 h at 950 °C in O_2		3.10	
	+ 1.5 h at 500 °C in Ar + H_2	1.88 ± 0.03		47
199 ± 8	6 h at 1050 °C in O_2	2.56 ± 0.06		0

Table 4.2: List of samples employed for the analysis of absorption at 342 nm.

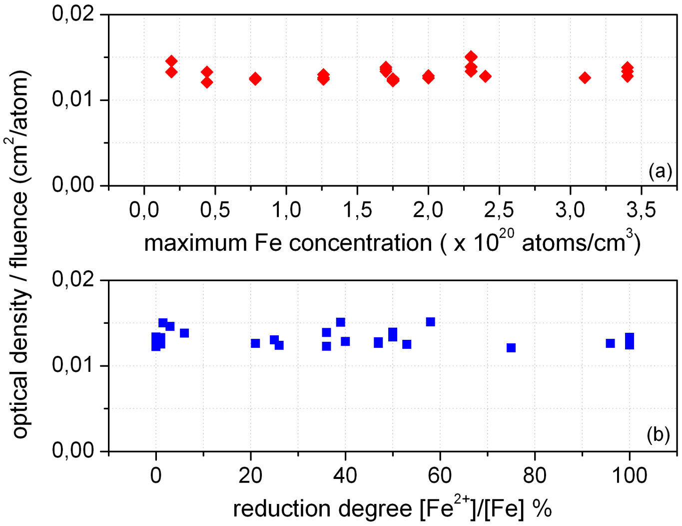

Figure 4.7: For each sample, optical density divided by fluence, i.e. absorption cross section calculated for each measurement, is plotted as a function of (a) the surface Fe concentration, (b) the reduction degree of Fe, to show that there is no correlation.

effect of enhancement or inhibition of absorption due to the nearness of Fe atoms, the dependence of these results on the concentration was checked. By plotting the optical density divided by the fluence as a function of the maximum concentration (figure 4.7 (a)) no correlation can be recognised, therefore this result is likely valid also for lower concentration of Fe.

In conclusion, absorption measurements at the isosbestic point can be used to determine the total Fe amount in any sample, regardless the reduction degree. In other words, it is possible to define an effective absorption cross section at the isosbestic point, with which each Fe atom contributes, either only with C band if it is Fe^{3+}, or with D band and attenuated C band if it is Fe^{2+}. From the linear fit of data, this cross section is $\sigma_{(342)} = (13.1 \pm 0.2) \times 10^{-18}\mathrm{cm}^2$.

The presence of an isosbestic point ensures that only two species contribute to absorption. If a third species is partaking, spectra intersect at varying wavelengths. In the present case, other species which may absorb light in the visible range are polarons and bipolarons (see section 1.3.1) hence the importance of the isosbestic point is in ensuring in particular that polarons and bipolarons are absent. In other words, it is important to check the presence of the isosbestic point in order to estimate correctly the Fe^{2+} concentration because the absorption at 532 nm may contain contributions also from polarons and bipolarons.

4.1.4 Correction of absorption spectra

In many samples with low Fe doping or reduced for a short time, a high optical density in the region 700 − 800 nm is observed, moreover spectra do not intersect at 342 nm, indicating that species other than Fe are absorbing. If a sample of pure $LiNbO_3$ is treated in reducing gas, its absorption spectrum shows some absorption bands in the visible associated to transition involving Nb^{4+} bound polaron and bipolaron [5].

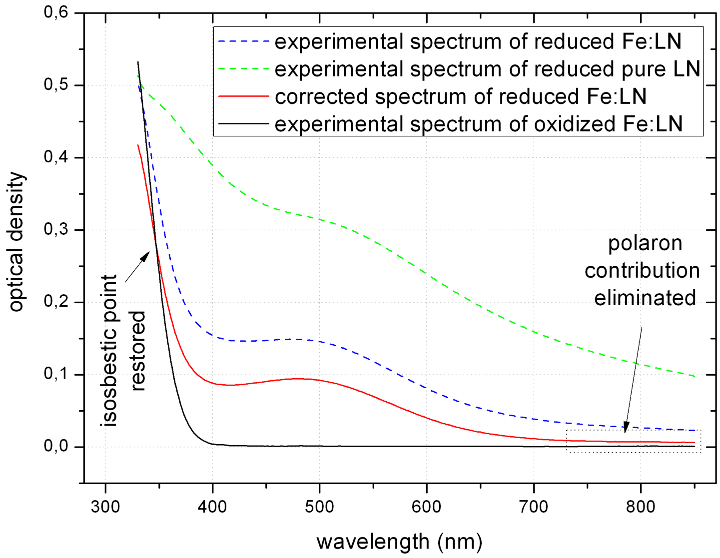

Figure 4.8: Example of correction of absorption spectra: the experimental spectrum of a reduced Fe:LN sample contains contributions from polaron and bipolaron bands. The spectrum of a reduced pure LN sample (green line), multiplied by a suitable constant (0.17), is subtracted from the spectrum of reduced Fe:LN. In the corrected spectrum (red line), compared to the spectrum of the same sample oxydized, the isosbestic point is restored to the correct wavelength and the absorption in the polaron region is reduced.

At room temperature both bands appear, giving an absorption spectrum like the green dashed spectrum shown in figure 4.8, which refers to a pure congruent $LiNbO_3$ sample reduced at 500 °C in N_2 and H_2 (4%) mixture for 4 hours. Assuming that the other species contributing in Fe:LN samples are polarons and bipolarons, and that their spectrum has the same shape as in undoped samples, it is possible to isolate the contribution of Fe absorption by subtracting from the optical density of Fe doped sample (blue dashed spectrum in fuigure 4.8) the optical density of an undoped reduced sample, multiplied by a convenient constant, so that the resulting spectrum (red solid line) has again the isosbestic point and low absorption in the $700 - 800\,\mathrm{nm}$ region. This procedure proved a posteriori to be correct since the resulting spectrum turns out to have the usual shape of Fe:$LiNbO_3$ absorption and calculation of Fe^{2+} concentration gives reasonable values. An example of this procedure applied on a sample containing $27 \times 10^{15}\mathrm{at/cm}^2$ is shown in figure 4.8.

4.1.5 Relation between post-treatment duration and reduction degree

A comparison between samples with different concentration but same profile and same reducing treatments was made to understand how the Fe^{2+} concentration depends on post-treatment duration. Data are reported in table 4.3. The first remark is that data are quite scattered: neither the Fe^{2+} areal density, nor the Fe^{2+} percentage are equal after the same reducing treatment. But the most striking feature is that after 1.5 h of reducing treatment *all* the spectra needed to be corrected for polaron absorption, while

fluence	OD after 1.5 h of reduction	OD after 3 h of reduction
27×10^{15} at/cm^2	0.08 (corr.)	-
54×10^{15} at/cm^2	0.05 (corr.)	0.23
80×10^{15} at/cm^2	0.05 (corr.)	0.30
100×10^{15} at/cm^2	0.11 (corr.)	0.20
108×10^{15} at/cm^2	0.11 (corr.)	0.23

Table 4.3: Optical density values at 532 nm of samples which underwent the same two reducing steps. After the first reducing step, all the spectra needed to be corrected for polaron contribution.

none of them needed correction after 3 h of reducing treatment. This feature suggests that not only the reduction degree depends upon duration of reducing treatment, but also the distribution of electrons in the sample, i.e. as the time spent at 500 °C goes on, the electrons distribution between Fe level and polaron level changes. This feature will be further discussed in detail in section 6.1.5

4.2 Lattice site of Fe

As already mentioned, there are many works that proved, by means of different techniques, that Fe substitutes for Li in bulk doped LN. In particular, ion beam analysis in channeling conditions, combined with PIXE and nuclear reaction, showed that by choosing proper channeling directions which allow the ion beam to hit Li sites in the centre of the channel, a flux peak of Fe PIXE signal appears, ensuring that Fe locates mainly of Li site [14]. However it must be underlined that those investigations involved bulk doped $LiNbO_3$ grown from melt. This means that the structure accommodates the dopant while it forms, assuming the most stable configuration at the melting temperature. When the dopant is introduced by diffusion, it has to find place in an already established structure, hence the final configuration may differ from the one of a bulk doped. In order to check if the diffusion doping places Fe atoms in different sites, the same PIXE - channeling experiment was here performed at INFN (Legnaro) by N. Argiolas and D. De Salvador with two diffused samples, whose surface concentration was 0.93 mol%, one containing mainly Fe^{3+}, the other containing mainly Fe^{2+}, in order to compare the results.

The experiments were carried out using the 2.5 MV AN2000 Van de Graaff accelerator, with a 2 MeV H^+ beam, and the channeling direction chosen was along the plane (0 0 0 1). Several spectra of PIXE and RBS were acquired changing the angle of incidence of the beam in the XZ plane in the range (-0.6 °- +0.6 °), and by plotting the integral RBS signal of Nb, the usual channeling dip was observed (figure 4.9); the integral of Fe PIXE signal for both samples displays exactly the same flux peak observed by Rebouta et al. [14] on bulk doped Fe:LN. It can be concluded that also after diffusion both Fe^{3+} and Fe^{2+} locate at the Li site.

4.3 Surface topography

The surface of the samples has been observed before and after treatments by Atomic Force Microscopy (AFM) with a Veeco CP-II microscope; the investigated area is 5µm × 5µm and the measurements were carried out in contact mode. Data were

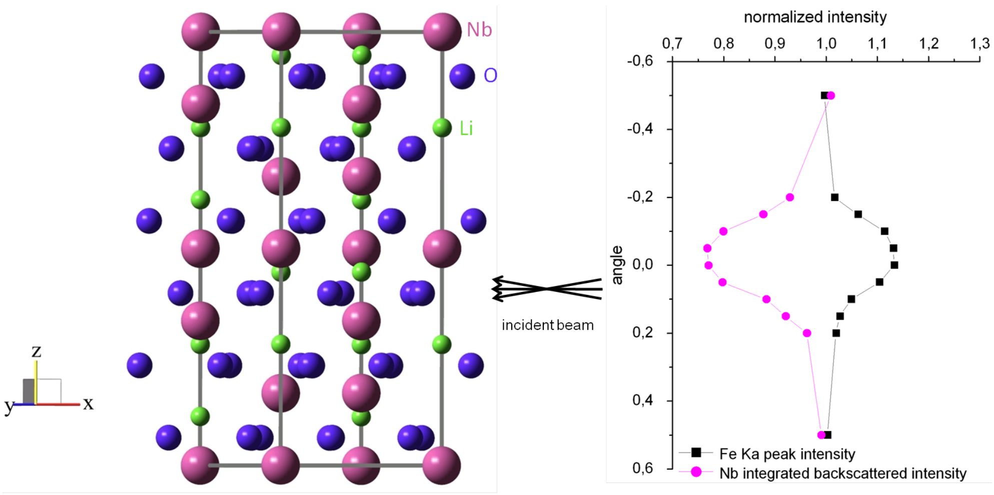

Figure 4.9: Scheme of PIXE measurement. The incident beam was directed along the X direction spanning a small angle interval in the XZ plane; when the incident beam gets channeled in the (0 0 0 1) plane, Nb backscattered signal shows a minimum, while Fe signal shows a peak, indicating that Fe ions locate in the middle of the channel created by Nb atoms, presumably on Li site.

recorded both maintaining constant force on the tip and acquiring the surface topography, and at constant height of the sample while measuring the variation of force on the tip: after cross-checking, the latter is reported. The first kind of measurements permits to estimate the height of the observed surface features but with the second kind the sensitivity is increased.

The samples investigated are six, obtained after diffusion at 900 °C for 10 h, under six different atmospheres:

- dry oxygen;
- wet oxygen;
- dry argon;
- wet argon:
- dry oxygen followed by dry reduction under $N_2 + H_2$ at 500 °C for 4 h;
- wet oxygen followed by wet reduction under $N_2 + H_2$ at 500 °C for 4 h.

Measurements were carried out both on the doped surface and on the undoped one, for comparison. AFM images obtained are tabulated in figure 4.10. Most of the surfaces investigated, except some dirt particle, are flat below few nanometres which is the sensitivity of the microscope, whereas on the doped face of samples treated in dry atmosphere, the formation of a topographic structure, with heights of about tenths of nanometres, is evident. These structures, whose size is about a hundred nanometres, have rectangular shape and they are oriented along the Z direction. Their formation is evidently connected with the presence of Fe, and inhibited by water vapour. These observations will be further commented in section 6.1.6.

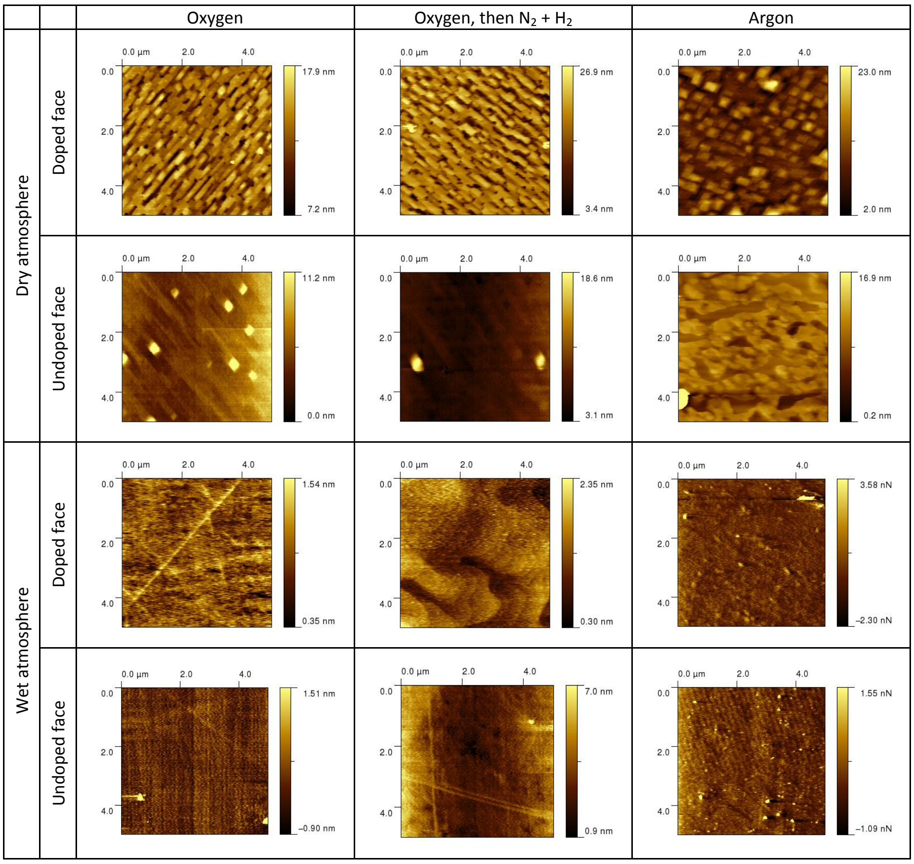

Figure 4.10: AFM images of the doped surface and undoped surface of six samples treated under different atmospheres.

4.4 Structural characterisation

Structural characterisation by means of HRXRD was exploited to investigate two aspects: lattice deformation and crystal disorder. Experimental details are given in appendix D. In the following discussion only the main results will be outlined, since the structural characterisation will be the subject of a PhD thesis by A. Zaltron.

4.4.1 Lattice mismatch in the doped layer

In order to look for deformation of the lattice along the diffusion direction, the diffraction peaks corresponding to the symmetrical reflections (1 1 0), (2 2 0) and (3 3 0) were investigated. The rocking curves showed the regular $LiNbO_3$ diffraction peak together with a shoulder peak at higher angles. This peak is present in all the three reflections investigated, and its angular distance with respect to the substrate peak indicates the existence of a layer with a lattice constant slightly smaller than the regular $LiNbO_3$ constant. The decrease of the lattice constant is attributed to Fe incorporation in the doped layer. A similar analysis performed on the (2 2 6) asymmetric reflection (not shown) points out that the Fe doped layer is pseudomorphous to the undoped substrate so that the deformation occurs only in the direction perpendicular to the surface. The doped material in its bulk state has in general a different lattice constants with respect to pure LN. When the doped lattice is constrained by pseudomorphism condition to the undoped substrate, the in-plane lattice constants are strained and, due to the off-diagonal elements of the elastic tensor, the perpendicular lattice constant is strained too. The interplanar distance d measured here by means of XRD corresponds to the strained lattice constant of the doped material, and its relative difference with respect to the substrate interplanar distance is the relative mismatch. According to general elasticity theory it is possible to envisage a linear relation between strain, defined as

$$\epsilon_\perp = \frac{d - d_\mathrm{R}}{d_\mathrm{R}} \tag{4.2}$$

and the mismatch

$$\xi_\perp = \frac{d - d_\mathrm{sub}}{d_\mathrm{sub}} \tag{4.3}$$

where d_R is the interplanar spacing of the doped layer in its fully relaxed state, and d_sub is the interplanar spacing of the undoped substrate. The decrease of the lattice constant is attributed to Fe incorporation in the doped layer. It is reasonable to assume that the decrease is roughly proportional to Fe concentration, which varies with depth in a semigaussian fashion, therefore the rocking curve observed is a results of the sum of contributions from each atomic plane with gradually decreasing compression going from surface to depth. In principle it is possible to simulate the rocking curve by considering a set of layers with different lattice constants and obtain the mismatch profile. Then it would be possible to compare mismatch profile and concentration profile and extract a relation. Work is in progress for the setup of a simulation program. For the moment, it suffices to consider the angular position of maximum intensity of the shoulder peak, assuming it refers to the maximum mismatch, i.e. to the surface where Fe concentration is higher. Mismatch values are easily calculated from Bragg's law according to formula 4.3.

In order to find a relation between concentration and mismatch, the maximum mismatch values must be related to the concentration values *at the surface*, which can

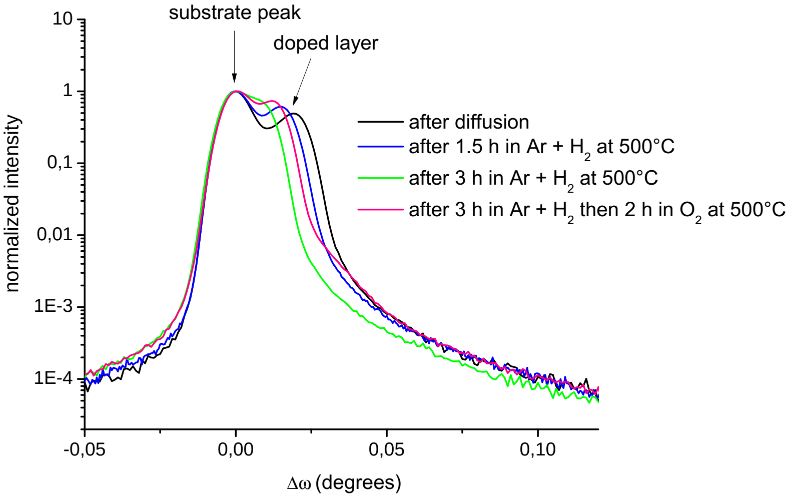

Figure 4.11: (3 3 0) rocking curves of a sample containing 108 x10^{15} at/cm^2 of Fe undergone several thermal treatments resulting in four different reduction degrees.

be extracted from normalised SIMS profiles. If only oxidised samples are considered, there is a linear relation between maximum mismatch and Fe^{3+} surface concentration. If a sample is partially reduced, the mismatch is smaller with respect to its oxidised state. By way of example, the same sample already mentioned in table 4.1 with four degrees of reduction is considered. The rocking curves displayed in figure 4.11 clearly show that the mismatch decreases as the reduction degree increases. Moreover, if mismatch is plotted as a function of optical density at 532 nm, which represents the reduction degree, the relation is linear, even after reoxidation: the mismatch depends on the valence state of Fe and is not influenced by former thermal treatments. It can be concluded that, at least for what concerns valence state and lattice deformation, oxidising and reducing treatments are completely reversible. The relation between mismatch and reduction degree will be further discussed in section 6.1.2.

4.4.2 Lattice disorder

HR-XRD can provide information about lattice disorder by means of reciprocal lattice maps, i.e. by measuring the diffracted intensity in the neighbourhood of a Bragg reflection in the reciprocal space. For experimental details, see appendix D. In the present work, reciprocal lattice maps were used to investigate the structural effects of the different atmospheres adopted for diffusion and reduction, both on the doped surface and on the back undoped surface of samples. The measurements were carried out on the same set of six samples treated under six different atmosphere, which underwent AFM measurements. Reciprocal lattice maps acquired on the doped face of the six samples are shown in figure 4.12. For all the maps two contributions can be clearly distinguished: a strong vertical truncation rod corresponding to the coherent scattering and a diffuse scattering peak corresponding to the incoherent scattering produced by the layer. Using the diffuse scattering peak as an indicator of the average quality of the surface it is immediately apparent that the samples treated in argon are the only ones whose structure is sensibly affected by the thermal treatments. All

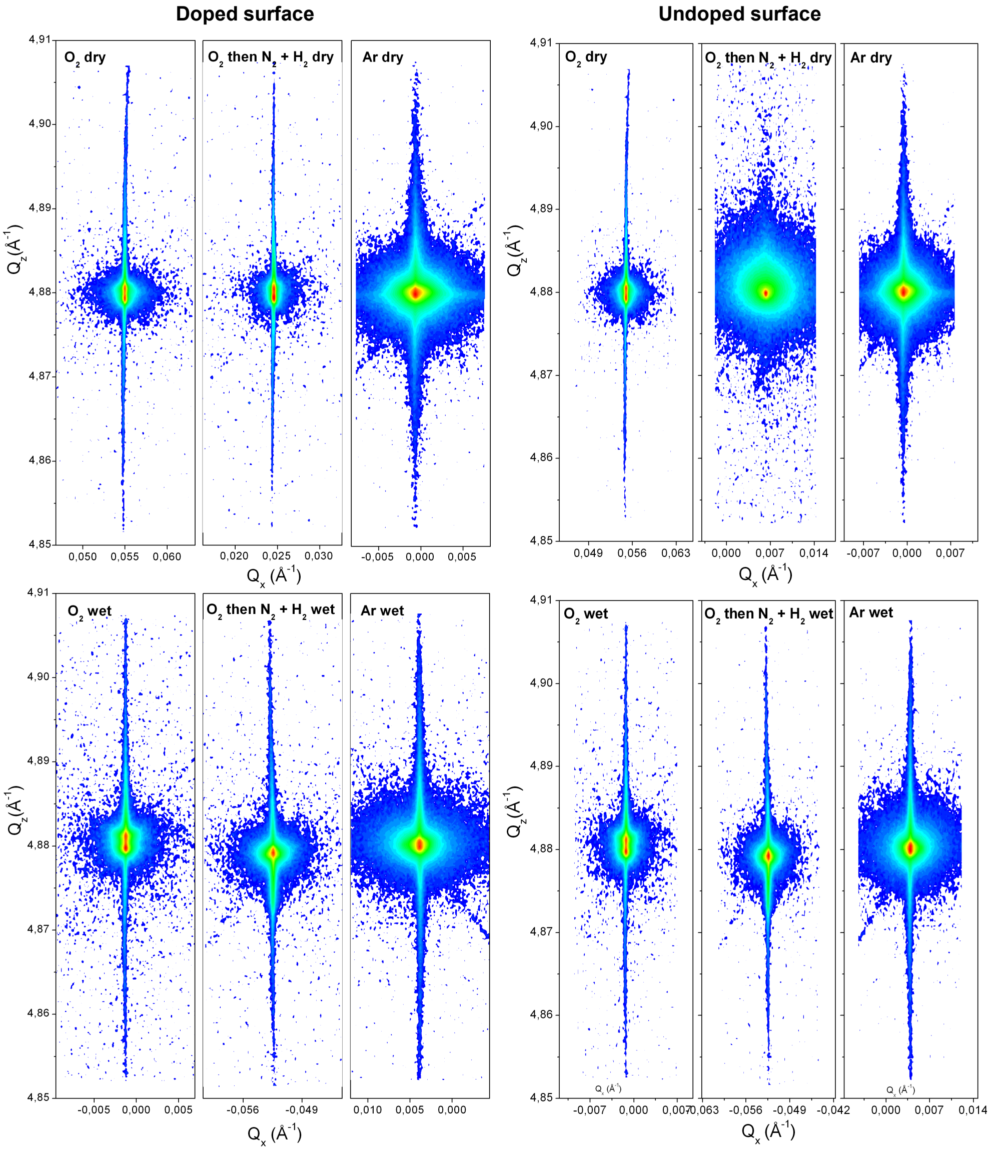

Figure 4.12: Reciprocal space map around the (2 2 0) reflection on the doped surface (left) and on the undoped surface (right) of six samples treated in different atmospheres.

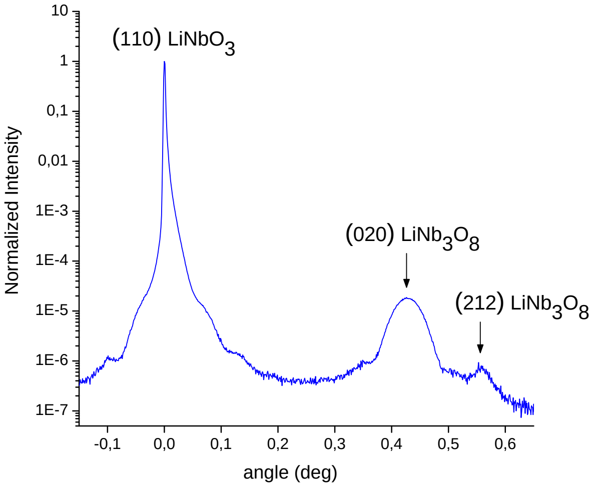

Figure 4.13: XRD ω - 2θ scan showing (1 1 0) diffraction peak of $LiNbO_3$ and two peaks due to Bragg reflections from $LiNb_3O_8$.

the other samples present a limited diffuse scattering indicating that the structure is practically identical for oxygen diffused and post-treated samples. Looking at the coherent part of the scattering, in all the samples, except in Ar treated ones, the truncation rods show two peaks due to the fact that the doped layer and the undoped substrate have a slightly different interplanar spacing along the vertical direction, as discussed in the previous section.

Since the back face of samples is not doped, in principle it's like investigating the effect of annealing in different atmospheres on the surface of pure LN. The reciprocal lattice maps acquired on the back face, shown in figure 4.12, indicate that the as-diffused samples both in dry and wet oxygen show only a moderate disorder while samples treated in both dry and wet argon have a more pronounced diffuse scattering peak. Finally the samples post-treated in $N_2 + H_2$ exhibit a marked difference between dry and wet treatments, the former introducing a much severe distortion than the latter, and in general much more than all other samples.

4.4.3 Lithium triniobate ($LiNb_3O_8$)

Several authors reported that the surface of lithium niobate may undergo damage after long, high temperature annealing, due to out-diffusion of lithium oxide, according to the reaction:

$$3LiNbO_3 \rightarrow LiNb_3O_8 + Li_2O \qquad (4.4)$$

The out-diffusion of lithium oxide causes lithium deficiency in the first atomic layers, which decompose in another phase, so called lithium triniobate ($LiNb_3O_8$). This new phase starts to grow by islands that were clearly visible by scanning electron microscopy [29]. $LiNb_3O_8$ formation was also reported during Ti diffusion [28] [30].

Also on some of the six samples considered in the previous discussion on lattice disorder $LiNb_3O_8$ was detected. Figure 4.13 shows a rocking curve acquired on the back face of sample annealed in dry argon: two peaks related to two different Bragg reflections of $LiNb_3O_8$ were detected, indicating the presence of a polycrystalline layer.

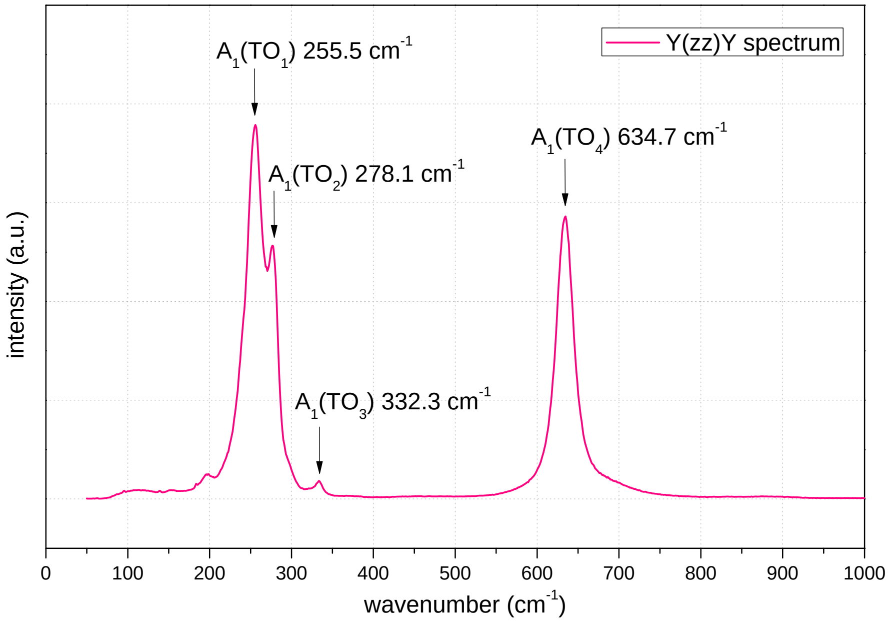

Figure 4.14: Raman spectrum of lithium niobate in Y(zz)Y configuration.

These peaks are present only on the back faces of samples treated in dry argon and in dry $N_2 + H_2$.

4.5 Raman spectroscopy

Raman scattering can afford a reliable technique to provide information not only about the structural quality of the whole lattice, but additionally about each sublattice. This gives important information about the defect structure of lithium niobate and on the role that a dopant has on it [31] [32]. Moreover, when used in combination with a confocal microscope, Raman spectroscopy can be used to obtain all the above mentioned information in a spatially resolved fashion, which makes this approach very convenient for the study of locally doped material.

For this study, the A_1(TO) phonons were considered, which correspond to ionic motions along the ferroelectric c axis. Three of these four phonons can be detected in the Raman spectrum by intense and well resolved peaks [33], as shown in figure 4.14. To probe each sublattice, the fact that each phonon A_1(TO) affords separate information is exploited. Indeed the $A_1(TO_1)$ phonon is associated to the out-of-phase motion of Nb ions against O ions, the $A_1(TO_2)$ is related to the vibration of Li and O ions in opposite directions, whereas the $A_1(TO_4)$ is related to the stretching of O ions. Therefore $A_1(TO_1)$ can probe the Nb sublattice, the $A_1(TO_2)$ is mainly sensitive to the A site (Li) and the $A_1(TO_4)$ is affected by any distortion of oxygen octahedron, and thus of the whole lattice. The line $A_1(TO_3)$ associated with the oxygen motion has generally a very small intensity, so that it cannot be used in the present approach.

These properties associated with Raman lines were earlier used in various investigations involving lattice dynamics of LN, in particular to study the incorporation mechanism of dopant ions in LN lattice. The substitution process depends on the nature and the content of intrinsic defects related to non-stoichiometry. Indeed the deficiency of Li in the A sites[2] is partly compensated by Nb antisites, which may leave some vacancies on Nb sites. As this defects are associated to A and B sites, the characteristics of $A_1(TO_1)$ and $A_1(TO_2)$ phonons are consequently investigated as function of doping concentration, to study the process of the introduction of extrinsic defects in LN. Furthermore it was shown that the $A_1(TO_1)$ can be used to evaluate the degree of non stoichiometry: when going from congruent to the stoichiometry the frequency slightly increases and the damping (or linewidth) strongly decreases [34]. The frequency increase can be related to a strengthening of chemical bonds, while the damping decrease is linked to a diminishing of the disorder in the lattice. A similar behaviour can be obtained by an appropriate doping of LN.

The behaviour of $A_1(TO_1)$, $A_1(TO_2)$ and $A_1(TO_4)$ phonons are analysed to investigate the influence of treatment and to control the quality of the crystal. The aim is to study the structural changes induced by thermal treatments and iron incorporation in lithium niobate.

4.5.1 Experimental

A confocal LabRam spectrometer was used in backscattering geometry: a scheme of this apparatus is shown in figure 4.15. A He-Ne laser emitting at 633 nm with 1 mW power was used as light source. The beam is focused on the sample by means of a 100× objective; the light scattered from the sample is collected by the same objective, filtered by a Notch filter to remove Rayleigh peak, dispersed by a 1800 tracks/mm grating, and finally detected by a CCD camera. Two polarisers provide the desired polarisation for respectively the incident beam and the scattered light. The Raman line of a Si crystal at $521\,\text{cm}^{-1}$ was used for spectrometer calibration at the beginning of any series of measurements in order to avoid any drift. The sample holder is equipped with a XYZ moving stage. An experimental configuration was chosen in order to perform an accurate in depth profile of the Raman modes evolution along the Fe diffusion profile. The confocal geometry (figure 4.16) allows to perform a scan along the X direction of the sample to provide depth resolved information. However, the region probed in this configuration is about 1 μm wide and, due to the high refractive index of LN, several μmdeep, therefore a depth dependent convolution of contributions from the Fe doped region with others coming from the underlying bulk substrate would be obtained. It is therefore preferable to perform a scan of the lateral face: in such way the lateral resolution is smaller and the scattering cross section remains constant for the different points along X. To perform Raman analysis by scanning the sample on the side faces, samples were carefully polished on the Y and Z faces. The Y(zz)Y configuration[3], which allows to obtain only the $A_1(TO)$ phonon modes under interest in this study, was adopted. Measurements were performed scanning along the crystallographic X direction with 1 μm steps, on the lateral Y faces, starting from the doped edge and moving towards the undoped one.

4.5.2 Results

A typical Raman spectrum obtained in Y(zz)Y configuration has already been presented in figure 4.14. Spectra are fitted with a sum of damped harmonic oscillators.

---

[2] A refers to the octahedral site normally occupied by Li, whereas B refers to site normally occupied by Nb.

[3] In this notation, upper-case letters indicate the direction of propagation of respectively the incident beam and the scattered beam, whereas the lower-case indicate the directions of polarisation.

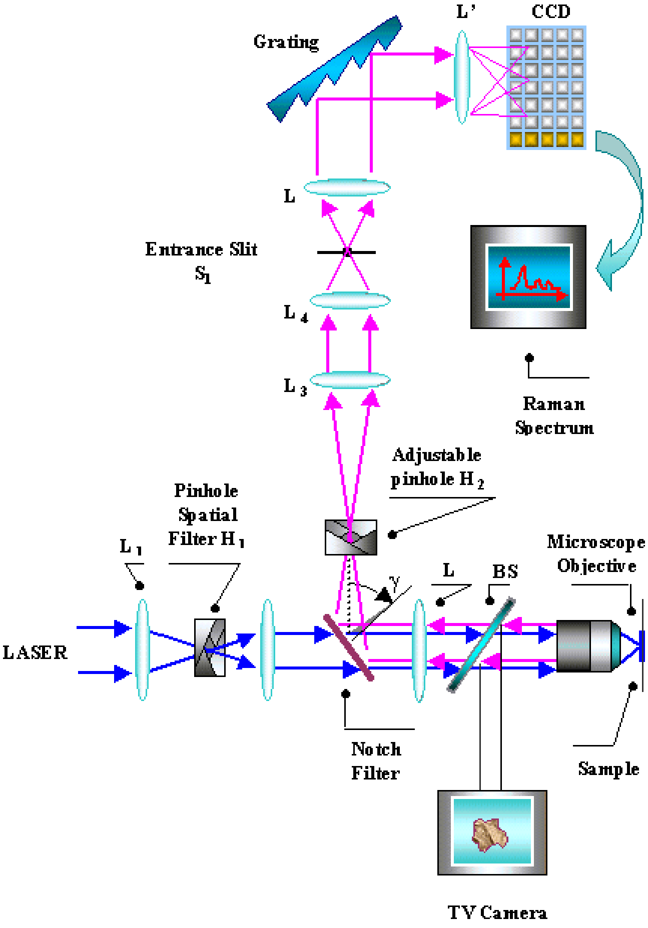

Figure 4.15: Scheme of LabRam spectrometer.

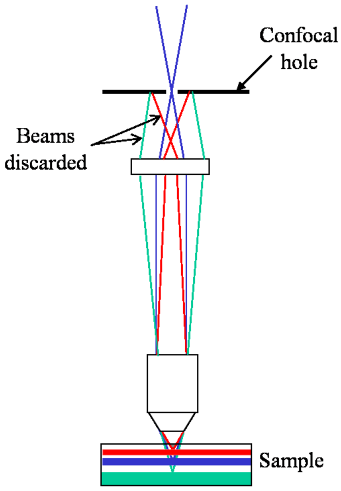

Figure 4.16: Scheme of confocal setup in Raman spectrometer.

This procedure was performed for each spectrum taken at different X positions along a line from the Fe-doped surface up to the bulk for all the samples under study. The four samples here considered, containing the same amount of Fe with the same distribution: two of them are diffused in dry/wet oxygen, the other two were also post-treated in reducing atmosphere (they are part of the six samples considered in section 4.4.2).

In figure 4.17 are reported, as a function of depth X, the frequency position and the FWHM of the $A_1(TO_1)$, $A_1(TO_2)$, and $A_1(TO_4)$] modes.

For all the samples the frequency of the $A_1(TO_1)$ and $A_1(TO_4)$ phonons (figure 4.17 a and e) shows on the doped face an increase from the substrate to the surface, which is absent on the undoped face. Its trend is in remarkable agreement with the concentration profiles of Fe given by SIMS data, which were shown in figure 3.9d. These facts ensure that the increase in frequency of these phonons is related to Fe incorporation. Two parts of the profiles can be therefore distinguished: the first part from 0 µm to 10 µm where the dopant is present, and the second part from 10 µm to 20 µm where the dopant is absent. Any difference between profiles of different samples in the undoped part should be therefore ascribed to the effect of the annealing atmosphere, and not to Fe doping. In the doped part, the frequency shifts of $A_1(TO_1)$ and $A_1(TO_4)$ ascribed to Fe incorporation are not so large (0.5 to 0.7 cm^{-1}) but significantly beyond experimental error. In contrast, the $A_1(TO_2)$ frequency profile (figure 4.17 c) does not evidence any significant variation of its frequency as a function of depth.

A remarkable feature in the undoped part of the profiles is that whereas the frequency of the phonon $A_1(TO_2)$ is nearly unaffected to any treatment, the frequency of $A_1(TO_1)$ is slightly larger in reduced samples than in the oxidised ones. Frequency and damping or $A_1(TO_4)$ are significant larger for both reduced sample with respect to oxidised ones. Moreover, the sample treated in dry oxygen has a larger damping of $A_1(TO_2)$ and $A_1(TO_1)$ phonons with respect to the other three samples, in particular the trend of $A_1(TO_1)$ damping is different: for the sample treated in dry oxygen it increases in the doped part, whereas it decreases for the other three samples.

4.5.3 Interpretation

The change exhibited by both the frequency and damping of $A_1(TO_1)$ (which, as stated above, is related to the motion of Nb sublattice) on approaching the surface in the doped part, together with the constancy of the $A_1(TO_1)$ (which is related to the Li sublattice) characteristics could prove in a first view that the Fe incorporation should concern the B sites only while the A sites should be unaffected. Instead this description has to be discarded, first of all because PIXE analysis proved that A sites are occupied by Fe, and secondly because incorporation of Fe on B sites should induce an increase of disorder on B sites and thus of the $A_1(TO_1)$ damping, which is opposite to the experimental observations. Retaining the fact that Fe ions go on A sites, the hypothesis that Fe ions push out Nb ions from antisites back to their natural site (B site) is in accordance with experimental observation: indeed the phonon frequency increase and damping decrease of the $A_1(TO_1)$ phonon can be explained by the replacement of Nb vacancies by Nb ions, which leads to a strengthening of the chemical bonds and a structural re-ordering in Nb sublattice, as observed when going from congruent to stoichiometric LN. The nearly constant values of frequency and damping of $A_1(TO_2)$ can be explained by the fact that if Fe ions substitute for Nb ions approximately in the same amounts, no large change in the frequency or damping should be expected.

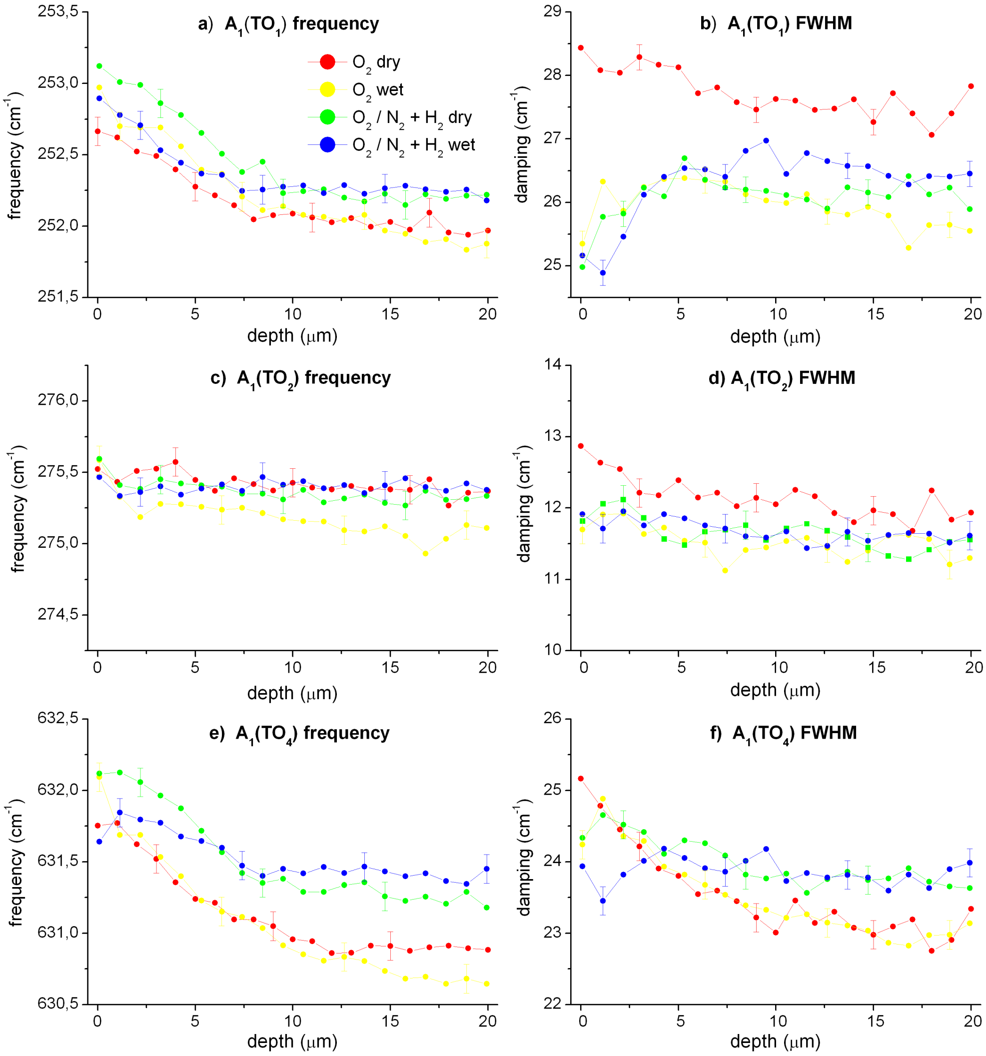

Figure 4.17: In-depth profiles of frequency and FWHM of Raman lines, corresponding to A_1TO_1, A_1TO_2, A_1TO_4 Raman modes, measured on four samples annealed under different atmospheres.

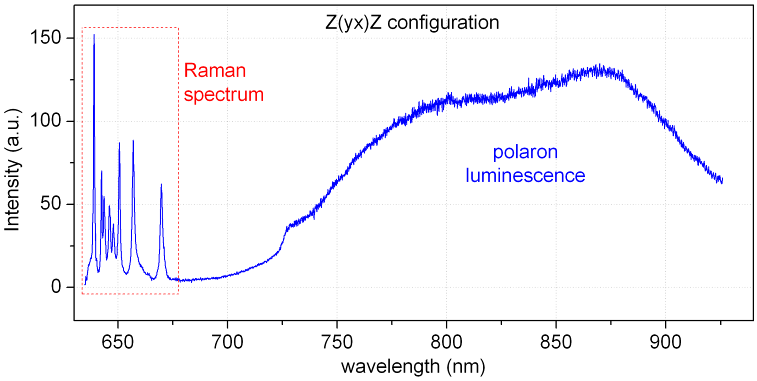

Figure 4.18: Spectrum acquired with Raman spectrometer in Z(yx)Z configuration: beside the Raman spectrum, a broad band, attributed to polaron luminescence, is visible.

Concerning the peculiar behaviour of $A_1(TO_1)$ damping, the larger values for sample treated in dry oxygen can be explained invoking out-diffusion of Li, which causes higher disorder. Wet atmosphere inhibits Li out-diffusion, hence in both wet treated samples the damping is smaller; in the dry post-treated sample, the absence of damping enlargement can be ascribed to the fact that the 4 hours long annealing at 500 °C heals the disorder formerly created by Li out-diffusion.

The $A_1(TO_4)$ frequency and damping in the undoped part show no dependence on water vapour presence, therefore their lower value for reduced samples has to be ascribed to the reducing gas: maybe the reduction creates some oxygen vacancies that affect the vibration of oxygen octahedra.

4.6 Polaron luminescence

When a Raman spectrum is acquired with exciting wavelength 633 nm, an intense and very broad band starting at 730 nm and extending beyond 950 nm is detected. This band is always present in congruent LN, even if nominally pure, but vanishes in stoichiometric LN; its intensity is enhanced after chemical reduction and is fairly proportional to the incident intensity up to 2 GWm^2. This band has a huge intensity in comparison to the Raman lines. This band is attributed to the radiative excitation of electrons trapped by niobium ions, namely polarons Nb^{4+}. In the dark at room temperature, electrons are mostly trapped by pairs, making a bond between a niobium antisite and a niobium at neighbor normal site, hence forming the bipolaron. Under illumination, the bipolaron is dissociated into two single polarons by a first photon, then a second photon causes ionisation of one of the created polarons. The bipolaron absorption band is a broad peak centered at 500 nm, whereas the polaron absorption band ranges from 580 nm to 850 nm. Owing to the overlapping of the absorption bands both processes are still fairly efficient at 633 nm, the wavelength used for our measurements. The whole luminescence band in the range 700 nm - 950 nm can be resolved into two main peaks: a gaussian peak centered at 790 nm and a wide lorentzian peak centered at 880 nm, both related to polaron luminescence [35].

For the present work, the six samples already described before, plus one additional sample with much lower concentration and longer diffusion profile (0.1 mol%, 10 μm),

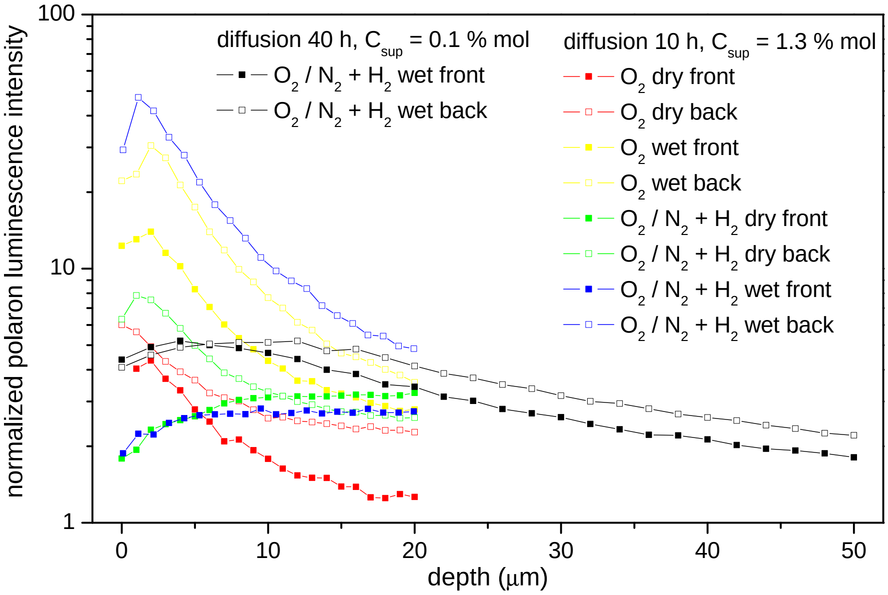

Figure 4.19: In-depth profiles of normalised polaron luminescence intensity of several samples, both on the doped side and on the undoped side.

were investigated by profiling the lateral face in Z(yx)Z configuration, both on the doped side and on the undoped side. For each spectrum, the PL intensity integrated over the whole PL band was then normalised to the intensity of a reference Raman line. The normalised intensity was then plotted as a function of depth: the results are reported in figure 4.19. Since many of the samples here considered are oxidised, their absorption at 633 nm is negligible, nevertheless PL is very intense, indicating that the process leading to PL is very sensitive and efficient. The PL emission coming from a given point of the sample can be considered as proportional to the concentration of photo-polarons at this point, that is, the concentration of polarons created by the dissociation of bipolarons under the incident light.

The most striking feature is that all the samples show an increasing trend of PL going from depth to surface, except reduced samples, which show opposite trend. This feature can be explained by recalling that the D absorption band, present only in reduced Fe:LN, covers also the exciting wavelength of Raman experiment (633 nm), therefore the incident intensity is partially absorbed by Fe^{2+} and induces less PL. This interpretation is supported by the fact that the decrease of PL at the surface of reduced samples (red and blue full points in figure 4.19) follows the same profile of Fe concentration. The increasing trend of PL intensity detected for all the other samples can be understood recalling reaction 1.1 and other reactions discussed in section 6.1.6. Both oxygen and Li out-diffusion induce a rearrangement of the structure, which involve the creation of further antisites Nb_{Li}: the increased number of Nb antisites leads to an enhanced PL intensity. This interpretation is supported by the fact that the sample annealed for much longer time shows a profile deeper and lower than its analogous shortly annealed sample: the longer annealing allowed a better rearrangement of the structure, involving deeper regions of the sample. This effect was already observed on Ti:LN after long high temperature annealing required for creating Ti diffused waveguides [35]. Considering one sample at a time, the fact that the PL intensity is always lower on the undoped face with respect to the doped face can be ascribed to lower abundance of Nb antisites on the doped face: as inferred in discussion of Raman results, Fe ions substitute for Li and oust some Nb from antisite to regular site, therefore their number is expected to decrease and PL intensity decreases as well. In general, sample treated in wet atmosphere show a larger PL intensity: this fact hints a not yet clear role of hydrogen in the mechanism leading to PL.

4.7 Electron spin resonance

When the molecules of a solid exhibit paramagnetism as a result of unpaired electron spins, transitions can be induced between spin states by applying a magnetic field and then supplying electromagnetic energy, usually in the microwave range of frequencies. The resulting absorption spectra are described as electron spin resonance (ESR) or electron paramagnetic resonance (EPR). The interaction of an external magnetic field with an electron spin depends upon the magnetic moment associated with the spin. The application of the magnetic field then provides a magnetic potential energy which splits the spin states by an amount proportional to the magnetic field (Zeeman effect), and then radio frequency radiation of the appropriate frequency can cause a transition from one spin state to the other.

ESR measurements were performed by L. Bogomolova at Moscow State University, using a modified spectrometer working with electromagnetic frequency 9.45 MHz, at 77 K or at room temperature. The samples investigated have surface concentration 0.5 mol%, and diffusion depth of about 10 µm. Here, only the main results are presented, without going into details. The single broad absorption line associated with Fe ions vaies depending on the orientation of the crystal with respect to applied magnetic field. This angular anisotropy indicates a long range magnetic order in the plane of sample surface. The temperature dependence of this signal does not follow a Boltzmann distribution, expected in the case of paramagnetic systems: this fact prevents the estimation of Fe^{3+} concentration. By reducing the temperature, the ESR line broadens and shifts towards lower field: this indicates the formation of superparamagnetic particles. In summary, the results can be interpreted by assuming that a part of Fe ions forms inclusions with long-range magnetic ordering, the remaining part are isolated Fe^{3+} ions.

4.8 Hydrogen incorporation

IR spectroscopy was used to characterise the OH^- incorporation during thermal treatments. As already mentioned in section 1.4.1, quantification of OH^- is difficult due to scattering of cross section data from different authors, therefore discussion of the results will be only qualitative. Measurements were performed in transmission using a Jasco FTIR spectrometer, in the range $3000 \div 4000$ cm^{-1} with step 0.25 cm^{-1}. Fourier transform was done on 64 acquisitions for each sample. The sample investigated are the same six samples investigated by Raman and HRXRD. The most representative results are gathered in figure 4.20. An undoped, untreated $LiNbO_3$ sample was measured for comparison: the native content of OH groups in the virgin crystal results in a relatively intense band. For samples diffused in dry oxygen and dry argon, the intensity of the band has strongly decreased, that means that the crystal lost its OH groups, due to the fact that these atmospheres are devoid of water and the OH groups in the crystal tend to form H_2O molecules which evaporate. When the atmosphere is

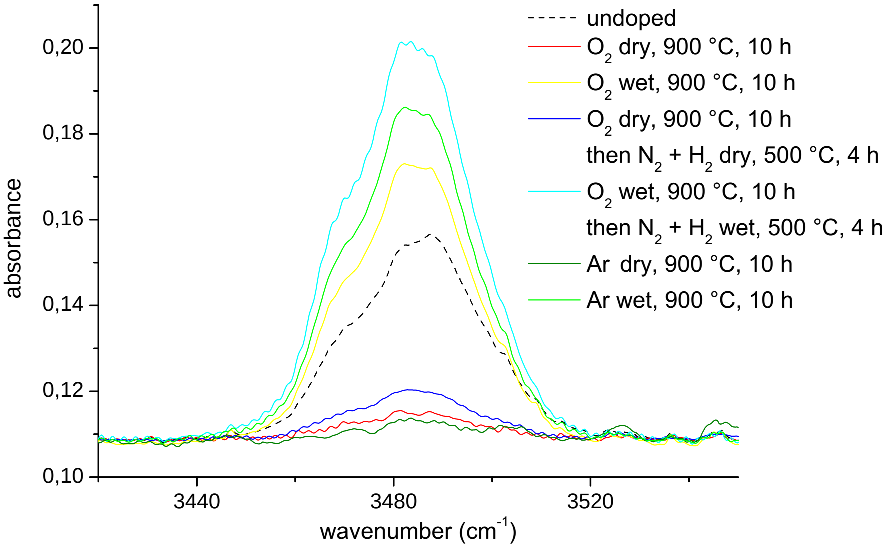

Figure 4.20: Infrared spectra of six samples annealed under different atmospheres and one untreated sample for comparison. The band due to OH stretching changes its intensity according to the H_2O and H_2 content of the atmosphere.

wet, it happens the opposite, H_2O molecules dissociate and enter the crystal, hence the band has greater intensity with respect to virgin sample. It is interesting to note that after post treatment in wet $N_2 + H_2$ the band is further increased, indicating that the OH content is further increased during the 4 hours of reducing treatment at 500 °C. By comparing samples diffused in dry oxygen before and after reducing treatment, it emerges that the band has become more intense, due to the fact that also H_2 molecules dissociate and form OH groups in the crystal. However, the amount of OH groups introduced by dry post treatment is much lower than the amount present in the virgin crystal, or the amount introduced by wet treatments.

Chapter 5

Laterally confined iron doping

The work presented so far concerns preparation and characterization of a virtually infinite surface of $LiNbO_3$ doped with Fe by diffusion. In the final device however only a small region of the monocrystal is doped. Laterally confined doping requires different preparation and characterisation methods and gives rise to new problems to solve. Here few demonstrative samples were prepared with a doped region with size 2 mm × 2 mm, intentionally larger than supposed, in order to simplify preparation, SIMS and optical absorption measurements. However the larger size has no influence on the analysis discussed on this chapter.

The main points discussed in this chapter are lateral diffusion of Fe, which broadens the boundary between doped and undoped region, and the effect of the reducing treatment on doped and undoped regions.

5.1 Preparation

The aim is to deposit on the substrate a square thin film of iron by masking the substrate before magnetron sputtering deposition. Masking presents several problems. The mask should have well defined edges, should be precisely aligned with crystallographic directions and should be removed without damaging the deposited film. The most indicated method to obtain such result is a photolithographic method: a photoresist is deposited on the substrate, then a mask with the desired shape is put on it, then illuminated with UV light to allow polimerization only in the illuminated region (positive photoresist), then the non polimerized part is removed by a chemical etching. After magnetron sputtering deposition, Fe is deposited on the desired square region of the substrate and on the remaining photoresist. At this point, the photoresist and the film deposited on it must be removed before diffusion. From the technological point of view, this is the most critical step. Before attempting to solve the above mentioned technological problems, a preliminary investigation of the system was done by using a much simpler masking method, i.e. laying a metallic hard mask in contact with the substrate. The mask is made of stainless steel, 100 μm thick; holes were produced by electroerosion; holes have two sizes: 1 mm × 1 mm and 2 mm × 2 mm. Mechanical alignment and contact are ensured by a custom made cell, which traps the mask and the substrate and keeps them fixed on the sample holder. The edges of the mask are not flat and the alignment is not precise, however this rough method does not damage the Fe film during removal and allows to obtain quickly the desired result.

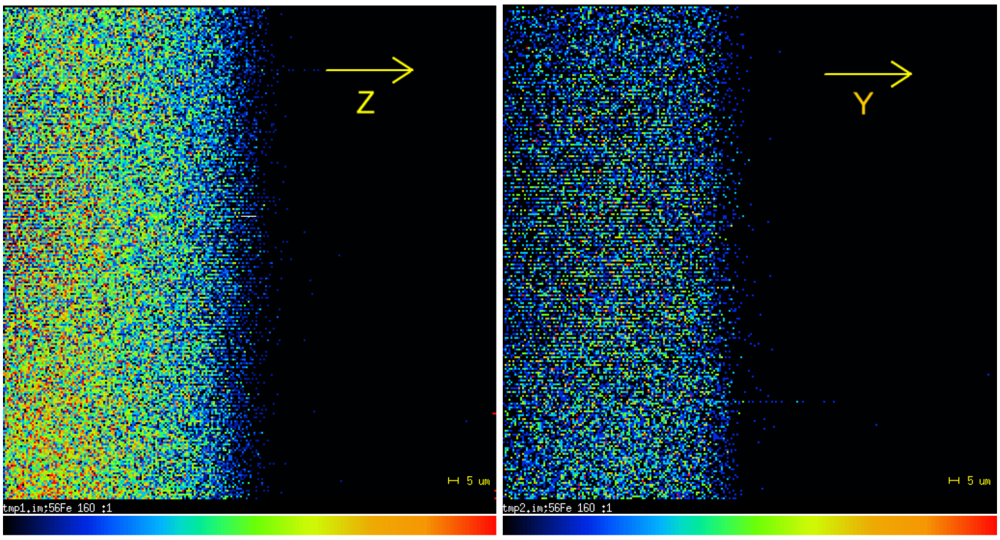

Figure 5.1: SIMS ion images of FeO^- ion on the boundary between doped region and undoped region, perpendicular to Z axis (left) and to Y axis (right).

5.2 Lateral diffusion

Once the deposition of the metallic Fe layer has been laterally confined, the usual thermal treatment under oxygen atmosphere must be performed to achieve diffusion. Obviously Fe ions diffuse not only in depth, along X axis, but also laterally along Z and Y axis. This fact may constitute a problem in the final device, hence it is important to investigate it. SIMS scanning ion imaging is a suitable tool for characterising lateral diffusion. The experimental details about how scanning ion images were obtained are given in appendix A. The investigated regions are 250 µm × 250 µm squares, straddling the boundary between doped and undoped region. The lateral resolution of this measurements, evaluated experimentally by measuring test samples in the same conditions, is better than 3 µm. The sample investigated was treated at 1000 °C for 8 h. Since the two crystallographic direction lying in the diffusion plane are anisotropic, ion images were performed both on one edge perpendicular to Z axis and one edge perpendicular to Y axis. After checking with an in-depth profile that the concentration of Fe is constant over the first 2.5 µm, the images are obtained by eroding 2.5 µm in depth, while acquiring one image plane every 7 nm of substrate. The images shown in figure 5.1, obtained after accumulation of many image planes, show clearly the broadened boundary. A line, crossing perpendicularly the boundary, was chosen, and the intensity at each point of such line, with steps of about 1 µm, was plotted as a function on the position, to obtain a lateral concentration profile. The signal results noisy due to scarcity of counts, however the trend is clear. According to the phenomenological treatment of diffusion, the doped region behaves in this case as an infinite source of diffusing species, hence at a first approximation the concentration profile should follow the complementary error function(equation 3.4). The linescan in figure 5.2 was therefore fitted with an erfc function. The resulting width parameters resulted $w_Z = (23.3 \pm 0.4)$ µmfor diffusion along Z axis, and $w_Y = (15.7 \pm 0.5)$ µmfor diffusion along Y axis. From these values the lateral diffusion coefficients can be

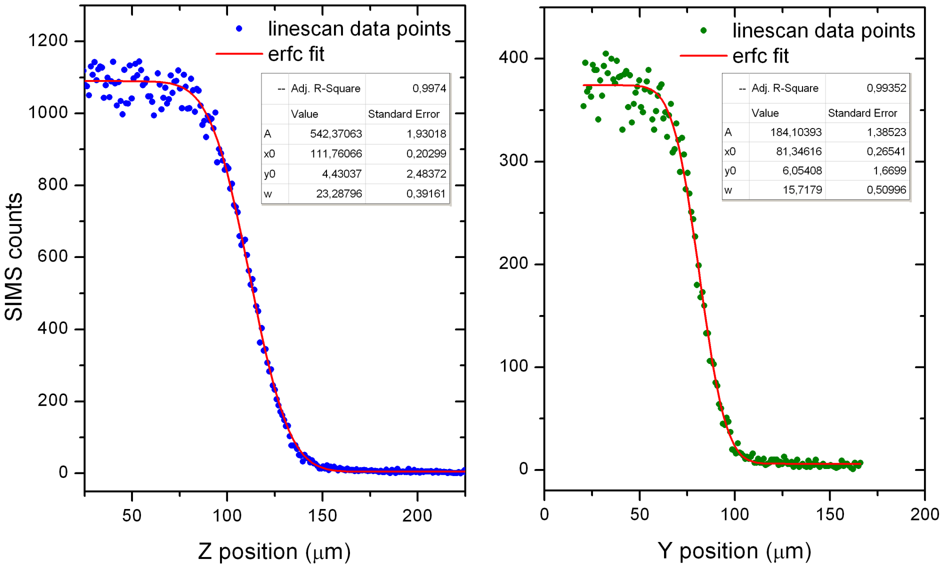

Figure 5.2: Lateral linescans of SIMS counts taken from scanning ion images, across the boundary perpendicular to Z axis (left) and Y axis (right), fitted with complementary error function.

calculated:

$$D_{\mathrm{Zl}} = (47 \pm 2) \times 10^{-4} \mathrm{\mu m^2 s^{-1}} \tag{5.1}$$

$$D_{\mathrm{Yl}} = (21 \pm 2) \times 10^{-4} \mathrm{\mu m^2 s^{-1}} \tag{5.2}$$

These values can be compared with the in-depth diffusion coefficient along X axis at the same temperature, $D_{\mathrm{Xd}} = (5.1 \pm 0.2)10^{-4}$ $\mathrm{\mu m^2 s^{-1}}$. D_{Yl} is four times larger than D_{Xd}: since according to symmetry diffusivity along X should be equal to diffusivity along Y, the difference is justified by the fact that the in-depth diffusion condition differs from the lateral one, which occurs near the surface. The difference can be ascribed to the fact that annealing cause a superficial damage, and diffusion occurs easily through defects. The same consideration hold for D_{Zl}, which is almost ten times larger than D_{Xd}. Large differences, even more than one order of magnitude, between in-depth diffusivity and surface diffusivity were already reported in many experiments [36].

From the phenomenological point of view, the difference between D_{Zl} and D_{Yl} is justified by crystal anisotropy. From the microscopical point of view, as described in section 3.1.2, the migration path of an impurity is similar along X, Y and Z, because the impurity must pass through the same oxygen triangles, thus the activation energy is likely the same, but the migration rate can be in principle different, since an impurity has to pass a different number of oxygen triangles for travelling the same distance along X or along Z. Anisotropy may also arise if the impurity migration is affected by the internal field due to ferroelectricity, directed along the Z axis. Anisotropic diffusivities were already found, for instance, for Ti and Er [24]: in both cases D_Z resulted larger than D_{Y}, however the difference is small enough that several workers have labelled the diffusion as isotropic. On the contrary, in the present case the difference is not so small, D_{Zl} is more than two times D_{Yl}: however, before making a strict comparison with literature, the reliability of these preliminary results must be verified on a larger

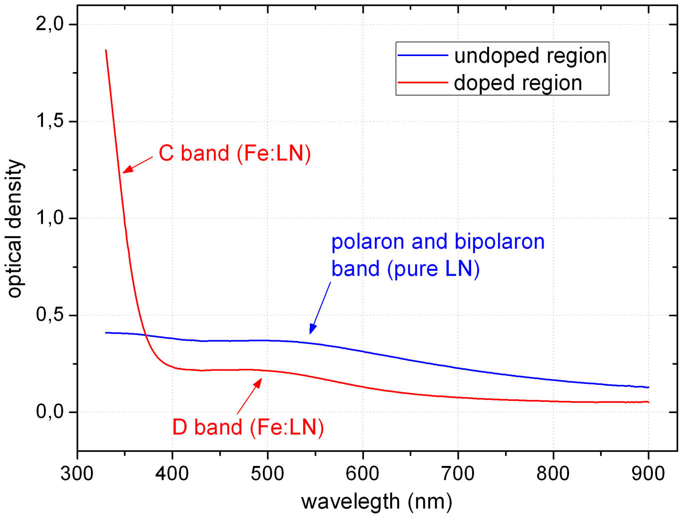

Figure 5.3: Optical absorption spectra inside and outside the doped region of a sample doped only on one half of the surface.

number of samples, and the accuracy of SIMS ion images must be improved.

5.3 Optical absorption

A sample was prepared in the following way: Fe was deposited on one half of the surface, the other half remaining undoped. The sample was then treated at 1050 °C for 10 h to promote Fe diffusion, then reduced at 500 °C for 2 h. To the naked eye, the sample is perfectly transparent, the doped region has the usual red colour, while the undoped region has a dark grey colour; moreover, an unexpected uncoloured stripe appears corresponding to the position of the boundary between doped and undoped region. Optical absorption measurements were performed in different positions of the sample inside and outside the doped region. The lateral width of the beam in the spectrophotometer is about 1 mm, therefore each spectrum was acquired moving the sample with steps of 1 mm, spanning a distance equal to 11 mm across the boudary between doped and undoped region, along y crystallographic direction. In figure 5.3 optical absorption spectra in the doped region and in the undoped region, far from the boundary, are shown. The doped region has the usual absorption bands due to Fe, and no other contributions are present. On the other hand, the spectrum in the undoped region shows a higher absorbance with respect to the doped region, in all the range of visible wavelengths. This absorption is due to reduction of intrinsic LN, i.e. polarons and bipolarons. From the standpoint of the final device, absorption in the undoped part is undesirable because it limits the intensity of light propagating in the waveguides of the device. In order to characterize how the absorption of the sample changes going from one region to the other, it is useful to plot the optical density (OD) values as a function of the position. Three wavelengths were chosen:

- a wavelength that provides a signature of Fe presence, i.e. a wavelength covered by C band (355 nm);
- a wavelength that provides a signature of polaron presence, far from iron's bands

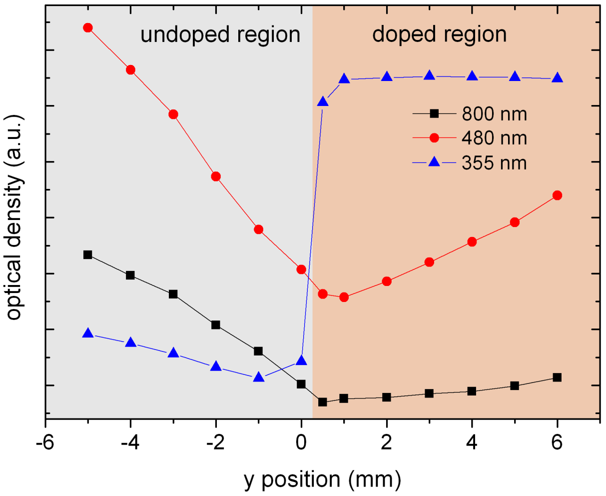

Figure 5.4: Optical density values at three selected wavelengths plotted as a function of position along y axis.

C and D (800 nm);

- a wavelength in the blue/green range, at which the final device should operate, for instance the wavelength of maximum absorbance of Fe (480 nm).

The optical density at the first wavelength marks the boundary between doped and undoped region; the second indicates how much the intrinsic LN gets reduced as a function of the position; the third indicates how much the material absorbs the light that will propagate in the waveguides. The values of OD at the three selected wavelengths are plotted as a function of position in figure 5.4.

In the undoped region a decreasing trend of OD at all the three wavelengths is observed. Since polarons and bipolarons absorb at all the three wavelengths considered, the three trends are similar, in fact the ratio between them is constant going from position -5 to position -1. The decreasing trend approaching the boundary indicates that the reduction degree of intrinsic LN is sensitive to the presence of the boundary. Going from position +1 to position +6, OD at 355 nm is constant, indicating that the total Fe concentration is constant, while the other two have an increasing trend. The OD at 480 nm, which represents in general the reduction of the material, has a minimum in correspondence to the boundary. Since in the doped region OD at 480 nm contains contributions both from polarons and from Fe^{2+}, in order to evaluate correctly its trend it must be compared to the trend of OD at 800 nm, which instead is due to polarons only.

The ratio between OD at 480 nm and OD at 800 nm is a proper quantity to evaluate the Fe^{2+} concentration trend. In fact this ratio is constant in the undoped region, where both OD are due to polarons only, and start to increase at the boundary indicating an increasing contribution of Fe^{2+} absorption going from position 0 to position +4. This means that the Fe^{2+} concentration is not constant, instead it increases going far from the boundary over several mm. In other words, there is a gradient of reduction degree which spans a distance much greater than the gradient of Fe concentration.

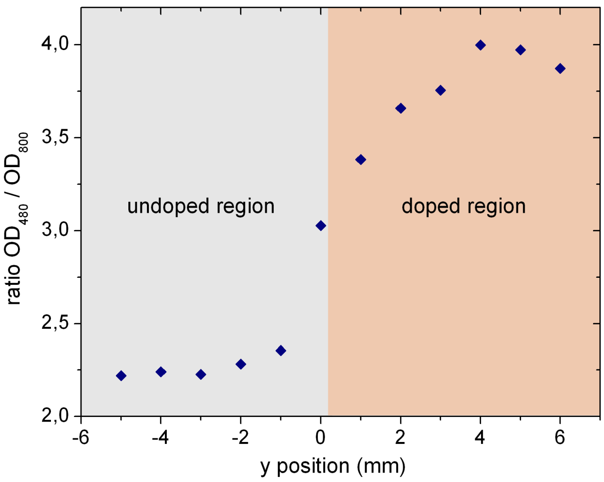

Figure 5.5: Ratio between optical density in the Fe^{2+} spectral region and optical density in the polaron region, indicating the reduction degree of the material, as a function of position from the boundary separating doped and undoped region.

The observation of these phenomena poses several questions. First of all, why reduction is inhibited at the boundary. To the naked eye, the minimum in the trend of the red line in the graph 5.4 hints a kind of depletion of charge carriers at the boundary. A gradient of chemical potential across the boundary can be hypothesised, which pushes the electrons far from the boundary; by now however there are not sufficient elements to justify this hypothesis. Second, the gradient of the reduction degree constitutes a problem for the final device, which should have a perfectly homogeneous reduction degree in the doped region, in order to have homogeneous photorefractive efficiency. Since the doped region will be approximately 250 µm × 250 µm large, the characterisation of the reduction degree cannot be done by conventional spectrophotometry, but requires a probe with micrometric size.

Chapter 6

Conclusions and perspectives

This chapter contains a summary and a critical cross-linked discussion of the results presented in previous chapter, and final considerations about the feasibility of the device, as well as ideas and perspectives for the future work.

6.1 Advances in knowledge of the Fe - diffused LN system

6.1.1 Lattice position of Fe

Even though the lithium vacancy model is the most accounted one, the existence of Nb vacancies cannot be completely ruled out when dealing with high temperature diffusion [24]. The total cation vacancy concentration is 3.9 mol% and the [Li]/[Nb] ratio is 0.94 for all models. When the material is doped with Fe, a certain amount of Fe_2O_3 is added: in the case of Czochralski growth from doped melt, Fe_2O_3 is added directly to $LiNbO_3$ in the crucible; in the case of thermal diffusion, metallic Fe gets oxidised then the two oxygen sublattices merge and, after interdiffusion of cations, form a single structure. If y molecules of Fe_2O_3 are added every 1 molecule of $LiNbO_3$, $3y$ atoms of O and $2y$ cation sites must be added to the unit formula: since the number of O atoms increases, the ratios [Li]/[O] and [Nb]/[O] have changed while the ratio [Li]/[Nb] is unaltered. If Fe occupies the Li site, there are two possible formulae: if the Nb_{Li} population remains unchanged

$$\{[\mathrm{Li}]_{1-5x}[\mathrm{Nb_{Li}}]_x[\mathrm{Fe}]_{2y}[\mathrm{V_{Li}}]_{4x-y}\}\{[\mathrm{Nb_{Nb}}][\mathrm{V_{Nb}}]_y\}\mathrm{O}_{3+3y} \tag{6.1}$$

where y must be less than $4x$, namely the atomic percentage of Fe must be less than 8 mol%. Fe accommodation decreases the vacancy concentration in the Li site, while some vacancies are created in the Nb site. On the other hand, if we assume that these new Nb vacancies are filled by Nb atoms located originally in the Li site, the formula will be

$$\{[\mathrm{Li}]_{1-5x}[\mathrm{Nb_{Li}}]_{x-y}[\mathrm{Fe}]_{2y}[\mathrm{V_{Li}}]_{4x}\}\{[\mathrm{Nb_{Nb}}]_{1+y}\}\mathrm{O}_{3+3y} \tag{6.2}$$

where of course y cannot exceed x, i.e. this formula is possible only if Fe is less than 2 mol%. It can be concluded that if Fe substitutes only for Li, and if $y > 0.01$, there *must* be some Nb_{Li} moving to regular Nb site, and the antisite concentration diminishes. If the latter movement is ruled out, Fe must necessarily occupy partially

Nb site, according to the formula:

$$\{[\mathrm{Li}]_{1-5x}[\mathrm{Nb_{Li}}]_x[\mathrm{Fe}]_{2y-z}[\mathrm{V_{Li}}]_{4x+y+z}\}\{[\mathrm{Nb_{Nb}}][\mathrm{Fe}]_z\}\mathrm{O}_{3+3y} \tag{6.3}$$

If the coexistence of Nb and Li vacancies is considered, the most general formula is obtained:

$$\{[\mathrm{Li}]_{1-5x}[\mathrm{Nb_{Li}}]_{x+w}[\mathrm{Fe}]_{2y-z}[\mathrm{V_{Li}}]_{4x-w+y+z}\}\{[\mathrm{Nb_{Nb}}]_{1-w}[\mathrm{Fe}]_z[\mathrm{V_{Nb}}]_{w+y-z}\}\mathrm{O}_{3+3y} \tag{6.4}$$

where the only constrains are $z < 2y$, $2y < 4x$ (i.e. Fe must be less than 4 mol%) and $y < w - z < 4x + y$. To summarise, the existence threshold, in terms of Fe atomic percentage, is 2 mol% for configuration 6.2, 4 mol% for configuration 6.4, 8 mol% for configuration 6.1, and finally there is no threshold for configuration 6.3.

All the configuration described above provide charge compensation. However not only the overall charge compensation of the crystal must be satisfied, but also *local* charge compensation should be maximised. From this point of view, the defect configuration which minimises long range coulomb field due to impurity defect is the one in which two Fe atoms lie on two adjacent sites and one substitutes for Li, the other for Nb. Since $\mathrm{Fe_{Li}}$ has net charge +2 and $\mathrm{Fe_{Nb}}$ has net charge -2, charge balance is accomplished within only one primitive cell. This is possible in two of the defect structures proposed, 6.3 and 6.4 putting $z = y$. This kind of configuration implies a clustering of Fe atoms in couples. However, preliminary PIXE-channeling investigation showed that the majority of Fe atoms are located on Li site, therefore the latter configuration cannot be valid for all the dopant atoms, but also a small part of them. One may think of even more complicated configurations involving clustering of impurities and their charge-compensating defects, forming some kind of domains or inclusions whose existence may be not detectable by XRD due to their small size. Such configurations could explain the results obtained by EPR, which indicate the presence of ferromagnetic inclusions. In the future work will be devoted to investigate carefully the system by means of PIXE-channeling and EPR, and correlate the results: in particular it will be interesting to check if there are differences between samples with different concentrations, above and below the above described thresholds, and if the results will allow to discard one or more configurations.

6.1.2 Relation between lattice deformation and reduction degree

The results presented in section 4.4.1 show that $\mathrm{Fe^{3+}}$ induces a lattice compression which decreases when iron is reduced to $\mathrm{Fe^{2+}}$, moreover the reversibility of this phenomenon was proven, i.e. after re-oxidation of the sample the $\mathrm{Fe^{2+}}$ amount diminishes and the lattice deformation increases. This fact hints a direct relation between lattice deformation and reduction degree. Since the concentration of defect impurities is small (less than 2 mol%), it is reasonable to assume that the deformation is given simply by a linear superposition of the contributions from all the defects, according to a simple relation:

$$\xi = k_1[\mathrm{Fe^{3+}}] + k_2[\mathrm{Fe^{2+}}]$$

Assuming that there are no other sources of deformation, k_1 and k_2 can be estimated from experimental data. Three samples were considered for this study with different fluences, different thermal treatments and therefore different profiles and surface concentration: their characteristics are listed in table 6.1. Each sample was cut into two

fluence 10^{15} at/cm^2	thermal treatments	C_{sup} 10^{20} at/cm^3	α_{sup} 10^2 cm^{-1}	ξ 10^{-6}
108	8 h at 1000 °C in O_2	1.75	0.06 ± 0.1	-162 ± 2
	+ 1.5 h at 500 °C in Ar + H_2		1.7 ± 0.1	-125 ± 2
	+ 1.5 h at 500 °C in Ar + H_2		3.5 ± 0.1	-55 ± 4
	+ 2 h at 500 °C in O_2		2.4 ± 0.1	-98 ± 2
50	8 h at 900 °C in O_2	2.3	0.01 ± 0.4	-198 ± 2
	+ 0.5 h at 500 °C in Ar + H_2		4.7 ± 0.4	-108 ± 2
66	10 h at 900 °C in O_2	2.4	0.1 ± 0.3	-221 ± 2
	+ 1.5 h at 500 °C in Ar + H_2		3.6 ± 0.3	-160 ± 2
	+ 0.5 h at 500 °C in Ar + H_2		5.4 ± 0.3	-114 ± 2

Table 6.1: List of samples exploited for studying the relation between lattice deformation and reduction degree. Each entry reports the fluence, the thermal treatments, the surface concentration, the surface absorption coefficient, the relative lattice deformation.

or more subsamples which underwent subsequent reduction / oxidation treatment, thus obtaining different reduction degrees, measured by means of optical absorption. For the samples with 108 × 10^{15} at/cm^2, data have been already presented in figures 4.11 and 4.4.

As explained in section 4.4.1, the quantity extracted from XRD measurements is the maximum deformation, i.e. deformation at the surface. If a relation between deformation and concentrations is to be found, also the concentrations of Fe^{3+} and Fe^{2+} must be considered *at the surface.* Since the measured quantities, from which [Fe^{3+}] and [Fe^{2+}] are extracted, are the total Fe concentration and the optical density, it is convenient to relate the lattice deformation to these quantities:

$$\xi_{\text{sup}} = m_1 C_{\text{sup}} + m_2 \alpha_{\text{sup}}$$

where C_{sup} is the total concentration of Fe at the surface, and α_{sup} is the surface absorption coefficient at 532 nm. It can be easily seen that $m_1 = k_1$ and $m_2 = \frac{k_2 - k_1}{\sigma}$, where σ is the absorption cross section at 532 nm. These quantities can be easily derived from fluence and optical density, by using SIMS data. The integral of SIMS normalized Fe signal S_{tot} is proportional to the fluence, and the signal at the surface S_{sup} is proportional to C_{sup}, therefore

$$C_{\text{sup}}[\text{cm}^{-3}] = F[\text{cm}^{-2}] \cdot \frac{S_{\text{sup}}}{S_{\text{tot}}[\text{cm}]}$$

where F is the fluence. Similarly, assuming that Fe^{2+}/Fe^{3+} ratio is constant with depth,

$$\alpha_{\text{sup}}[\text{cm}^{-1}] = OD \cdot \frac{S_{\text{sup}}}{S_{\text{tot}}[\text{cm}]}$$

In this way data reported in table 6.1 were calculated. These values may be viewed as points in a three-dimensional space where the coordinates are ξ_{sup}, C_{sup} and α_{sup}: these points must be fitted with a plane to find the coefficients m_1 and m_2. To this aim, a simultaneous least square minimisation was carried out, using ξ_{sup} and C_{sup} as

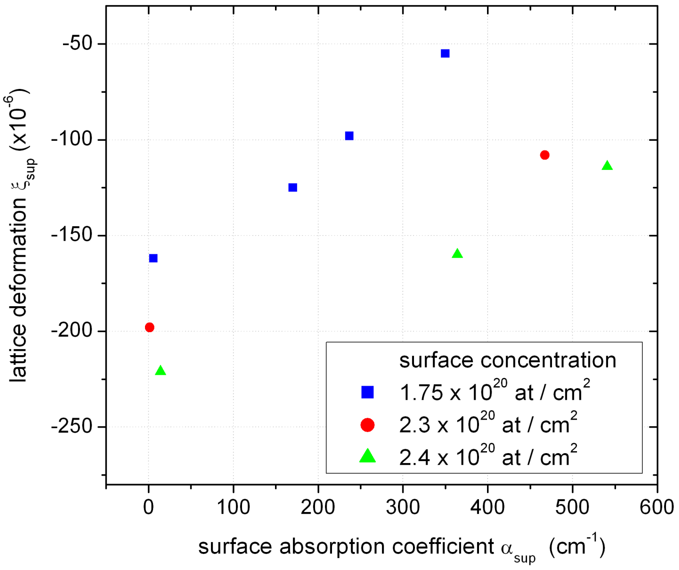

Figure 6.1: Lattice deformation vs surface absorption coefficient for the eight samples considered, with three different concentrations.

independent variables due to their smaller uncertainty. The resulting coefficients are

$$k_1 = (-1.3 \pm 0.2) \times 10^{-24} \tag{6.5}$$
$$k_2 = (-0.3 \pm 0.1) \times 10^{-24} \tag{6.6}$$

They indicate that the deformation produced by Fe^{2+} doping is several times lower than the deformation produced by Fe^{3+} doping, as observed at the beginning of this investigation.

In terms of a simple ionic crystal model, a lattice compression both with Fe^{3+} and with Fe^{2+} suggests that Fe substitutes for Li: the compression occurs because of the higher charge carried by the dopant with respect to Li$^+$, which attracts more strongly the surrounding oxygen anions. Reasonably the effect is higher with Fe^{3+} due to the higher charge difference and smaller ionic radius(65 pm, to be compared with 78 pm for Fe^{2+} and 76 pm for Li$^+$). Since LN is piezoelectric, another explanation of lattice compression can be envisaged: Fe impurity and the other defects that compensate its charge constitute a dipole, and set up an electric field, which produces via piezoelectric effect a deformation. Also in this framework the deformation is expected to be higher for Fe^{3+}.

6.1.3 Diffusivity of Fe in X-cut LiNbO$_3$

In chapter 3, a systematic study of in-depth Fe diffusion was accomplished, leading to the determination of the diffusion coefficient at four different temperatures

$$D_X^{900^\circ C} = (0.056 \pm 0.009)10^{-3}\mu m^2 s^{-1} \tag{6.7}$$
$$D_X^{950^\circ C} = (0.27 \pm 0.10)10^{-3}\mu m^2 s^{-1} \tag{6.8}$$
$$D_X^{1000^\circ C} = (0.51 \pm 0.07)10^{-3}\mu m^2 s^{-1} \tag{6.9}$$
$$D_X^{1050^\circ C} = (1.3 \pm 0.2)10^{-3}\mu m^2 s^{-1} \tag{6.10}$$

As already mentioned, only two determinations of D at only one temperature (1000 °C) were done in the past, thus this work enriches significantly the case study available in literature, extending to a wider range of temperatures, and allowing also an estimation of the activation energy $E_{\mathrm{att}} = (2.8 \pm 0.1)\mathrm{eV}$.

Also the lateral diffusivity along Y and Z axes were determined for $T = 1000$ °C:

$$D_{\mathrm{Zl}} = (47 \pm 2) \times 10^{-4} \mu\mathrm{m}^2\mathrm{s}^{-1} \tag{6.11}$$

$$D_{\mathrm{Yl}} = (21 \pm 2) \times 10^{-4} \mu\mathrm{m}^2\mathrm{s}^{-1} \tag{6.12}$$

It is worth to briefly recall that the difference between these two values is due to crystal anisotropy and that usually diffusivity along Z is slightly larger than along Y [24]. Since Y and X axis are isotropic, the difference between the in-depth diffusivity along X and the lateral diffusivity along Y is due to the fact that lateral diffusion occurs at the surface, which is modified by the thermal treatment, hence is faster than in depth diffusion, as already reported [36]. It is therefore reasonable that D_{Yl} results four times larger than D_{X} at the same temperature.

6.1.4 Hydrogen incorporation

When $\mathrm{LiNbO_3}$ is annealed at temperatures > 400 °C, dissociation of $\mathrm{H_2O}$ molecule on the surface of the crystal occurs:

$$\mathrm{H_2O} \longrightarrow \mathrm{H^+} + \mathrm{OH^-}$$

and $\mathrm{H^+}$ and $\mathrm{OH^-}$ are incorporated in the crystal. If the crystal contains OH groups, the opposite reaction occurs as well.

When the crystal is exposed to $\mathrm{H_2}$, dissociation of this molecule leads to incorporation of protons and electrons:

$$\mathrm{H_2} \longrightarrow 2\mathrm{H^+} + 2e^-$$

and the crystal enriches with OH groups as well as when it is exposed to water vapour. Moreover, electrons are incorporated and can be trapped at the lowest energy levels available, thus reducing the material.

6.1.5 Reduction of $\mathrm{LiNbO_3}$ and $\mathrm{Fe{:}LiNbO_3}$

The above described mechanism of hydrogen dissociation leads to reduction of the material according to the following reactions: if pure LN is considered

$$\mathrm{Nb^{5+}} + \mathrm{O^{2-}} + \frac{1}{2}\mathrm{H_2} \longleftrightarrow \mathrm{Nb^{4+}} + \mathrm{OH^-} \tag{6.13}$$

thus polarons and OH groups are created, without need to rearrange the structure. If Fe:LN is considered, beside the reduction of Nb also reduction of Fe can occur:

$$\mathrm{Fe^{3+}} + \mathrm{O^{2-}} + \frac{1}{2}\mathrm{H_2} \longleftrightarrow \mathrm{Fe^{2+}} + \mathrm{OH^-} \tag{6.14}$$

also in this case without need of rearrangement. Reduction of Nb and Fe are concomitant and concurrent. The same reactions are expected to occur with other reducing gases containing hydrogen atoms, as phosphine ($\mathrm{PH_3}$) or hydrazine ($\mathrm{N_2H_2}$).

Other kinds of reducing gas containing no hydrogen atoms, for example carbon monoxide (CO) act in a different way, they react with oxygen atoms creating oxygen vacancies and rearrangement of the crystal structure. Also inert gases affect the composition, because any atmosphere bare of oxygen causes oxygen out-diffusion from the crystal. The reduction reaction for pure LN, already presented in section 1.3.1, is

$$3\mathrm{O}_{\mathrm{O}}^{2-} + 2\mathrm{V}_{\mathrm{Li}} + \mathrm{Nb}_{\mathrm{Nb}}^{5+} \longleftrightarrow \frac{3}{2}\mathrm{O}_2 + \mathrm{Nb}_{\mathrm{Li}}^{4+} + 5\mathrm{e}^- \tag{6.15}$$

and involves the disappearance of a unit formula and rearrangement of the structure. In the case of Fe:LN, the latter reaction may be rewritten involving also reduction of Fe:

$$3\mathrm{O}_{\mathrm{O}}^{2-} + 2\mathrm{V}_{\mathrm{Li}} + \mathrm{Nb}_{\mathrm{Nb}}^{5+} + \mathrm{Fe}^{3+} \longleftrightarrow \frac{3}{2}\mathrm{O}_2 + \mathrm{Nb}_{\mathrm{Li}}^{4+} + \mathrm{Fe}^{2+} + 4\mathrm{e}^- \tag{6.16}$$

which means simply that Fe reduction occurs thanks to redistribution of the six electrons freed by oxygen out-diffusion. In other words, when using gases containing hydrogen, reduction occurs by *adding* something to the crystal (H atoms), while when using other gases reduction occurs by *removing* something from the crystal. It is therefore preferable the first way, because it introduces much less structural changes than the other.

Concerning the competition between reduction of Fe and reduction of Nb, experiments evidenced that the first prevails: for instance, the absorption spectrum of bulk doped Fe:LN after reduction shown in figure 1.11 indicates the absence of polarons. From the standpoint of band diagram, this means that the Fe level is located at lower energy with respect to bipolaron and polaron levels, hence the former is populated first. Thus electron are incorporated at the surface according to the mechanisms described above, then they move towards inner regions from one Fe ion to the next via hopping conduction, a mechanism that occur even at room temperature and is responsible for dark conductivity. The presence of both Fe^{2+} and Fe^{3+} ensures that the Fermi level is pinned at the Fe level.

In the case of diffused sample, the situation is more complicated. It should be expected that, as a result of reduction treatment, polaron and/or bipolaron are created in the undoped part of each Fe:$\mathrm{LiNbO_3}$ sample, giving rise to the relative absorption bands. But experimental data presented in table 4.3 showed that polarons and bipolarons are created only after short reducing treatments (30 - 90 min). After longer reducing treatments (3 hours), polaron and bipolaron bands disappear and the features in absorption spectra of samples are referable to Fe^{2+} solely. A possible explanation of this behaviour is the following. At the beginning of the reducing treatment, electrons introduced at the doped surface are trapped by Fe^{3+}, and the electrons introduced at the undoped surface are trapped by polaron and bipolaron states: as a result, the absorption spectrum displays contributions of both Fe^{2+} and polaron/bipolaron. As the treatment goes on, thermal excitation and transport of electrons take place: after redistribution of electrons, the Fe^{2+} population will grow at the expense of polaron/bipolaron population, in such way that the Fermi level is constant over the whole sample. Constant Fermi level implies also that the $\mathrm{Fe}^{2+}/\mathrm{Fe}^{3+}$ ratio is constant over the diffusion depth, i.e. that the in-depth distribution of Fe^{2+} is equal to that of Fe^{3+}. At last, even if 990 μm of thickness consist of pure LN and only 10 μm contain Fe, the reducing treatment affects only the doped layer of the sample. This implies that, at the temperatures adopted for reduction, the dynamics of electron transport are fast enough to let the electrons travel along the whole sample depth and be trapped at the most favourable site Fe^{3+} within few hours. This explanation is supported by the spectrophotometric characterisation of the boundary between doped and undoped region, presented in section 5.3, which showed a gradient of reduction

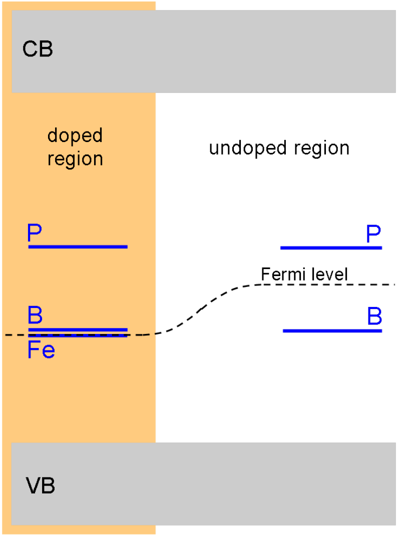

Figure 6.2: Energy level diagram of LN partially doped with Fe^{2+}/Fe^{3+}: in the doped part, Fermi level is pinned at Fe level, whereas in the undoped region lies between bipolaron level (B) and polaron level(P). At the boundary between doped and undoped regions, electrons experience a gradient of chemical potential that drives them towards the doped part.

degree and an electron depletion at the boundary. Far from the boundary, Fermi level is pinned between bipolaron and polaron level in the undoped region, whereas in the doped region it is pinned at Fe level, as schematised in figure 6.2. Hence electrons in the boundary experience a gradient of chemical potential which drives them towards the Fe doped regions, charge unbalance being compensated thanks to proton transport, until equilibrium is reached.

6.1.6 Effect of thermal treatments

The evaluation of the effect of different thermal treatments is done by comparing the results obtained by all the characterisation techniques (SIMS, spectrophotometry, FTIR, AFM, HRXRD, Raman, PL) on the set of six samples, presented in chapter 4 and summarised in table 6.2. All the treatments resulted in a complete diffusion of the film leaving a surface which appears smooth and undamaged to the naked eye. However, data presented in chapter 4 indicate that in spite of the same conditions of temperature and duration, different atmospheres have a different impact on the surface quality, on the structural characteristics and on the compositional parameters of the doped layer (i.e. Fe concentration, reduction degree and hydrogen content).
Concerning diffusion, as already mentioned in chapter 3, the reducing post-treatment does not promote further diffusion of Fe, as a consequence the diffusion profiles of the samples after diffusion in oxygen are equal to the profiles after reduction. Moreover, the presence of water vapour in the oxygen atmosphere does not affect the diffusion profiles, which resulted practically identical. Hence among the six samples, four have the same superficial concentration of Fe and the same diffusion profile, as shown in figure 6.3. Samples treated in argon instead have deeper profiles with respect to oxygen, and present a marked difference between dry and wet.

	oxygen	oxygen, N_2 + H_2	argon
dry	10 h at 900 °C	10 h at 900 °C then 4 h at 500 °C	10 h at 900 °C
wet	10 h at 900 °C	10 h at 900 °C then 4 h at 500 °C	10 h at 900 °C

Table 6.2: Summary of thermal treatments on the set of six samples investigated for the study of the effect of the atmosphere.

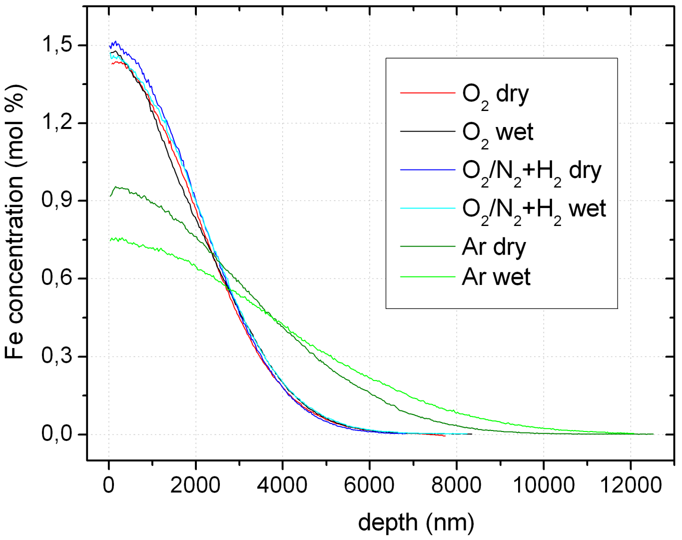

Figure 6.3: SIMS depth profiles of Fe of six samples diffused under different atmospheres.

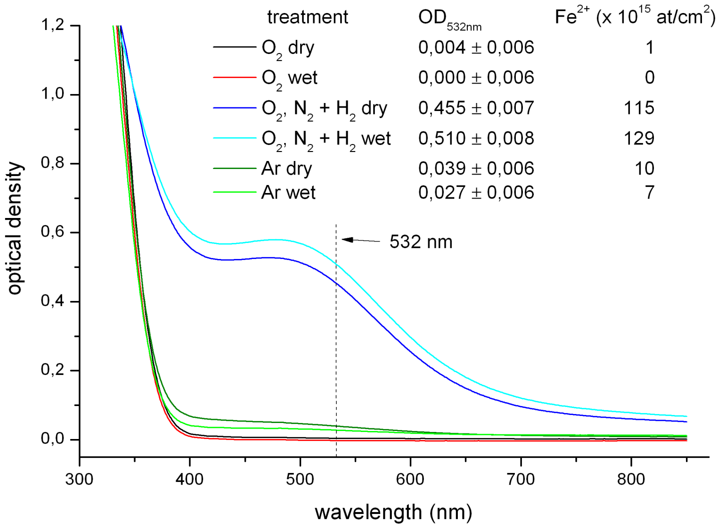

treatment	OD_{532nm}	Fe^{2+} (x 10^{15} at/cm^2)
O_2 dry	0,004 ± 0,006	1
O_2 wet	0,000 ± 0,006	0
O_2, N_2 + H_2 dry	0,455 ± 0,007	115
O_2, N_2 + H_2 wet	0,510 ± 0,008	129
Ar dry	0,039 ± 0,006	10
Ar wet	0,027 ± 0,006	7

Figure 6.4: Optical density spectra of six samples treated under different atmospheres.

The absorption spectra of the six samples are reported in figure 6.4: for each sample, the amount of Fe^{2+}, calculated using cross section 4.1, is also reported. Among the treatments here presented, the only ones which determined a significant reduction of Fe are the two post - treatments in $N_2 + H_2$, whereas Ar gives a small amount of Fe^{2+}. In the case of Ar, reduction is due to oxygen out-diffusion, accompanied by rearrangement of the defect structure. The higher defectivity, confirmed by the presence of the diffuse scattering on the reciprocal space maps, is responsible for the higher diffusivity of Fe in Ar treated samples indicated by SIMS depth profiles: indeed the more vacancies and defects are present, the easier will diffusion occur.

In the case of post - treatments in $N_2 + H_2$, reduction follows the dissociation of H_2, according to the mechanism explained in section 6.1.4. It should be underlined that only a small amount of hydrogen is incorporated for obtaining significant reduction: indeed the presence of hydrogen in the atmosphere in its molecular form affects negligibly the hydrogen content of the substrate with respect to other hydrogen - free dry treatments, as observed in the case of reduction in dry atmosphere from FTIR measurements (figure 4.20). On the other hand, all the wet treatments resulted in an increase of the hydrogen content in the sample. This means that under our experimental conditions the dissociation of the H_2 molecule at 500 °C introduces much less OH groups than the dissociation of water in OH^- and H^+ at 900 °C, therefore the most important cause for the hydrogenation of the samples is the presence of water in the atmosphere.

Concerning the effect of the different gases on the crystal matrix, in the following an interpretation that accounts for several of our observations is attempted. It is known that in lithium niobate, when treated at high temperature, some lithium oxide tends to out-diffuse. This out-diffusion on one hand leads to the presence of different vacancy defects, and on the other may cause the precipitation of $LiNb_3O_8$ phase according to the reaction

$$3LiNbO_3 \rightarrow LiNb_3O_8 + Li_2O \tag{6.17}$$

However, the Li - out diffusion is not the only condition necessary for the creation of $LiNb_3O_8$, as it has been demonstrated [37] that its formation does not occur in samples previously dehydrogenated. A possible interpretation of this phenomenon may be suggested: the out-diffusing species may be also lithium hydroxide, besides lithium oxide, according to the reaction

$$3LiNbO_3 + OH^-_{(s)} + H^+_{(s)} \rightarrow LiNb_3O_8 + 2LiOH \tag{6.18}$$

where $OH^-_{(s)} + H^+_{(s)}$ are natively incorporated in LN crystals produced in the presence of humidity. This reaction explains why wet atmosphere inhibits $LiNb_3O_8$ formation (as many authors already reported): the abundance of water in the atmosphere inhibits the out-diffusion of $OH^-_{(s)} + H^-_{(s)}$ from the crystal, hence displaces the equilibrium to the left part of the reaction. Consistently, the wet treatments did not produce any trace of lithium triniobate. Reaction 6.18 also explains why dehydrogenated samples do not decompose: the reaction does not occur since $OH^-_{(s)} + H^-_{(s)}$ are absent inside the crystal. Also Fe appears to play a role in the above mentioned reaction, in fact on the Fe doped faces less disorder and no $LiNb_3O_8$ formation were observed. A possible explanation may be that Fe lowers the OH content of the doped layer, according to the mechanism proposed by [38]:

$$Fe^{3+} + OH^- + \frac{1}{2}H_2 \rightarrow Fe^{2+} + H_2O \tag{6.19}$$

	oxygen	oxygen, N_2 + H_2	argon
dry	$(-221 \pm 2) \times 10^{-6}$	$(-197 \pm 2) \times 10^{-6}$	$(-89 \pm 3) \times 10^{-6}$
wet	$(-272 \pm 2) \times 10^{-6}$	$(-42 \pm 5) \times 10^{-6}$	$(-93 \pm 3) \times 10^{-6}$

Table 6.3: Maximum relative lattice mismatch measured at the surface of six samples treated under different atmospheres.

This local depletion of OH groups inhibits in turn out-diffusion and $LiNb_3O_8$ formation. This interpretation is corroborated by the fact that Fe^{2+} is more abundant in wet post-treated sample with respect to dry post-treated one, as demonstrated by optical absorption spectra. The presence of $LiNb_3O_8$ was detected only on the undoped face of samples treated in Ar and N_2 + H_2 dry and not in the samples treated in O_2 dry atmosphere. This feature can be explained by asserting that Ar and N_2 + H_2 dry atmospheres induces more out diffusion than O_2 dry, as corroborated by the higher defectivity of the former with respect to the latter: the $LiNb_3O_8$ precipitation reaction in dry conditions 6.17 should be indeed favoured if the atmosphere is oxygen poor. Thus precipitation of $LiNb_3O_8$ leads to a detectable amount of $LiNb_3O_8$ only in dry Ar and N_2 + H_2 atmosphere, and not in dry O_2 atmosphere.

The presence of the diffuse scattering on the reciprocal space maps in figure 4.12 can be related to defects produced by oxygen and lithium oxide out-diffusion (oxygen vacancies and rearrangement of the cationic distribution). The maps evidenced that the damage appears particularly severe for Ar treated and N_2 + H_2 treated samples. The presence of defects associated to oxygen out-diffusion is also confirmed by depth resolved polaron luminescence measurements, which showed an increasing abundance of Nb antisites approaching the surface. Raman data have been interpreted stating that Fe pushes Nb ions from antisite to their natural site, in accordance with PL data that indicate less antisites on the doped face with respect to the doped one.

Concerning the structural characterisation of the Fe doped layer, the approaches used in this work complement each other, as HRXRD is sensitive to the average long range characteristics of the lattice, while micro Raman spectroscopy is sensitive to the short range interactions determining the vibrational dynamics of a given sublattice and may be used to probe any change related to the introduction of defects in the lattice. HRXRD measurements indicate that the incorporation of iron in general leads to a shrinkage of the lattice and the values of the maximum relative lattice parameter difference are reported in table 6.3. The low level of deformation of the two Ar diffused samples with respect to the two oxygen as-diffused ones can be explained by the lower surface concentration of iron in these samples revealed by SIMS measurements (see figure 6.3). As already mentioned, since the post-treatment does not affect the concentration of Fe, the lower mismatch detected on the post-treated samples, with respect to as-diffused ones, is related to the valence state change of Fe. However it must be underlined that the relieving of lattice deformation is different between the dry and wet post-treatment: in the former case is only of 10%, while in the latter case the deformation is suppressed up to about 80%. The reasons for this difference are still under study.

Raman data show that the frequency of the $A_1(TO_1)$ and $A_1(TO_4)$ phonons presents in all the samples a non negligible increase from the substrate to the surface with a profile analogous to the Fe concentration profile obtained by SIMS. It is interesting to note that there is no correlation between this frequency increase and the lattice deformation measured by HRXRD. In particular the sample post treated in wet atmosphere has the lowest mismatch, but the frequency increase of Raman modes is not significantly different from other samples. This fact leads to the conclusion that the frequency change is purely due to a change in short range order induced by the Fe doping and not to indirect effects such as the deformation of the lattice. The phonon frequency increase with Fe incorporation reflects a strengthening of the chemical bonds, similarly to what happens in undoped crystals when going from congruent to stoichiometric composition. This fact gives an indication that the Fe incorporation directly improves affects the vibration of the Nb sublattice. The detailed understanding of the modifications induced by the Fe ions are under study.

Finally, concerning the very surface of the samples, AFM images presented in figure 4.10 revealed only on the doped surface of samples treated under dry atmosphere the presence of a thin textured morphology. There is no correlation between this structure and $LiNb_3O_8$, since $LiNb_3O_8$ was detected on the undoped face of samples treated in Ar and $N_2 + H_2$, which appeared flat and smooth in AFM images. Moreover, SIMS revealed no compositional alteration at the very surface of these samples. It can be concluded that this structure does not consist of a phase other than LN, or that it is so thin that it could not be detected. Its presence is related to Fe and the absence of water vapour. It can be argued that it is a kind of fingerprint left by the residual layer: if the residual layer has an island microstructure, as already reported for Ti in-diffusion [28], when LN grows underneath the residual layer, gradually consumes it keeping memory of its morphology. Since strong differences between dry and wet atmosphere on the evolution of the surface during Ti in-diffusion were already reported [30], it is reasonable to presume that similar differences occur also in the case of Fe in-diffusion: an investigation of the morphology of the residual layer is thereby needed and a compositional investigation, analogous to the one presented in section 3.2, will be performed also in the case of wet atmosphere, in order to confirm this hypothesis.

6.2 Advances in Fe:LN characterisation tools

6.2.1 Spectrophotometric quantification of Fe

Section 4.1 reported a deep investigation of optical absorption spectra and demonstrated the possibility to obtain a complete determination of Fe concentrations by using optical absorption measurements solely. Indeed to determine the total Fe concentration, regardless of its reduction degree, it suffices to measure the optical absorption at 342 nm and exploit the cross section at that wavelength, calculated in section 4.1.3, according to the relation

$$C_{\mathrm{Fe}}[\mathrm{cm}^{-3}] = \frac{\alpha_{342}[\mathrm{cm}^{-1}]}{(13.1 \pm 0.2) \times 10^{-18}\mathrm{cm}^2}$$

where C_{Fe} is the total Fe concentration and α is the measured absorption coefficient.

The absorption at 532 nm can furthermore give the Fe^{2+} concentration, according to the relation:

$$C_{\mathrm{Fe}^{2+}}[\mathrm{cm}^{-3}] = \frac{\alpha_{532}[\mathrm{cm}^{-1}]}{(3.95 \pm 0.08) \times 10^{-18}\mathrm{cm}^2}$$

where the cross section was determined from experimental data [19]. Finally the Fe^{3+} concentration can be calculated as the difference $C_{\mathrm{Fe}} - C_{\mathrm{Fe}^{2+}}$.

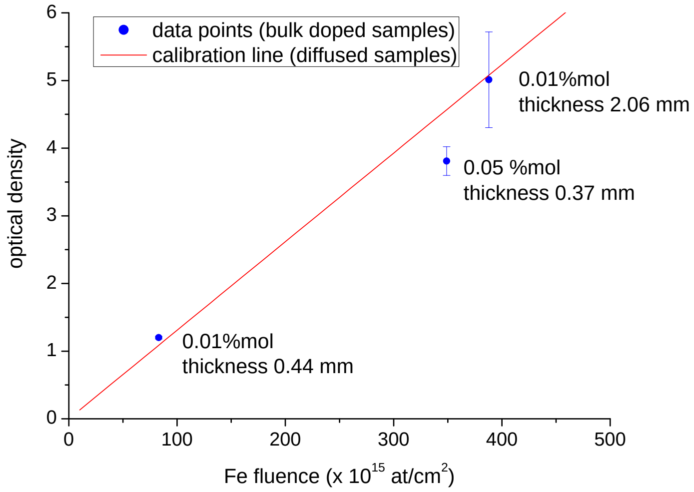

Figure 6.5: Optical densities at 342 nm of three bulk-doped Fe:LN samples compared to the calibration line obtained from samples doped by thermal diffusion.

Hence by only measuring the optical absorption at two wavelength it is possible to characterise the sample composition. It is useful to extend this method also to bulk doped Fe:$LiNbO_3$.

Bulk doped Fe:$LiNbO_3$

It is known that many dopants, among which Fe, are not incorporated at constant concentration during Czochralski growth [39] therefore different parts of the boule may contain different Fe concentration. Moreover, if Czochralski growth is performed in air, the reduction degree of the as-grown material depends on the specific growth conditions (e.g. humidity). Fe can also constitute an unwanted impurity for applications that require the absence of optical damage, as a consequence a simple method for Fe quantification is desirable. The absorption at the isosbestic point, using the effective cross section calculated above, can be a useful tool for determination of Fe concentration also for bulk doped samples, provided that the intensity of the light transmitted by the sample at 342 nm is measurable. This method was checked on boules of Fe:$LiNbO_3$, grown with nominal concentration 0.01 mol% and 0.05 mol%. Nominal concentration is simply calculated from the amount of iron oxide added to the melt before Czochralski growth. An absorption spectrum of one of these samples was already shown in figure 1.11: it has the same features as the ones found in literature [17] [20]. Two samples were cut and polished from the boule doped with 0.01 mol% of Fe, and one from the boule doped with 0.05 mol%. Their thickness was accurately measured, and the nominal number of Fe atoms per unit area, i.e. the fluence, was calculated. The optical densities at 342 nm are plotted as a function of the nominal fluence in figure 6.5, where the fitting line derived from diffused samples in figure 4.6 is plotted for comparison. The optical densities values for samples cut from 0.1 mol% doped boule are close to the calibration line, while the optical density of the other sample is lower than it should, indicating that the actual concentration is lower than 0.5 mol%.

6.2.2 SIMS analysis of Fe:LN

In this work, SIMS technique has been widely exploited for compositional characterisation of Fe:LN. In particular work was devoted to optimisation of measurement conditions already known and experimented before, as well as exploration of new ones. In the following, a short summary of what described in appendix A is reported.

For the determination of the diffusion coefficient of Fe, depth profiles were obtained in negative mode, with 14.5 keV primary beam at high current (100 - 150 nA) on completely diffused Fe:LN with a metallic grid and normal incidence electron gun for charge compensation. Within this investigation, it was possible to determine the relative sensitivity factor for Fe in LN, which allows to derive directly the absolute concentration of Fe from the normalised Fe signal: this datum will be very useful for future work on Fe:LN samples obtained both by thermal diffusion and from bulk doping.

SIMS investigation allowed to discover the presence of the residual layer: for the analysis of its composition, the above described conditions do not allow enough depth resolution. Therefore a lower energy setup was employed, with a 7 keV primary beam at low current (5 - 10 nA), with normal incidence electron gun for charge compensation. The possibility of carrying measurements without electron gun was successfully tested on samples with residual layer, because the layer is enough conductive to provide an efficient sink for excess charges, thus avoiding charging up. Also for samples without residual layer, charge compensation can be achieved without electron gun, thanks to a metallic thin film, deposited on the sample by sputtering deposition before SIMS measurement, which also in this case acts as a sink for excess charges. During depth profiling, the metal atoms are pushed in the substrate by recoil implantation, producing a tail in the depth profile, whose decay length has been measured and used for profile correction.

To improve depth resolution, also detection of CsM^+ ions in positive mode with a 5.5 keV primary beam was tested: also in this case charge compensation was achieved thanks to a metallic thin film. Secondary ion yields of CsM^+ ions, and their ratios, are completely different from yields of M^- ions in negative mode, and undergo different surface effects: as a consequence, comparison between depth profiles obtained in negative and in positive mode allowed to gain much more information on the composition of the residual layer, than the information obtained by depth profiles in negative mode solely.

Besides recoil implantation, other artefacts have been observed and investigated, and many features in LN depth profiles have been interpreted also with the help of simulations.

Finally, SIMS ion imaging was exploited to estimate the lateral diffusivity of Fe. The main experimental problem that strongly limits the results quality is the size of the primary beam. Indeed it cannot be focused much without losing its intensity: this implies that if the spectrometer is used in microprobe mode, the lateral resolution is not sufficient, since it is linked to primary beam size. In the microscope mode instead, lateral resolution is determined by the transfer ion optics: this second mode is adopted, but also in this case the large size of the primary beam constitutes a problem. As a matter of fact, given the same primary beam current, the sputtering rate is the same, but the current density on each analysed point is lower the larger the primary beam is. As a consequence, also the secondary ion yield is lower, and each ion image plane contains very few counts. Therefore, results have been obtained by accumulation of several image planes, i.e. after integration over a certain depth. In summary, the main problems to solve in order to improve ion SIMS ion imaging have been identified, and other experimental conditions will be tested in the future.

6.3 Choice of best conditions

According to the results presented so far, important conclusions can be drawn with the purpose of choosing the best conditions to produce the final device. Diffusion in argon leads to defects, non reproducible diffusion profiles, non sufficient reduction degree: for these reasons diffusion in argon has to be discarded. Diffusion in oxygen has an acceptable degree of reproducibility and induces less defects, but it results in completely oxidised samples: however a post-diffusion annealing at 500 °C in a gas mixture containing hydrogen proved to be effective for obtaining the desired reduction degree, it does not modify the diffusion profile, moreover it is reversible. As a consequence it allows to decide separately the diffusion profile and the reduction degree. For these reasons, this method is chosen as the best way to produce the final device. In choosing the best annealing atmosphere, it should be also reminded that hydrogen was recognised as responsible of dark conductivity, therefore the photorefractive properties of a crystal containing hydrogen are expected to be unsatisfying. The amount of hydrogen introduced in a crystal after a reducing treatment under hydrogen gas is very small, negligible with respect to the amount normally present in virgin LN: thus the reducing treatment in hydrogen gas is expected to affect negligibly the dark conductivity. On the contrary, annealing in wet atmosphere introduces a large amount of hydrogen in the crystal. Nevertheless wet atmosphere is advisable for obtaining good crystal quality: first of all, it prevents the formation of the textured microstructure, which was observed on the doped face after dry diffusion; second, it prevents Li outdiffusion and related defects, in particular the formation of $LiNb_3O_8$ on the undoped surface. In order to benefit from wet annealings and at the same time minimise the hydrogen content, a possible solution is the dehydrogenation of the substrate. It is reported [11] that hydrogen can be introduced/removed by performing annealings at 400 °C or more in wet/dry atmosphere for several hours. Thus, after diffusion and post-treatment in wet atmosphere, the sample can be treated at 400 °C under inert gas, until the hydrogen concentration get sufficiently low.

As result of the diffusion study in chapter 3, the mean diffusivity values were determined. It is therefore possible, with reasonable uncertainty, to forecast the diffusion profile that will be obtained given the temperature and duration. On the other hand, it is possible to determine a proper combination of parameters (fluence, temperature, duration) to obtain a given diffusion profile. The requirements of the final device are:

- constant concentration of Fe over the waveguide depth ($2 \div 3$ µm);
- surface concentration lower than 0.1 mol%, which is the maximum acceptable for permanent photorefractive recording [3].

Of course these requirements can be fulfilled with infinite combinations of diffusion parameters. The surface concentration can be lowered at wish by simply lengthening the duration, at any temperature and fluence. However the lateral diffusion should be minimized, therefore one must find the shortest duration and the lowest fluence that fulfil these requirements. The lowest fluence is determined by the shortest deposition duration: 60 s was established as the shortest duration to avoid big uncertainties on the fluence. Therefore the smallest fluence is 25×10^{15} at/ cm^2. Then the duration needed to obtain 0.1 mol% (which corresponds to 1.9×10^{19}at/cm^3) at the surface

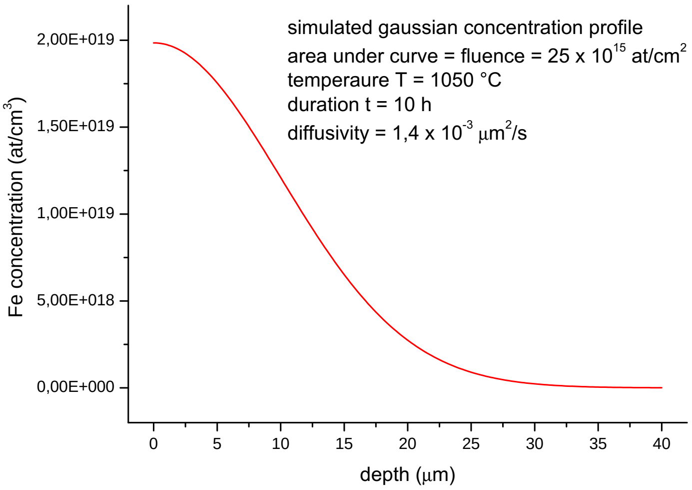

Figure 6.6: Simulated concentration profile for 10 hours of diffusion at 1050 °C.

can be determined by simulating a gaussian curve using the average diffusivity values found in section 3.4. By way of example, 10 hours at 1050 °C are sufficient to obtain the desired surface concentration, as the simulation in figure 6.6 shows.

When the number of Fe atoms is lower than the number of electrons introduced, electrons start to populate polaron and bipolaron states: adopting the usual reducing conditions, this happens after less than 1 hour for samples containing 25×10^{15} at/cm^2.

In summary, the optimal procedure is

- deposition of 25×10^{15} at/cm^2;
- diffusion in wet oxygen for 10 h at 1050 °C;
- post treatment at 500 °C in Ar + H_2 for 30 min;
- dehydrogenation at 400 °C of the substrate.

6.4 Feasibility and critical points of the final device

6.4.1 Waveguides

As already mentioned in the introduction, the final device consists of waveguides created in the same monocrystal, in particular a planar waveguide is located in the Fe - doped region. Waveguides are usually produced by ion implantation with O, C, or other elements. After implantation, a thermal treatment is required to recover damage and allow rearranging of ions. Many questions arise from the technical point of view, in particular about the sequence of the preparation stages. Indeed Fe doping and reduction should be performed before implantation, and implantation itself may affect the distribution of iron in the substrate. Moreover, the thermal treatment after implantation may alter the reduction degree of Fe. For these reasons the production of the final device must be accurately tested from the technological point of view.

Less expensive ways to create waveguides are Ti in-diffusion and proton exchange [2]. Double diffusion of Ti and Fe has already been done [26]; Ti diffusivity in LN is much lower than Fe diffusivity [25] and requires higher temperature and longer annealing. Moreover the introduction of Ti ions stabilises Fe^{2+}, giving a non constant reduction degree over the waveguide depth [40]. As a consequence Ti diffusion should be performed before doping with Fe, and the doping and annealing parameters should be carefully calibrated in order to obtain both the desired Fe concentration and the desired waveguiding properties. Proton exchange waveguides are obtained at low temperature by treating LN with an appropriate acid which provides hydrogen ions that substitute for Li ions, changing the refractive index [11]. In this case, the effect of proton exchange on Fe doping and its reduction degree must be carefully investigated.

6.4.2 An alternative: Fe ion implantation

Another way to produce the Fe doped region can be ion implantation: in fact, ion implantation allows to simplify the preparation for many reasons. First, no photolithographic mask would be required to dope the substrate in a well defined region; second, the device requires in any case ion implantation to create the waveguides, therefore only one apparatus would be needed to obtain both dopings; third, by performing subsequent implantations with different energies it is possible to achieve a more suitable doping profile; forth, thermal treatments are still needed to recover implantation damage, but with much shorter duration than those required for diffusion, thus limiting the problem of lateral diffusion. Obviously in order to define the best conditions to obtain the device by ion implantation it will be necessary to start a new study on fluences, energies, annealings, etc. However many of the results obtained in this study will be useful also for implanted substrate, e.g. the investigation on reducing treatments, the characterisation by optical absorption. First demonstrative implanted samples were produced in New Delhi, India. They were produced by using three different impact energies, and a Fe interlayer to reduce the end of range. These samples are currently under study.

6.4.3 An alternative: bulk doping and local reduction

As discussed in chapter 5, laterally confined doping presents several problems: lateral diffusivity is much higher than in-depth diffusivity, as a consequence the doped region results broadened and blurred. However, a planar waveguide smaller than the doped region can overcome this problem. The problem which limits seriously the feasibility of the device is the gradient of reduction degree. Direct experimental measurements show that lateral gradient of reduction degree is much wider than the lateral concentration gradient. Analogously it is reasonable and likely that the in-depth gradient of reduction degree is wider than the in-depth concentration gradient, i.e. that the reduction degree is not constant over the diffusion profile, instead the electrons are all trapped away from the undoped region, near the surface. A depth-resolved spectrophotometric technique could unravel this doubt, however it is supported by polaron luminescence measurements, which show that the behaviour of electronic transitions is not constant in the first 2 - 3 μm, where the planar waveguide should be located. It is difficult to get rid of these problems, which arise all from diffusion and thermal treatments.

A possible way out is to avoid diffusion at all. Indeed the device is in principle feasible even if it is entirely uniformly doped with Fe, provided that all Fe is Fe^{3+}, otherwise unwanted absorption of light in other stages of the device would occur. Therefore the alternative consists in arranging a bulk doped sample with a very low percentage of Fe^{2+}, then performing reduction only in the desired region. Falk and Buse [41] proposed a thermo-electric method for nearly complete oxidation of Fe:LN, which can be applied to crystal grown by the Czochralski method after doping the melt with Fe_2O_3 for obtaining doped substrates with very low absorption. To achieve local reduction, it is necessary to adopt a different reduction method. A possible method, currently under evaluation, consists in applying a photolithographic mask that leaves exposed only the part to be reduced, then soaking the sample in a reducing solution, i.e. a solution capable of introducing molecular hydrogen in LN. The process should occur at room temperature, or at the boiling point of the solution employed: reduction should be much slower and better controllable.

6.5 Perspectives

This work dealt with the optimisation of the material making use of many characterisation techniques, and established how to obtain the desired concentrations and reduction degrees: these two parameters are determinant in photorefractive response. The characterisation of the photorefractive properties of Fe diffused layer and the choice of optimal concentration and reduction degree will be the subject of a PhD thesis by A. Zaltron.

Apart from holographic memories, another interesting application of Fe diffused layers in integrated optics are permanent reflection Bragg gratings [42]. For instance, diffusion of Fe on the end face of a LN crystal was exploited to create a photorefractive grating which acts as a mirror for a laser cavity in Er:LN [43]. Such photorefractive stages can help to build up dense wavelength division multiplexing systems for optical communications, or may be used to build optical sensors for temperature and electric field measurement, to detect gases or complex biological molecules. Such sensors make use of the narrow spectral resonance of the holograms, where the filter reflectivity is already changed for very small effective index changes of the guided light.

Appendix A

Secondary Ion Mass Spectrometry

SIMS is an analytical technique that can be used to characterise the surface and near surface (circa 30 micron) region of solids. The technique uses a beam of energetic 0.5 - 20 keV primary ions to sputter the sample surface, producing ionised secondary particles that are detected using a mass spectrometer. The primary beam can be O_2^+ (typically used for detection of electropositive species) Cs^+ (for electronegative species) or many others (Ar^+, O^{2-}). The sputtering process is not just a surface layer phenomenon, but consists of the implantation of the primary species into the sample and the removal of surface atoms by the energy loss of the primary species in the form of a collision cascade. Many species are formed by the interaction of the beam with the sample, but the positive and negative secondary ions are the species of interest for SIMS.

In the present work SIMS was used to characterise bulk and surface composition, and Fe concentration in-depth profile of our Fe:$LiNbO_3$ samples. The magnetic sector SIMS, its ion optics and its operating modes are described in detail, then experimental issues and artifacts are discussed, referring in particular to bare $LiNbO_3$ and $LiNbO_3$ covered with metal or other thin films.

A.1 CAMECA ims 4f

A magnetic sector SIMS instrument by CAMECA (model ims 4f) was used. A scheme of this apparatus is given in figure A.1. The instrument is equipped with two ion sources, a duoplasmatron, which ionises gases, in this case oxygen (not used in this work) and a solid state source. Solid state source consists of a reservoir containing cesium chromate raised to a temperature of 400 °C; the cesium vapour thus produced comes into contact with a tungsten tablet, heated at 1100 °C and gets ionised to Cs^+. Reservoir and ioniser are brought to a voltage $V_P = 10\,\mathrm{kV}$ and heated independently by electronic bombardment by two annular filaments. One electrode, placed in front of the ioniser at ground potential, extracts and accelerates Cs^+ ions towards the primary column. A magnetic mass filter bends the ion trajectories to the axis of the primary column, which consists of three electrostatic einzel lenses, deflectors and diaphragms, to bring a focused ion beam to the sample. The nominal incidence angle of the beam on the sample is 30 degrees. The position of the beam on the sample can be adjusted

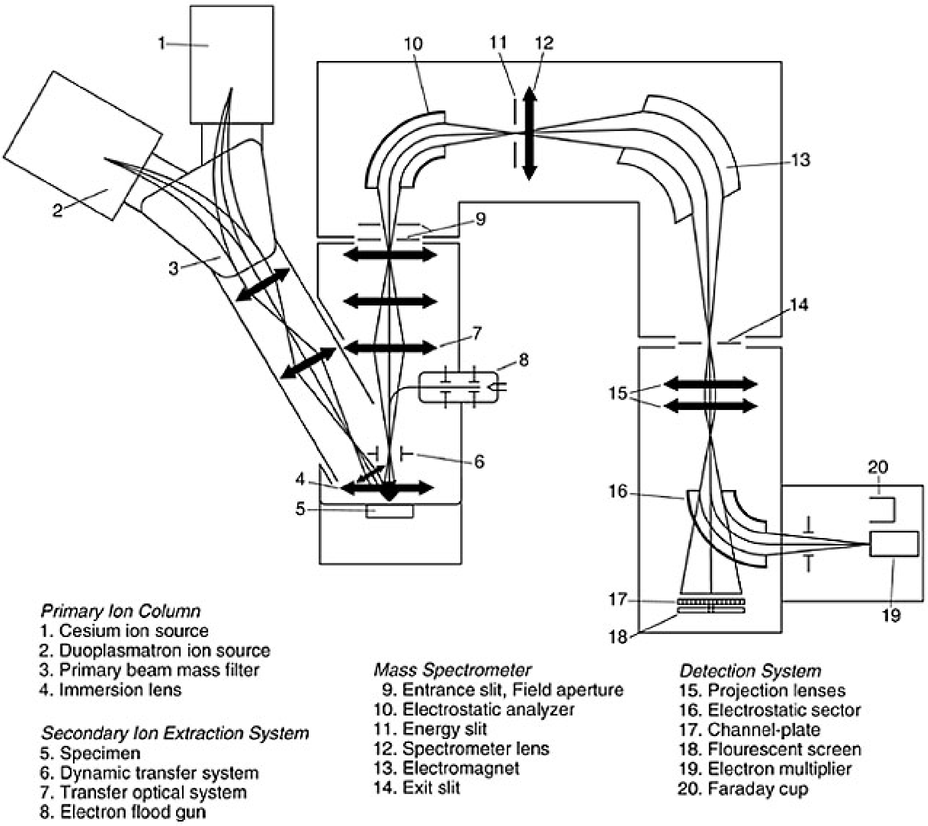

Figure A.1: Scheme of secondary ion mass spectrometer CAMECA ims 4f.

V_P	V_S	true incidence angle	depth resolution
10 kV	4.5 kV	24.5°	10 nm
4.75 kV	2.25 kV	24.3°	6 nm
2.5 kV	4.5 kV	17.4°	7 nm
10 kV	−4.5 kV	42.4°	4 nm

Table A.1: For each couple of accelerating voltages applied to primary column V_P and to sample V_S, the table reports the calculated incidence angle and the corresponding depth resolution.

thanks to two couples of deflection plates, placed at the end of the primary column. These deflectors allow also to raster the beam over the sample surface: raster is needed to obtain an homogeneous erosion of the sample and produce a flat bottom crater. Raster size can be adjusted to obtain a square crater up to $500 \times 500\ \mu\mathrm{m}^2$.

An electrode (extraction plate) at ground potential separates the primary column from the sample chamber. The sample itself is kept to a potential $-V_\mathrm{S}$ which depends on the sign of secondary ions to be detected. If negative secondary ions are needed, the potential is negative with respect to extraction plate (negative mode): this negative potential further accelerates primary ions, hence the impact energy of primary ions is $E_\mathrm{P} = q \cdot (V_\mathrm{P} + V_\mathrm{S})$. The nominal incidence angle differs from the true one due to the fact that in the region between the extraction plate and the sample the electric field, normal with respect to sample surface, has a component orthogonal to the beam's trajectory which deflects it. The true incidence angle θ is given by

$$\tan\theta = \frac{\sin(30)}{\left(\cos^2(30) - \frac{V_\mathrm{S}}{V_\mathrm{P}}\right)^{1/2}}$$

Table A.1 reports incidence angles for the most used combinations of parameters. The primary beam impinging on the sample causes a collision cascade, involving a wide region inside the sample, where atoms get displaced from their original position, and primary ions get implanted. Atoms from the uppermost atomic layers may gain from collisions enough energy to escape the surface (sputtering process) and be ejected as single ions, molecular ions or neutrals. Each particle is ejected from a point which is in the neighbourhood of its original site in the solid: this makes local analysis possible. Sputtered particles have a certain probability of becoming ionised as positive or negative ions during the ejection process. Secondary ions comprise single and multiple charged ions as well as clusters of several atoms: in general, but not always, the single charged ions have intensities higher than the others. In negative mode only negative secondary ions are attracted to the extraction electrode and collected by the secondary ion column. The secondary column transfers a laterally resolved image of secondary ions and separates them depending on their mass to charge ratio. It consists of transfer optics, an electrostatic sector and a magnetic sector.

The energy distribution of the secondary ions has a peak at few eV, more or less narrow according to the type of ions, and their direction spread in a solid angle of nearly 2π radians. Between the sample and the extraction plate, secondary ions are accelerated and the divergence of the pencil of trajectories stemming from each point of the surface is strongly reduced. Then an electrostatic lens (immersion lens) brings each pencil to focus on an image plane, where an enlarged image of the surface is produced. The plane where the pencil of trajectories cross is referred to as pupil or cross-over

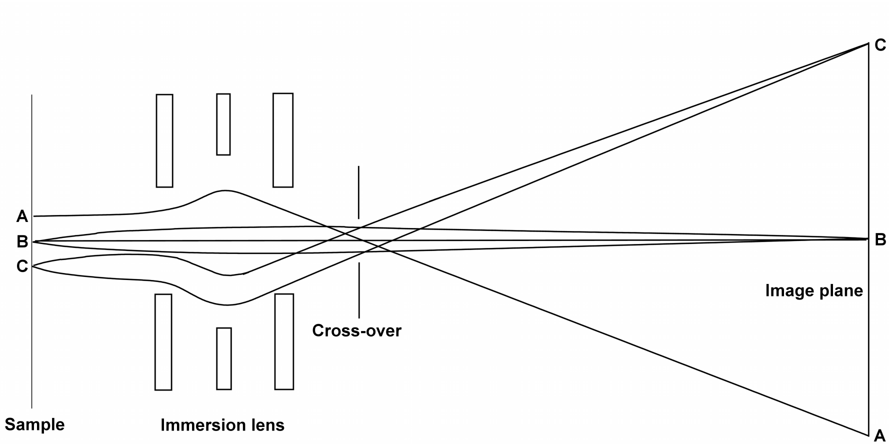

Figure A.2: Schematics of transfer ion optics: the immersion lens brings each pencil of ion trajectories to focus on an image plane, where an enlarged image of the surface is produced.

plane (figure A.2). The collecting system can be characterised by a virtual image containing all spatial information and by a virtual cross-over containing information on the angular distribution. The couple image and cross-over is transferred to the mass spectrometer by the transfer optics. It is made up of an electrostatic transfer lens (adjustable to three different potential values) which creates another cross-over plane: a diaphragm ("contrast diaphragm") is placed here to limit the aperture angle of the pencil. It reduces blurring due to chromatic and geometrical aberrations, it controls the collection efficiency and limits the spatial resolution. Another diaphragm is placed in the subsequent image plane, called "field aperture" because it limits the field of view. Four different sizes can be chosen for both field and contrast apertures: the many combinations of transfer lens, contrast aperture and field aperture offer great flexibility in magnification of the surface image, field of view of the surface image, and collection solid angle. The transfer optics can also be operated in a dynamic mode: in dynamic transfer system, deflection plates are added in correspondence to the cross-over plane between immersion and transfer lenses. These deflection plates operate synchronised with the primary beam scanning device, in such way that secondary ions emitted by the point of the sample hit by the primary beam at a certain instant are deflected along the central axis and pass through the field aperture. This mode allows to analyse areas larger than the field of view.

The magnetic sector consists of an electromagnet and an exit slit: the adjustable magnetic field bends the ions trajectory with a radius which depends on their mass to charge ratio: given a certain value of B, only ions with the corresponding m/q will exit the slits, the others being stopped. The radius of curvature depends also on the kinetic energy, which is given by the initial kinetic energy of the secondary ions plus the energy gained from the secondary accelerating potential. The distribution of kinetic energies results in a distribution of trajectories ("chromatic effect"): to avoid this problem, the electrostatic sector is used. It consists of two curved plates polarised at proper potentials, which deflects the ions with a radius of curvature that depends on their kinetic energy, and a slit (energy slit). By choosing properly the potential and the width of the slit, only ions in a defined energy range can enter the magnetic sector. A lens between the electrostatic sector and the magnetic sector (spectrometer lens)

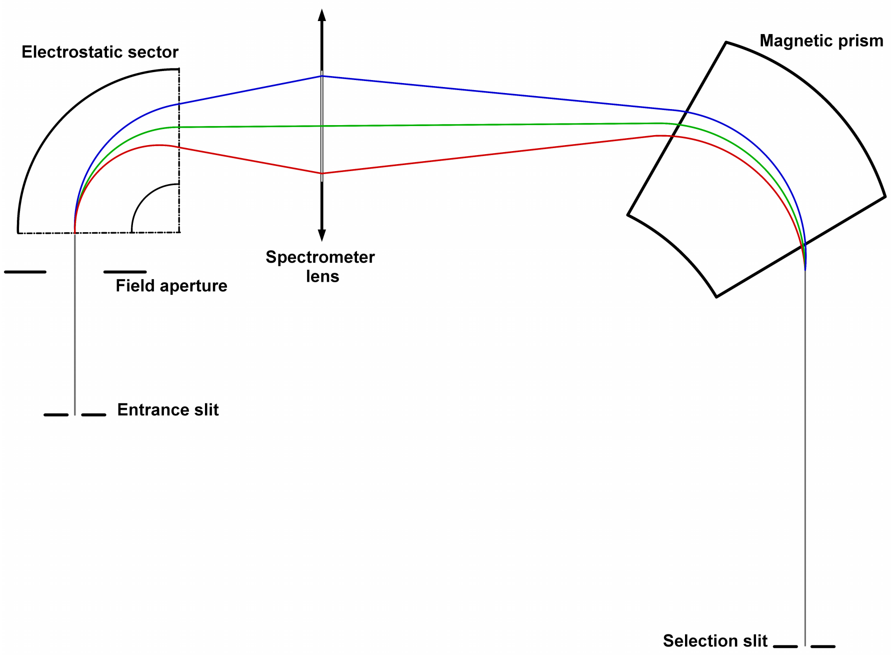

Figure A.3: Schematics of double sector spectrometer evidencing the role of the spectrometer lens, which brings into focus trajectories of ions with different kinetic energy.

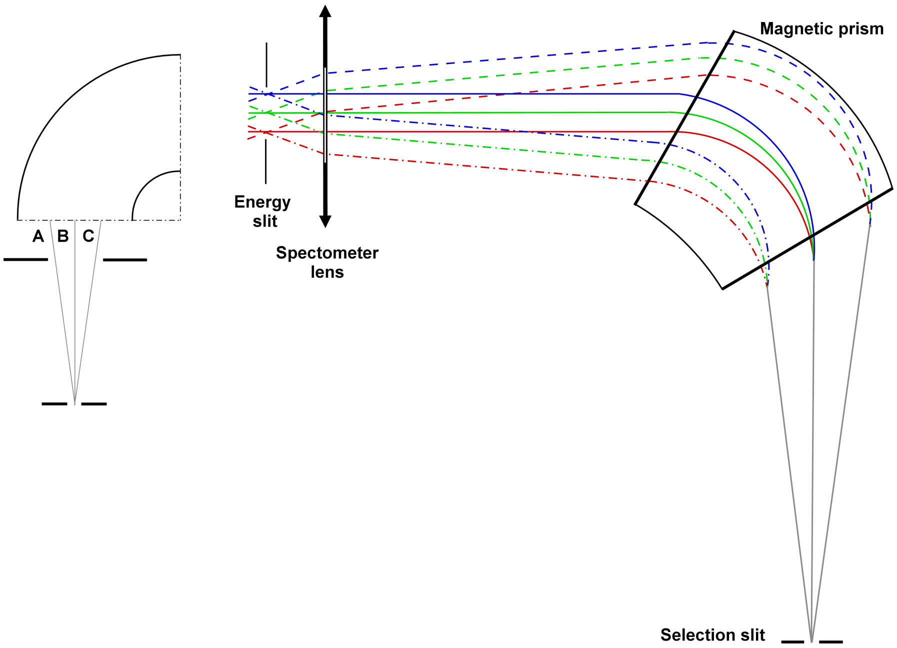

Figure A.4: Schematics of double sector spectrometer evidencing that it is achromatic and astigmatic.A, B, C refer to ions trajectories coming from different points of the sample.

brings the diverging trajectories of ions exiting the energy slit and focus them again at the exit slit, as schematised in figure A.3. The setup is arranged in such way that the energy dispersions produced by both prisms cancel each other, i.e. the spectrometer is achromatic. If for instance three ions are emitted from three different points A, B, C in the direction normal to the surface, as shown in figure A.4 their trajectories will pass in the same point of the cross-over; the electrostatic prism will make them cross again in another cross-over plane before the spectrometer lens, then in another cross-over plane located in correspondence of the exit slit. Also the trajectories of ions with different energies (blue, green, red) are separated by the electrostatic prism but merge again at the end of the magnetic sector ("achromatic point"). Finally, ions coming out from the mass selection slit have a mass range which depends on the size of the cross-over and the width of the slit, determining the mass resolution of the spectrometer. Finally the secondary ion image is transferred by a projection system which focus the image on a channel plate which transforms the ion image into an electron image observed on a fluorescent screen. Secondary ions can also be simply counted by an electron multiplier or a Faraday cup.

The progressive erosion of the material gives access to inner regions of the sample. An in-depth profile is obtained by recording the secondary ion currents as a function of time. In this type of analysis, a number of masses, corresponding to the secondary ions to be monitored, is chosen; the measurement is carried out in cycles, in each the magnetic field is increased from the lowest to the highest value and stops at each selected mass while the detectors count the incoming secondary ions; each cycle adds a point in the depth profile for each selected mass. The sampling frequency of the depth profile is therefore limited to the depth sputtered during one cycle, which in turn depends on the sputtering rate and on the duration of each cycle.

A mass spectrum is produced by sputtering a sample while the mass spectrometer scans the mass range. If the sample surface is sputtered very lightly, only the uppermost monolayers are removed, thus providing surface information (static SIMS). When the sample is sputtered rapidly while scanning the mass, a bulk analysis can be obtained. Depth profiles are obtained if one or more masses are monitored sequentially by switching among masses. The detected signal from the chosen species occurs from increasingly greater depths beneath the original sample surface (dynamic SIMS).

A.1.1 Normal incidence electron gun

When a beam of charged particles interacts with an insulating sample, electrical charging-up occurs. In SIMS experiments charges are brought in by the primary ion beam, or left behind by the outgoing secondary particles. According to the sign of the secondary ions being collected, two typical cases have to be considered. In positive mode, the total secondary ion yield is usually lower than one, therefore positive primary ions produce positive charge on the sample, whereas negative primary ions produce negative charge. Also the contribution of secondary electrons accelerated towards the sample must be taken into account. In negative mode, secondary electrons and negative ions are extracted as well. The electronic yield is usually much higher than one, therefore especially with positive primary ions, a positive charge appear on the sample. To prevent subsequent charge buildup, the instrument is equipped with an electron gun which provides an auxiliary electron beam moving along the optic axis, producing a self-regulated equipotential surface on any type of insulator. The electron gun delivers a beam with energy V; the beam enters a magnetic prism (located between the first cross-over plane and the transfer lenses) which deviates the electrons

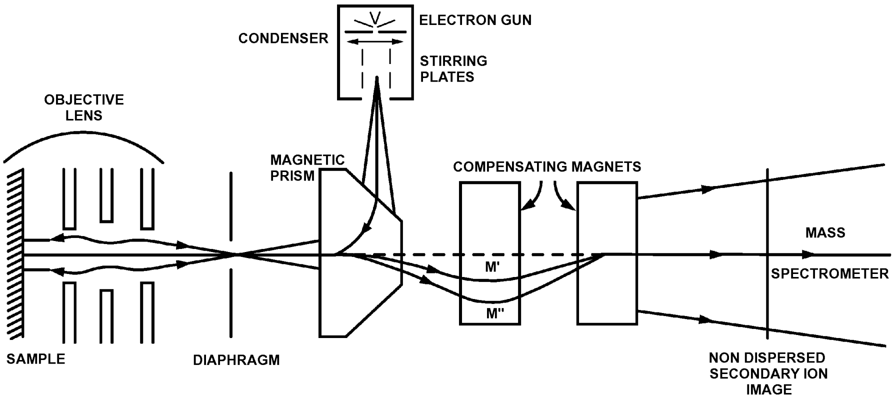

Figure A.5: Scheme of normal incidence electron gun and modified secondary ion optics.

by an angle of 90°, so that their trajectories coincide with the optic axis, i.e. they travel the same path as secondary ions, but in opposite direction. In order to reach the sample, they must have enough energy to overcome the decelerating potential applied to the sample, namely they must be accelerated by a potential $V \geq V_S$. This set-up provides a swarm of very low energy electrons directly near the surface. Since the magnetic prism affects also the trajectories of secondary ions, two compensating magnets (figure A.5) are placed between the magnetic prism and the transfer lenses, which must be properly adjusted to obtain a non dispersed secondary ion image.

A.2 Analysis conditions for $LiNbO_3$

Since $LiNbO_3$ is an insulating material, electrical charging-up of the sample during the measurement must be avoided. Although positive mode is recommended for $LiNbO_3$ due to the higher yield of Fe, Li, Nb as positive ions,negative mode was mainly adopted because in our apparatus charge compensation is more efficient. In order to improve conduction near the sputtered region and to create an equipotential surface on the sample (that reduces the effect of charging on ion optics), usually a metallic thin film is deposited on the sample in positive mode; in negative mode it could be unnecessary because the neutralisation process is self-compensating.

A.2.1 Negative mode, deep craters

When the features of interest require the erosion of a deep crater, for instance 5 μm or more, as in the case of Fe in-diffusion profiles shown in section 3.3, a high sputtering rate is desirable to perform the measurement in a reasonable time. Thus the highest impact energy (14.5 keV) was adopted, i.e. by setting V_P = 10kV and V_S = 4.5kV. There are many problems related to deep craters. First of all, as the primary beam digs the sample, the crater's bottom gets smaller and smaller, worsening depth resolution, therefore the largest raster and the smallest field aperture are desirable. Moreover, since the incidence direction of the primary beam is tilted, the crater tends to become more and more asymmetric. The problem of charging-up is particularly severe because of high primary current required to increase the sputtering rate, and because the focus conditions of primary beam and electron beam change during the measurement due to the fact that the position of the surface being sputtered drifts progressively away. In the present work, craters up to 20 μm deep were often rather easily obtained.

Experiments proved that self-compensating neutralisation of charge is a condition difficult to obtain without a conducting surface on the sample: instead of covering each sample with a metallic film, a quicker solution is to lean a copper grid on the sample. Since it is in electric contact with the sample holder, it helps in keeping the surface equipotential and disposes of unnecessary electrons supplied by the electron beam. The rastered area is thus limited by the grid's mesh. When studying the iron diffusion profiles, typically the beam was rastered over 150 μm x 150 μm inside the 210 μm x 210 μm voids of the copper grid. The focused beam's dimension is a compromise between shape, homogeneity and current, and typically had a diameter of 30 μm. The primary beam's current was chosen according to the aim of each measurement. Primary beam's current density higher than 6 Am^{-2} do not allow a good charge compensation: for depth profiling, primary currents in the range 50 ÷ 100 nA, in some cases 120 nA were adopted. The corresponding sputtering rates were in the range 1.5 ÷ 2 nm/s. Concerning charge compensation, the electron current emitted from the tungsten filament was 2 ÷ 2.2 μA, and electrons are accelerated towards the sample by a potential difference slightly higher than the potential difference between sample and extraction electrode, i. e. 4503 ÷ 4504 V. Since the beam diameter is not so small compared to raster size, the resulting crater's sidewalls are not sharp, and the uniform bombardment requirement is fulfilled only at the centre. Therefore the smallest field aperture is used, to collect only ions coming from the central 8 μm diameter region. The smallest field aperture combined with a medium contrast aperture guarantees a significant number of secondary ion counts for each element detected in depth profile mode.

A.2.2 Negative mode, improved depth resolution

In the case of samples with residual layer discussed in section 3.2.3, best resolution on the first hundreds of nanometres is required. In the conditions described in the foregoing paragraph, with impact energy 14.5 keV and high current density, the sampling frequency (about 1 point every 10 nm) is too low to give detailed information on the residual layer, which is only few tens of nanometres thick. Hence much lower primary beam currents were adopted (10 ÷ 20 nA). Since the presence of the residual layer allows for a better charge compensation, larger grids could be used (300 μm x 300 μm) and therefore larger raster size, to further decrease the primary ion beam current density and increase the distance between crater walls and analysed region. However, measurements performed adopting these conditions disclosed the artefacts related to SIMS analysis, discussed in detail in the next section. Artefacts can be minimised by lowering the impact energy, or by increasing the tilt angle of the primary beam. The impact energy was therefore lowered to 7 keV using two different modes:

- V_P = 2 keVand V_S = 4.5 keV, using the electron beam for charge compensation;
- V_P = 4.75 keVand V_S = 2.25 keVwithout electron beam, since it is not possible to set it up for operating at so low secondary ion voltage.

Although the impact energy is the same, the incidence angle is different hence the sputtering rate is also different. As a consequence, results obtained in these two modes are not directly comparable. The second mode could be used only for few samples with residual layer where charge compensation could be easily accomplished probably due to better conductivity of the residual layer with respect to pure LN, which could not be measured in these conditions.

A.2.3 Positive mode, high depth resolution

As already mentioned, in positive mode the charge balance must take into account ejected positive secondary ions, implanted primary positive ions, and negative particles attracted to the sample: the net sum of these contribution may be equal to zero without need of auxiliary charge sources. As a consequence, it is possible to carry out SIMS measurements on lithium niobate in positive mode without electron gun. In particular, the primary beam accelerating voltage was set to 10 kV and the voltage applied to the sample was set to 4.5 kV, giving an impact energy of 5.5 keV. Under this conditions the expected depth resolution is only 4 nm, therefore this mode was particularly useful for analysis of samples with residual layer. Charge compensation did not succeed on bare LN surfaces, on the other hand it was achieved easily on samples with residual layer, indicating that the residual layer has a higher conductivity with respect to pure LN. Bare LN surfaces were therefore covered with a thin copper layer to improve electric contact with the sample holder: in such way, currents up to $5\ \mathrm{Am}^{-2}$ could be used without charging-up problems.

A.3 SIMS yields in $LiNbO_3$

The number of secondary ions counted in a SIMS experiments is proportional to the concentration of that element M in the analysed sample, through a large number of factors:

$$I_{\mathrm{M}} \propto I_{\mathrm{P}} \cdot (S \cdot \gamma \cdot \eta \cdot \beta) \cdot C_{\mathrm{M}} \tag{A.1}$$

where I_{M} is the current of secondary ions detected, I_{P} is the primary beam current, S is the sputtering yield, i.e. the number of sputtered particles per incident primary ion, γ is the ionisation efficiency, i.e. the number of secondary ions emitted with the desired charge state per sputtered atom, β is the isotopic abundance of the isotope of M which is detected, η is the transmittivity, i.e. the number of secondary ions effectively detected per secondary ion emitted, and finally C_{M} is the concentration of M in the sample. Most of these factors are difficult to be determined, moreover the sputtering yield and ionisation efficiency depend on sample composition, therefore even if all the measurement parameters are equal, SIMS yield of an element may vary from one sample to another (so called matrix effect). As a consequence, quantitative analysis is possible only after calibration. Since primary beam current and the sputtering yield can easily vary during a depth profile acquisition, the secondary ion current of an element depends also on these variations, not only on variation of concentration of that element. In order to cancel out these unwanted contributions, it is recommended to normalise the signal of the desired element to the signal of an intrinsic element whose yield is supposed to be constant.

A.3.1 Negative mode

Cs^+ is used as primary ion in SIMS because of its property of lowering the work function of the surface where it is implanted. As a consequence, negative ions have the highest yields. Metal ions do not have a strong electronegativity, therefore their yield is not so high. On the contrary, oxygen has a high probability of being emitted

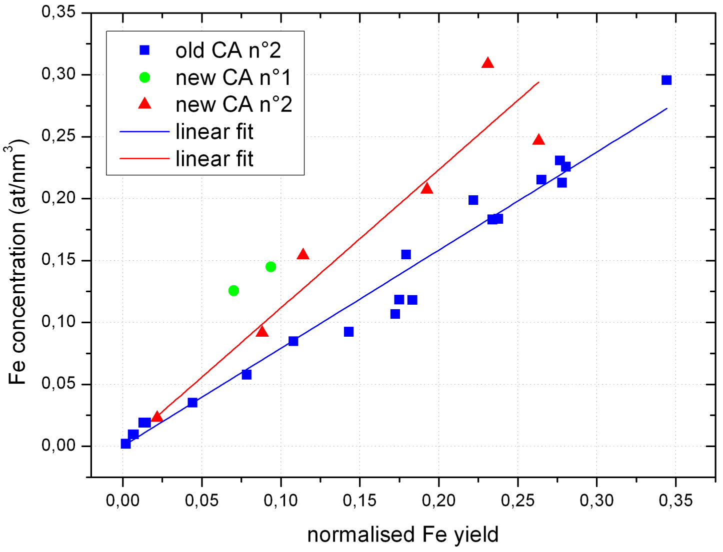

Figure A.6: Fe concentration values plotted as a function of SIMS normalised yield. Each point refers to an independent measurement. Data points can be distinguished in three sets, according to the size of contrast aperture adopted. Each data set was fitted to derive the relative sensitivity factor.

as a negative ion due to its high electronegativity. Concerning Fe:LN, Li^- and Nb^- have moderate ionisation yield, but since they are intrinsic elements the overall yield is high; O^- has a such high yield that in most of the experimental conditions here adopted the ion $^{16}O^-$ saturates the electron multiplier, therefore its less abundant isotope $^{18}O^-$ was measured; on the contrary, neither the most abundant isotope of Fe, ^{56}Fe, has a sufficient yield as negative ion. However, since oxygen is an intrinsic element and it has high electronegativity, the molecular ions LiO^-, NbO^- and FeO^- have a higher yield with respect to their corresponding simple negative ions. Therefore $^{56}Fe^{16}O^-$ ion was detected instead of $^{56}Fe^-$.

In the framework of determination of diffusion coefficient of Fe in LN, many depth profiles were measured in negative mode on similar samples (same crystallographic orientation, same chemical composition, same experimental conditions): this allows to drive statistical considerations of SIMS yields in LN. For each profile, $^{56}Fe^{16}O^-$ signal was normalised to $^{16}O^-$ in order to cancel out contribution from primary current instability, together with potential variations in $^{16}O^-$ yield. Finally the ratio of these two signals, I_M/I_{ref} describes correctly the profile of Fe. Then the integral of each profile was normalised to the fluence, known from RBS measurements, to obtain the absolute concentration profile, i.e. for each profile the proportionality factor between normalised signal and concentration was determined. This constant is usually called relative sensitivity factor RSF, defined by the equation:

$$C_M = RSF \cdot \frac{I_M}{I_{ref}} \tag{A.2}$$

In order to check the variability of RSF from one measurement to another, the concentration of Fe was plotted (figure A.6) as a function of normalised Fe signal for each measurement. Points are considerably scattered, indicating that differences in experimental conditions from one measurement to the other have a non negligible effect of RSF: this is reasonable considering the variability of beam shape, charge compensation conditions, etc. However, a clear dependence of RSF on the transmittivity of the secondary column was recognised. Contrast apertures, after many years of usage, get consumed by secondary ion collisions, thus becoming bigger and bigger: after substitution with new ones, the RSF factor became larger. Recalling that contrast aperture limits the angular acceptance of the spectrometer, this fact indicates that the yield of the reference element depends on the size of contrast aperture in a different way with respect to FeO^- yield, i.e. that the angular distribution of emitted O^- ions differs from that of FeO^- ions. Therefore in figure A.6 data points obtained with different contrast aperture size are marked in different colours. The main RSF values were determined as the slope of lines fitting two set of data points, referred to as “old CA” and “new CA”:

$$\text{old CA} \quad (7.9 \pm 0.2) \times 10^{21} \text{at/cm}^3 \tag{A.3}$$

$$\text{new CA} \quad (11.2 \pm 0.8) \times 10^{21} \text{at/cm}^3 \tag{A.4}$$

Due to the larger number of experimental points, the uncertainty on RSF for the old CA is smaller, however this value is now useless. The new value can be used for estimating the concentration with reasonable uncertainty (7%) of an unknown sample. This is particularly useful for samples with a very deep diffusion profile (more than 30µm) because it is difficult to measure the entire profile with SIMS, hence normalisation with RBS fluence is impossible: in this case the maximum concentration can be estimated from the ratio $I_\mathrm{M}/I_\mathrm{ref}$ in the first microns.

A.3.2 Positive mode

When using Cs^+ in positive mode, the highest yields are obtained for $Cs\,M^+$ ions, which get formed after interaction of implanted primary ions and intrinsic elements. Measurements of these molecular ions are particularly reliable from the point of view of relative concentrations and stoichiometry, because their yield does not depend strongly on chemical bonds between intrinsic elements. Moreover they are heavy ions, thus their yield does not depend much on instrumental settings and their energy distribution is narrow. In LN, the $CsLi^+$ ion has high yield, as a consequence of the very low ionisation energy of Li. The other molecular ions considered, namely $CsNb^+$, CsO^+ and $CsFe^+$ have moderate yields, but sufficient to obtain good profiles.

A.4 Artefacts in depth profiling

A.4.1 Primary ion implantation and surface equilibration depth

Since the SIMS yield of an element depends on the local composition of the substrate, one must take into account that the primary beam ions implant themselves into the sample, thus affecting its composition. This is the reason why Cs^+ ion is able to change the secondary ion yield. At the very beginning of sputtering, however, the first sputtered layers do not contain implanted primary ions, therefore their yield may be dramatically different from the bulk. Once the primary beam erodes layers that were already implanted, equilibrium is reached and the SIMS yields of matrix elements become constant. The depth at which equilibrium is reached is known as surface equilibration depth (SED); it depends on the mass of primary ions, their energy and

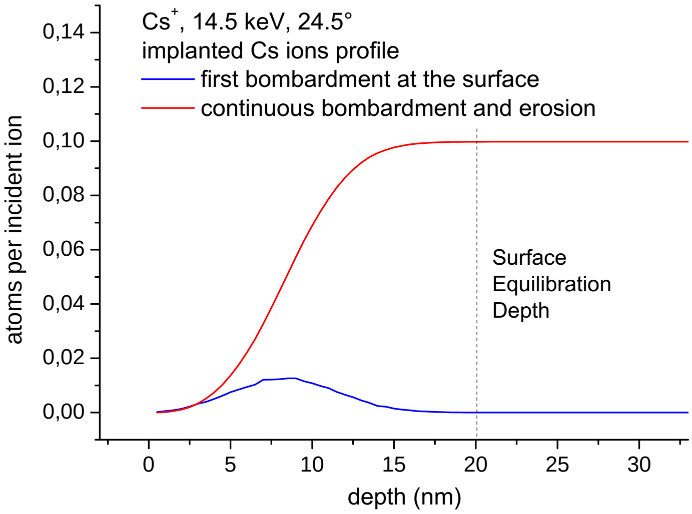

Figure A.7: Simulated implantation profile of Cs ions during SIMS measurement at 14.5 keV in $LiNbO_3$.

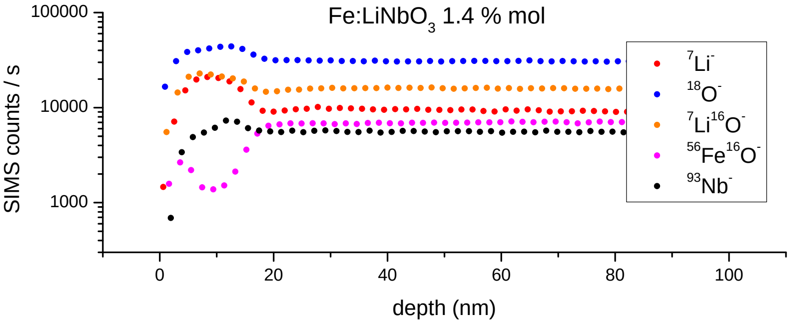

Figure A.8: SIMS depth profile of Fe doped $LiNbO_3$ with primary beam current 10 nA and energy 14.5 keV.

on the incidence angle. There exist empirical formulae relating SED to energy and incidence angle for the most used primary ions, which give SED independently of the properties of the sample. The samples analysed in this work have however different characteristics: homogeneous Fe:$LiNbO_3$ in the case of complete diffusion, Fe:$LiNbO_3$ with several nanometres of a different dielectric phase, in the case of non complete diffusion, Fe:$LiNbO_3$ with a thin metallic layer in the case of as deposited samples. To understand better the role of primary beam implantation on the SIMS yields, simple Monte Carlo simulation were made with TRIM programme. These simulation have two main limits: first, they treat the sample as an amorphous material; second, each collision cascade is calculated without taking into account the effects of former collisions. Due to these facts, simulation may underestimate depths. In the conditions that were adopted for most of the measurements in homogeneous Fe:$LiNbO_3$, i. e. 14.5 keV, simulation was done with 20000 incoming ions for each nanometre of $LiNbO_3$ eroded: the number of ions implanted during the erosion of the first nanometre was summed to the number of ions implanted during the erosion of the second nanometre and so on. Results are shown in figure A.7. The amount of implanted Cs begins to

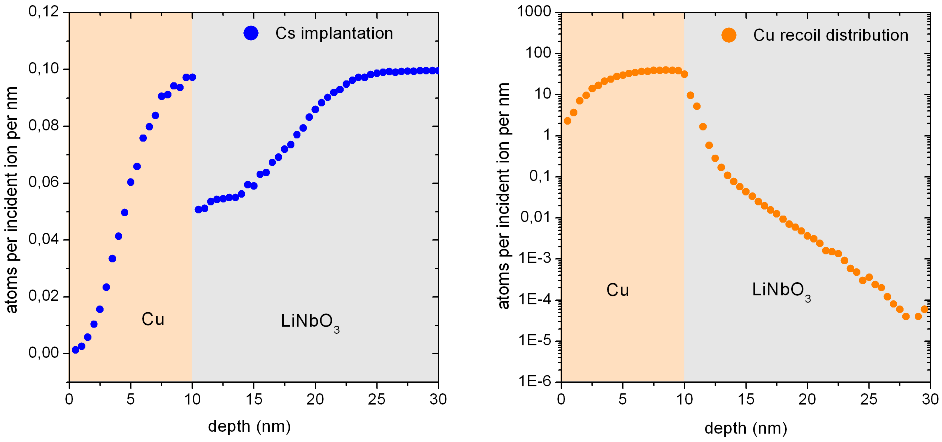

Figure A.9: Simulated profiles of Cs implanted ions and Cu recoil in a sample of $LiNbO_3$ with a copper surface layer 10 nm thick.

be constant from 20 nm in depth: this value corresponds to the end of the profile obtained from a single simulation of bombardment at the surface, as expected. The effect of SED on secondary ion yields in Fe:$LiNbO_3$ can be seen in the depth profile of figure A.8. Within the first 20 nm signals are not constant as they should be. This experimental proof confirms that simulation gave the correct value for SED. The signals for Li, Nb and O show a hump, the Fe signal instead shows a characteristic dip, the same observed for example in Si profiles in Si eroded by Cs^+ [44]. The effect of primary ion implantation on SIMS yields clearly implies that any feature in SIMS profiles that occurs within the surface equilibration depth is not reliable. This constitutes a problem when investigating compositional changes at the very first surface. A way to overcome the problem is to operate at lower and lower energy until SED becomes shallow compared to the features to be measured. Another solution is to add a layer on top of the sample, thicker than SED, in such a way that equilibrium is reached before the erosion of the original surface starts. In the case of $LiNbO_3$, it is convenient to deposit a metallic layer, so that the surface of the sample is conductive and it is possible to carry out measurement without need of electron gun for charge compensation, provided the depth to analyse is small. However the different density between metal and $LiNbO_3$ causes a discontinuity in the profile of implanted primary ions which may affect the secondary ion yields. To give an example, a simulation was made on a system consisting of 10 nm of copper deposited on $LiNbO_3$: as figure A.9 shows, the simulated profile of implanted Cs ions has a discontinuity coincident with the interface between metal and $LiNbO_3$. Moreover, simulation of recoil distribution of copper (figure A.9) reveals that some atoms are pushed into the underlying $LiNbO_3$. Therefore in the neighbourhood of a sharp interface, some instability in secondary ion yield is always expected.

A.4.2 Recoil implantation and ion mixing depth

As already hinted, atoms involved in the collision cascade displace from their original position: primary beam induced mass transport causes sharp concentration profiles to displace and broaden. As a consequence, ion mixing greatly limits the accuracy at nanometer depth resolution. A typical feature of ion mixing is that a true profile with a

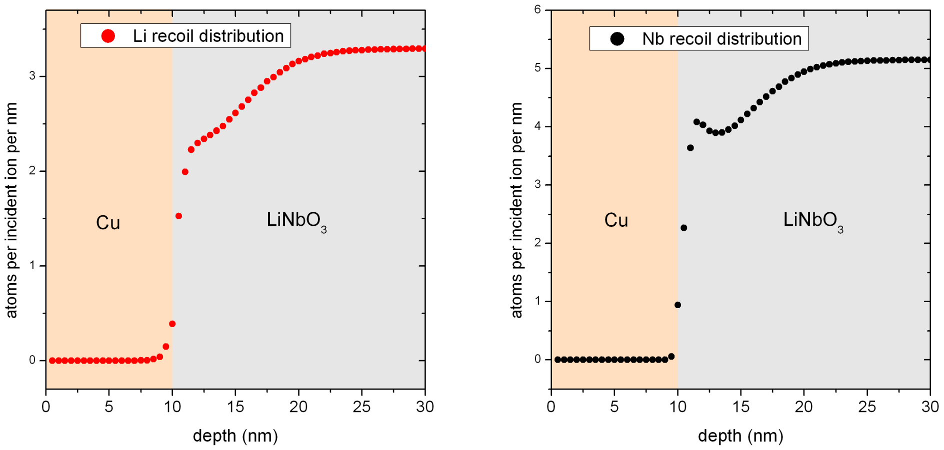

Figure A.10: Simulated profiles of Li and Nb recoil atoms in a sample of LiNbO$_3$ with a copper surface layer 10 nm thick.

sharp drop of concentration results in a smoother step with an exponentially decaying tail in the measured profile, just as the simulated Cu profile shown in figure A.9, and delta profiles result broadened towards higher depth with an exponentially decaying trend. However, true depth profiles can be derived from measured SIMS profiles using a proper deconvolution technique. Yang and Odom [45] proposed a simple algorithm suitable for delta profiles and step profiles. The measured depth profile, $N(x)$, can be expressed as a convolution of the true profile $N_0(x)$, with a SIMS response function $G(x' - x)$:

$$N(x) \int N_0(x')G(x' - x)dx'$$

Considering primary ion beam knock-on, the response function can be modeled as an exponential decay:

$$f(x' - x) = \frac{1}{\lambda} \exp - \frac{x - x' + \delta}{\lambda}$$

where λ is the decay length which can be determined directly from fitting the tail of the measured profile, and δ is the depth displacement, which can be determined if one knows a priori the step's depth. The approximated solution [45] is given by

$$N_0(x) \approx N(x + \delta) + \lambda \frac{\partial}{\partial x} N(x + \delta)$$

Of course also intrinsic elements undergo recoil implantation: in the former example of LiNbO$_3$ covered with 10 nm of copper, the simulation of ion recoil distribution of Li and Nb is shown in figure A.10. This peculiar trend of Li and Nb profiles can be recognised in figure 3.5, in the depth profile obtained at 5.5 keV on sample treated at 600 °C. It is therefore expected that after erosion of the copper layer, the secondary ion signals of all species will not be constant over a depth again equal to SED.

A.4.3 Artefacts in experimental depth profiles

Many samples were covered with about 15 nm of copper via magnetron sputtering deposition, in order to improve charge compensation: the artificial tail, simulated by

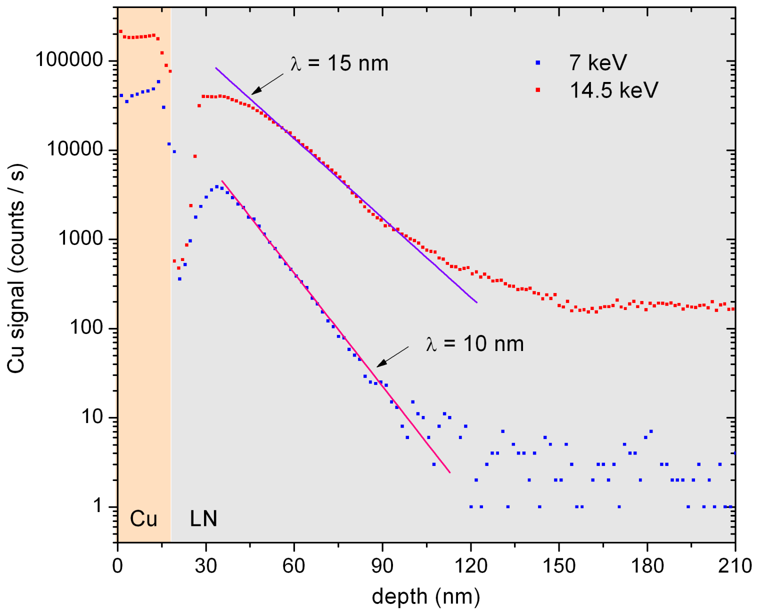

Figure A.11: Comparison of Cu depth profiles acquired on LN sample covered with a Cu thin film, with two different primary beam energies: the two decay length were obtained by fitting the exponential tails of Cu signals.

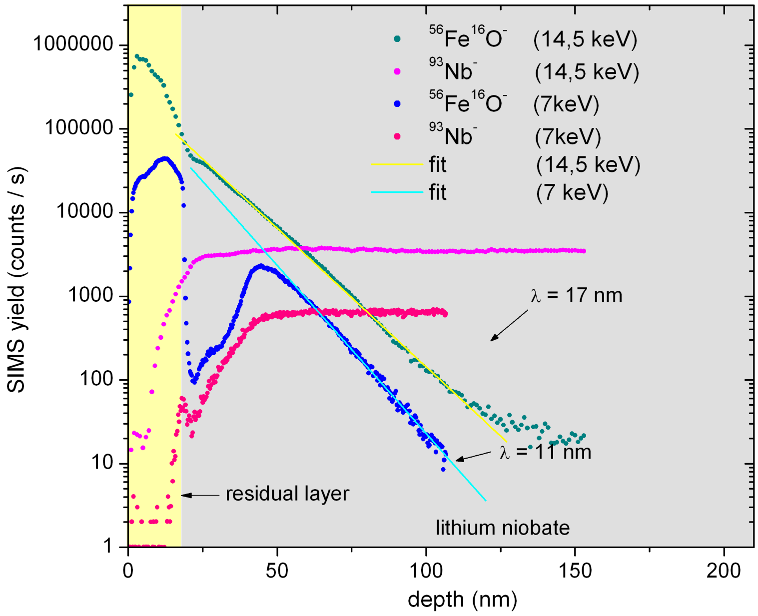

Figure A.12: Comparison of Fe and Nb signals acquired on a Fe:LN annealed at 600 °C, with two different primary beam energies: the two decay length were obtained by fitting the exponential tails of Fe signals.

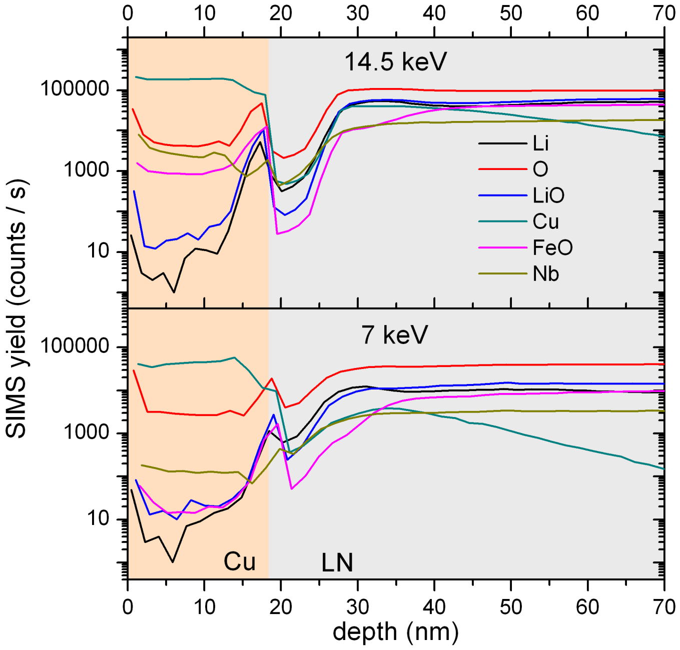

Figure A.13: Depth profile of a LN sample covered with a Cu thin film, obtained with primary beam energy 14.5 keV and 7 keV: after erosion of Cu film, all the signal drops; this effect is less pronounced for lower energy.

TRIM (figure A.9, in the Cu depth profile was experimentally observed. By way of example, the same sample was measured in negative mode at 14.5 keV and 7 keV and the Cu depth profile is shown in figure A.11: as expected, the profile exhibits an exponentially decaying tail that extends deeply in the substrate. The tail decays at longer depth for the profile obtained with higher primary beam energy: this proves that the tail is an artefact and does not represent a true concentration trend. Part of the tail has been fitted to derive experimentally the decay length: the results are 15 nm in the case of 14.5 keV primary beam, and10 nm in the case of 7 keV primary beam.

It is interesting to discuss the exponential tail of the first sample of the set of samples treated at different temperatures with residual layer, i.e. the sample treated at 600 °C for 1 h. It was measured both at 7 keV and at 14.5 keV. By comparing the two Fe depth profiles, it stands out that the profile obtained at 7 keV is significantly narrower than the other: this indicates again that the measured profile does not correspond to the true one. Indeed these two profiles, after the residual layer erosion, have an exponentially decaying trend: the decay lengths, derived from fitting of the exponential tails, are comparable to those derived for Cu. It can be concluded that the tails are due *only* to recoil implantation, i.e. that Fe atoms did not diffuse at all into the substrate, instead they were still staying in the residual layer even after 1 h at 600 °C. The decay lengths are slightly higher than those for Cu because Cu is heavier than Fe.

Concerning the samples covered with copper film again, the signals of all the ions detected show a peculiar behaviour in the first tens of nanometres. Looking at figure

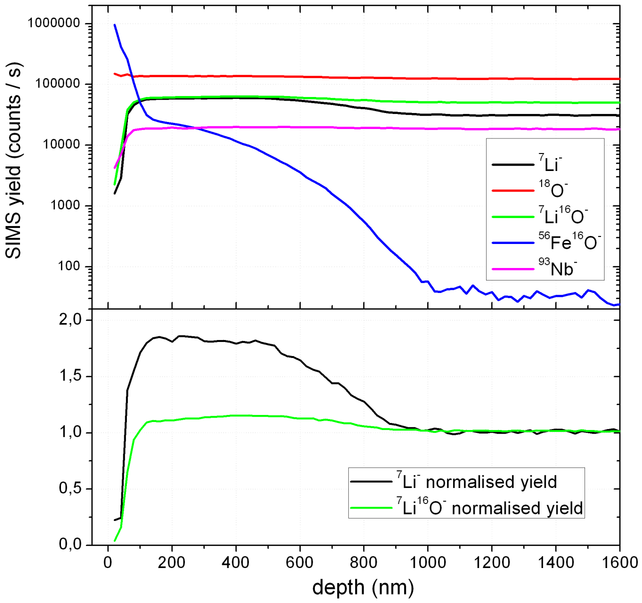

Figure A.14: Depth profile of a Fe:LN sample with residual layer, where an enhancement of Li signals is evident in the first 600 nm; the normalised signals reveal that the relative enhancement is different for Li^- ion and for LiO^- ion.

A.13, during the erosion of the copper film, the signal of Cu is very intense, the other signals are less intense than in the substrate, however not negligible as expected. When the Cu film is almost completely eroded, the other signals begin to grow, but then the yield of all ions suddenly drops; after erosion of some nanometres signals grow again up to their steady values in the bulk. This dip, drawn by all signals, clearly depends on primary beam energy, indeed it is more pronounced for measurement at 14.5 keV with respect to 7 keV. It can be concluded that the dip is due to the discontinuity in the density of Cs implanted ions: after erosion of the copper film, the first layer of substrate contains less Cs ions than the remaining substrate underneath, as the simulation demonstrated (figure A.9), thus the secondary ion yields are lower. The width of the dip obtained at 14.5 keV is about 10 nm, consistent with the width of the depleted layer in the simulated profile. However, concerning samples with residual layer, the only one that showed the dip after erosion of the residual layer is the one treated at 600 °C, i.e. the same one in which Fe did not diffuse at all in the substrates and whose diffraction peak was much broader than others. In the SIMS profiles of all the other samples there is no discontinuity of signals from residual layer to substrate. These facts suggest that in the sample treated at 600 °C there is an abrupt, incoherent interface between two crystalline phases, which stops the trajectories of primary ions and gives rise to a marked discontinuity in the profile of Cs implanted ions. In the other samples with residual layer, interdiffusion between the two phases occurred, the residual layer has a better crystalline order and probably it became pseudomorphous to the substrate, thus there is no more discontinuity in the profile of Cs implanted ions.

Samples with residual layer displayed also anomalies in the depth profiles of Li. An example is shown in figure A.14: as long as Fe is present, the Li^- signal draws a hump; all the depth profiles of samples with the residual layer showed, more or less, the same feature. It is probably an artefact, because if it was due to a true higher concentration of Li, the LiO^- signal would have the same hump as well. On the contrary, if the two signals, normalised to a reference element (oxygen) are compared, the relative enhancement of signal in the hump region with respect to the deep region differs much: up to 115% for Li^- signal, up to 190% for LiO^- signal. Moreover, the humps disappeared if the measurement was carried out after consumption or removal of the residual layer, confirming that it is an artefact, clearly related to the presence of the residual layer on the crater's edges. The reason of this phenomenon was not recognised yet.

A.5 Scanning ion images

As already mentioned, there is a dynamic transfer system that deflects the secondary ion beam synchronously with the primary beam deflection. An electronic system associates the intensity detected at a certain instant to the point from which those ions were emitted, taking into account the mass-dependent time of flight from the sample to the detector. The system creates an image on a cathode ray tube with size 256 × 256 pixels: each image point on CRT of the scanning ion image corresponds in position and intensity to an object source point. The corresponding size of the surface depends on the raster size of the primary beam, which can be set up to 500×500 μm^2. Thus secondary ion images are obtained.

In "microprobe" mode the beam size is made very small, and large contrast aperture and field aperture are chosen in order to increase the transmittivity: in these conditions the lateral resolution of the ion image depends on the size of the primary beam and on the aberrations of the transfer system. In "microscope" mode, a small contrast aperture is chosen to reduce aberrations, and also a small field aperture to limit the area from which secondary ions are collected for each image point: the lateral resolution of the image is therefore determined by the transfer optical system. In this case the smallness of the primary beam size is not fundamental. In this mode the transmittivity of the spectrometer is low, hence to improve the secondary ion yield it is convenient to increase the primary beam current. More precisely, the primary current *density* should be maximised over an area equivalent to the lateral resolution, and the beam position must be finely centred on the optical axis of the transfer system on the sample, in order to get the highest secondary ion yield for a given primary beam current, i.e. for a given amount of material eroded.

Data acquisition consists in counting secondary ions and attribute each count to a point of the 256 × 256 pixels image. A cycle that covers the whole surface lasts 0.56 seconds and generates one image plane, corresponding to a depth determined by the sputtering rate. By eroding for many cycles, many image planes are acquired, each corresponding to a certain depth in the sample: thus 3D imaging is possible. If the secondary ion yield is low, it is possible to accumulate more than one cycle for each image plane, thus worsening the depth resolution of the 3D image. Secondary ion images were used to characterise the results of laterally confined local doping. Measurements were carried out in negative mode at 14.5 keV without electron gun, after deposition of a thin Cu layer on the samples. The lateral resolution was determined a posteriori on a test sample with sharp lateral distribution of elements.

Appendix B

UV-vis spectrophotometry

For optical absorption measurements, a Jasco V-670 spectrometer was used. It is a double beam spectrophotometer operating in a wide range of wavelengths from 200 to 3200 nm. It is equipped with two lamps (deuterium lamp from 190 to 350 nm, halogen lamp from 330 to 3200 nm), a dual-grating monochromator, two detectors (a photomultiplier tube and a Peltier-cooled PbS detector) It is equipped also with an optional rotating sampleholder, and an optional polarising window made of a Glan-Taylor calcite prism.

A scheme of the spectrometer is drawn in figure B.1: light produced by lamps is first monochromatised by the grating, the splitted in two branches, the “reference” branch and the “sample” branch. Usually the “reference” branch is kept empty or a blank sample is put in it. The two beams are alternatively sent to the detector thanks to a moving mirror. The double beam configuration allows to cancel out fluctuations due to instability of lamps or detectors. Ideally, the two branches should be equal, each one carrying 50% of the incoming intensity. However they are not equal because the optical paths are slightly different. Moreover, when a polariser is mounted in the “sample” branch, the intensity detected in this branch is lower than the other. Therefore the ratio between “sample” and “reference” signal takes into account not only the absorption of the sample but also the difference between the two branches. In order to correct this, a baseline measurement is needed, i.e. a measurement acquired in the same conditions, but with the “sample” branch empty. The subsequent spectrum acquired with the sample is automatically divided by the baseline. The resulting spectrum should finally be representative of the absorption of the sample without artifacts. Nevertheless, small artifacts are still present due to non-linearity of the detectors. There are spectral regions where the detected intensity is high, due to high intensity emitted by the source or to high response of the detector: if in these regions the intensity is much different between “sample” and “reference” branch, the non-linearity gives rise to small dips or humps in the normalised spectrum.

Since LN is birefringent, dealing with X-cut LN samples implies that if unpolarised light is used, it propagates both with extraordinary and ordinary refractive index. To avoid this complication, polarised light was used and for each sample two spectra were acquired, one with light polarised along Z direction (extraordinary refractive index) and the other with light polarised along Y direction (ordinary refractive index).

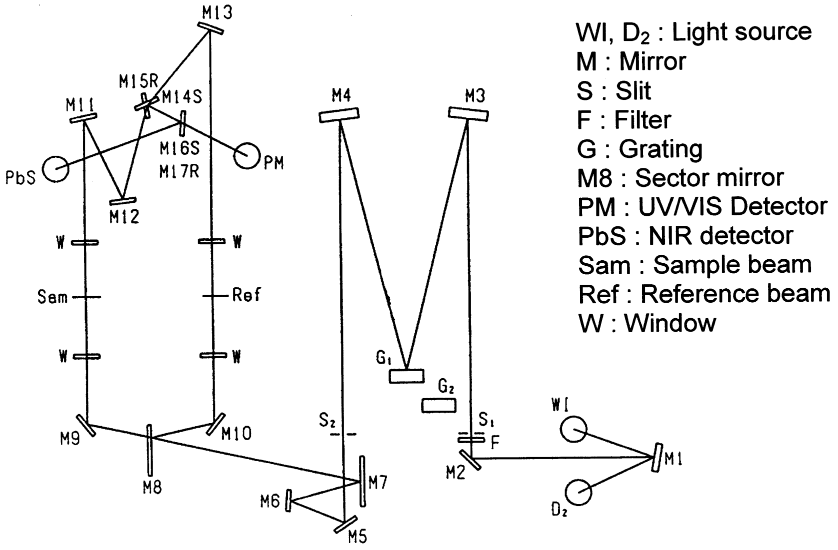

Figure B.1: Scheme of the optics of Jasco V-670 spectrophotometer.

B.1 Spectra correction

In order to extract from these measurements quantitative information about the absorption properties of the material, it is fundamental to remove spurious effects and perform a correct data analysis. Since lithium niobate has a high refractive index, surface reflectivity is quite significant. Moreover, also the polariser and the exit window reflect a non negligible fraction of intensity which comes back to the sample. It is necessary to take into account all these effects to extract from data the absorption coefficient α. Figure B.2 shows a scheme of the chamber: light emitted by sources with intensity I_0, after monochromatisation, pass through polariser first, then through the sample, then through quartz exit window, as shown in the upper part of the figure. As a result of multiple reflections and transmissions, many rays are produced, the most important are traced in the figure (polariser, sample and window are drawn tilted, in order to distinguish the trajectories). When the baseline is acquired, light is reflected and transmitted only between polariser and exit window (lower part of the figure) It is easily recognisable that the intensity transmitted consist of many contribution, which in the case of normal incidence are detected altogether. First, the Fresnel coefficients for reflection and transmission at normal incidence are called r_p, τ_p, r_s, τ_s r_q, τ_q, for respectively polarizer, sample, quartz glass exit window. Coefficients r and τ satisfy the relations

$$r = \left(\frac{n_a - n_{\text{mat}}}{n_a + n_{\text{mat}}}\right)^2 \qquad \tau = \frac{4n_a n_{\text{mat}}}{(n_a + n_{\text{mat}})^2} \qquad r + \tau = 1 \tag{B.1}$$

where n_a is the refractive index of air, n_{mat} is the refractive index of the material considered (calcite, lithium niobate, quartz glass) The intensity measured for baseline consists of these contributions:

$$I^{\text{baseline}} = I_0\tau_p^2\tau_q^2 + I_0\tau_p^2 r_q r_p \tau_q^2 + I_0\tau_p^2 r_q^2 r_p^2 \tau_q^2 + \dots \tag{B.2}$$

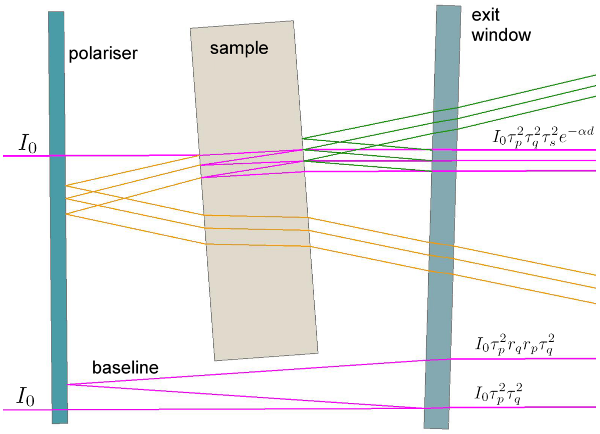

Figure B.2: Scheme of reflected and transmitted rays between polariser, exit window and sample in the chamber of the spectrophotometer.

which can be rewritten in terms of a geometric series

$$I^{\text{baseline}} = I_0 \tau_p^2 \tau_q^2 \sum_{n=0}^{\infty} (r_q r_p)^n \tag{B.3}$$

substituting for the sum of the geometric series with argument < 1

$$I^{\text{baseline}} = I_0 \frac{\tau_p^2 \tau_q^2}{1 - r_p r_q} \tag{B.4}$$

The intensity measured with the sample consists of several kinds of contributions:

$$\begin{aligned} I^{\text{sample}} = I_0 \tau_p^2 \tau_q^2 \tau_s^2 e^{-\alpha d} \cdot [1 &+ r_s^2 e^{-2\alpha d} + r_s^4 e^{-4\alpha d} + \cdots \\ &+ r_s r_p + r_s^2 r_p^2 + \cdots \\ &+ r_s r_p \tau_s^2 e^{-\alpha d} + r_s r_p \tau_s^2 e^{-\alpha d} r_s^2 e^{-2\alpha d} + \cdots \\ &+ r_s r_q + r_s^2 r_q^2 + \cdots \\ &+ r_s r_q \tau_s^2 e^{-\alpha d} + r_s r_q \tau_s^2 e^{-\alpha d} r_s^2 e^{-2\alpha d} + \cdots] \end{aligned} \tag{B.5}$$

where d is the light path inside the sample (equal to the sample thickness for normal incidence). All these contributions can be easily rewritten as a product of three series:

$$\begin{aligned} I^{\text{sample}} &= I_0 \tau_p^2 \tau_q^2 \tau_s^2 e^{-\alpha d} \sum_{n=0}^{\infty} r_s^2 e^{-2\alpha d} \sum_{n=0}^{\infty} (r_p r_s)^n \sum_{n=0}^{\infty} (r_q r_s)^n \\ &= \frac{I_0 \tau_p^2 \tau_q^2 \tau_s^2 e^{-\alpha d}}{(1 - r_s^2 e^{-2\alpha d})(1 - r_p r_s)(1 - r_q r_s)} \end{aligned} \tag{B.6}$$

Finally, the transmittance measured by the instrument is given by:

$$T = \frac{I^{\text{sample}}}{I^{\text{baseline}}} = \frac{\tau_s^2 e^{-\alpha d}}{1 - r_s^2 e^{-2\alpha d}} \cdot \frac{1 - r_p r_q}{(1 - r_p r_s)(1 - r_q r_s)} \tag{B.7}$$

where the factor

$$F_r = \frac{1 - r_p r_q}{(1 - r_p r_s)(1 - r_q r_s)} \tag{B.8}$$

depends only on reflection coefficients of the surfaces. It is convenient to define a corrected transmittance $T' = T/F_r$, then after rearranging a second degree equation is obtained:

$$e^{-2\alpha d} + \frac{\tau_s^2}{T' r_s^2} e^{-\alpha d} - \frac{1}{r_s^2} = 0 \tag{B.9}$$

which can be solved to find out the attenuation factor $e^{-\alpha d}$

$$e^{-\alpha d} = -\frac{\tau_s^2}{T' r_s^2} + \sqrt{\left(\frac{\tau_s^2}{T' r_s^2}\right)^2 + \frac{1}{r_s^2}} \tag{B.10}$$

This relation allows to calculate the absorption coefficient starting from transmittance values. To perform calculation, refractive indexes at all wavelengths are needed, to find out reflection and transmission coefficients.

B.2 Procedure

Samples are cleaned with acetone, then mounted on the rotating sample holder. Polariser is mounted on the entrance window in the “sample” branch.

Optimisation involved the wavelength at which the instrument changes diffraction grating and detector: since the two detectors give different response, the wavelength was chosen in order to minimise the step in the signal spectrum. Optimisation involved also the choice of the spectral bandwidth, which is linked to the size of the beam, since bandwidth is determined, given the wavelength spread of the grating, by the slits aperture. The bandwidth choice must take into account that the two grating give different wavelength spread, therefore the same bandwidth result in two different sizes of the beam in the two spectral regions. To have the same size in the entire spectrum, IR bandwidth must be four times the UV-vis bandwidth. Little bandwidth implies low intensity: the best choice is a compromise between resolution requirement and signal to noise ratio. Optimisation involved also scanning speed, detection duration at each step, data pitch. After optimisation, spectra were taken in the following experimental conditions: reference and sample branch are kept empty for the baseline measurement and the sample is placed in the sample branch for the subsequent sample measurement. The chosen measurement parameters are:

- photometric mode: transmittance percent (the signal in sample branch divided by the signal in reference branch);
- response: slow;
- scanning speed: 100 nm/min;
- spectral range: from 300 nm to 1600 nm(the upper limit is due to absorption by the polariser);
- bandwidth: 1 nm in UV-vis region, 4 nm in infrared region;
- data pitch: 1 nm;
- source change wavelength: 340 nm;
- grating and detector change wavelength: 800 nm;

B.3 Data analysis

The data treatment described above showed to be not suitable to our experimental conditions. The most accounted reason is that light is not collimated, instead it is focused on sample position. The incidence angle spreads over a certain range, and so do the reflected and transmitted rays, part of which may be not detected because it falls out of exit window. It is therefore difficult to find out a good way to correct our spectra. This means that it is impossible to find out the absolute absorption coefficient. It was decided then to perform a simple normalisation of spectra with respect to an undoped commercial sample. That is, for each sample to measure, a spectrum of the sample and a spectrum of pure LN were taken exactly in the same conditions, and the latter was used as a baseline. This procedure is justified by two considerations: first, the thickness of pure sample and doped sample is always the same, this ensures that there is no difference in optical path; second, the refractive index, as found in literature [39], differs very little from Fe-doped to undoped LN, therefore the percentage of light intensity transmitted or reflected by interfaces is almost equal in the two cases. In terms of the equations written above, this procedure implies the following approximation:

$$\frac{T^{\text{doped}}}{T^{\text{undoped}}} = \frac{\tau^2_{\text{doped}} e^{-\alpha_{\text{doped}} d}}{\tau^2_{\text{undoped}} e^{-\alpha_{\text{undoped}} d}} \cdot \frac{1 - r^2_{\text{undoped}} e^{-2\alpha_{\text{undoped}} d}}{1 - r^2_{\text{doped}} e^{-2\alpha_{\text{doped}} d}} \approx \frac{e^{-\alpha_{\text{doped}} d}}{e^{-\alpha_{\text{undoped}} d}} \tag{B.11}$$

which is justified in most cases, since $r^2 < 0.02$ and $e^{-\alpha d} < 1$. This procedure has another advantage: it allows to isolate only the contribution of the dopant to absorption properties, because not the absolute absorption coefficient, but rather the difference $\alpha^{\text{doped}} - \alpha^{\text{undoped}}$ is derived. From normalised spectra, optical density $OD = -\ln \frac{T^{\text{doped}}}{T^{\text{undoped}}}$ was calculated. In the case of bulk FeLN samples, it was divided by the thickness to obtain the absorption coefficient. In the case of diffused FeLN, since the responsible of absorption is not homogeneously distributed over the sample thickness, it makes no sense to calculate absorption coefficient, so the optical density itself was used to develop the discussion in section 4.1.

Appendix C

Ion beam analysis

Rutherford backscattering technique (RBS) was used to quantify the absolute amount of iron deposited. The knowledge of the dose of iron, together with the knowledge of thickness by XRR, allows to determine the density of the film before the diffusion; moreover, assuming that Fe does not evaporate during diffusion[1], allows to convert the SIMS depth profile after diffusion into concentration profile, as shown in chapter 3.

C.1 Rutherford Backscattering Spectrometry

During an RBS measurement, few MeVlight ions are made to collide on the sample surface. Incident ions undergo collisions with target atoms and are therefore scattered. Backscattered atoms are collected by a detector which measures their energy: the reduction in energy depends on the masses of incident and target atoms and provides the signature of the target atoms [46].

Kinematics of elastic collision can be solved by applying the principles of energy and momentum conservation. The energy of the scattered atom satisfies the relation

$$\frac{E_1}{E_2} = \left[\frac{(M_2^2 - M_1^2 \sin^2\theta)^{\frac{1}{2}} + M_1 \cos\theta}{M_2 + M_1}\right]^2 = K(M_1, M_2, \theta) \tag{C.1}$$

where M_1, M_2 are the masses of projectile ion and target atom respectively, and E_1, E_2 are projectile ion energies before and after collision, as shown in figure C.1, and K is called kinematic factor and depends only on masses and scattering angle θ. The identity of target atoms is determined by the energy of the scattered particle, therefore, given the experimental geometry and the incident ion, the backscattering (θ as close as possible to 180°) geometry is preferred because of higher change of K as a function of target mass.

The number N_s of target atoms per unit area is determined by the probability of a collision between incident particle and target atoms as measured by the total number of detected particles Q_D for a given number Q of incident particles. The connection between number of target atoms per unit area N_s and number of detected particles is

---

[1] This was confirmed by PIXE quantitative measurements of Fe amount on an as-deposited sample and an as-diffused sample, which gave consistent values.

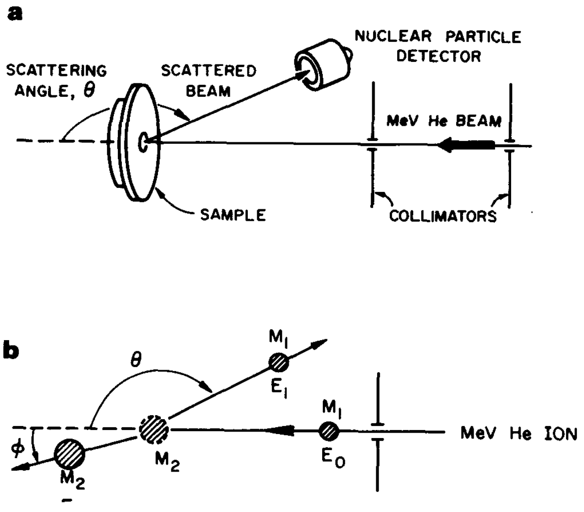

Figure C.1: Scheme of experimental setup for RBS measurement (a); schematic representation of elastic collision between incident ion and target atom (b) [46].

given by the scattering cross section:

$$\frac{\text{number of particles scattered into } d\Omega}{\text{total number of incident particles}} = \frac{d\sigma(\theta)}{d\Omega} \cdot d\Omega \cdot N_s \tag{C.2}$$

If the detection solid angle Ω is small, one can define an average differential cross section

$$\sigma(\theta) = \frac{1}{\Omega} \int_{\Omega} \frac{d\sigma}{d\Omega} \cdot d\Omega \tag{C.3}$$

therefore the number of detected particles is given by:

$$Q_D = \sigma(\theta) \cdot \Omega \cdot Q \cdot N_s \tag{C.4}$$

The scattering cross section can be calculated from the force that acts during the collision between projectile and target atom. Since high energies are used, the distance of closest approach is within electron orbit, so the force can be described simply as a Coulomb repulsion of two nuclei, with a small correction due to electron screening.

C.2 Fe fluence measurements

The experiments were performed on a set of seven as-deposited samples with different deposition duration, using the 1.7 MV tandetron 4117HC accelerator at IMM-CNR (Bologna) which provided a He^+ collimated beam (energy 1.5 MeV). The detector was placed at 170° with respect to the incident beam, with a detection solid angle (measured with calibration standard) equal to 1.966 mstrad. Since Nb is heavier, Fe signal will be superimposed to a high background signal due to Nb of the substrate. RBS spectra were therefore acquired in channeling condition with X axis, i.e. with the incident beam perpendicular to the surface of the sample, in order to reduce Nb background signal and isolate easily Fe peak. In figure C.2 two RBS spectra in

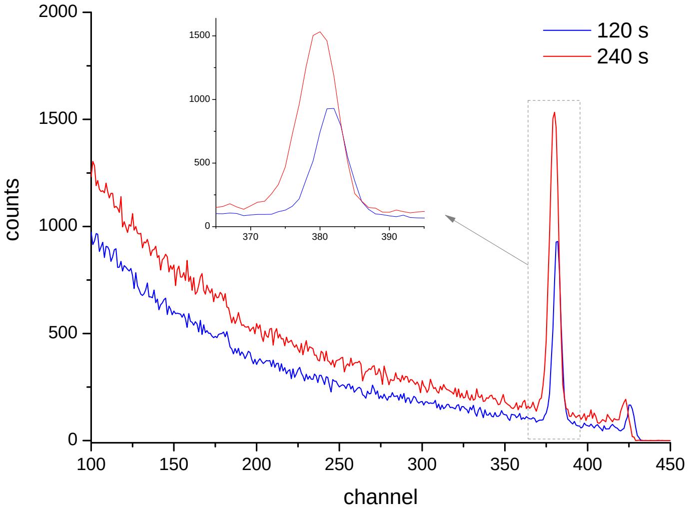

Figure C.2: RBS spectra in channeling condition of two as-deposited samples of Fe on $LiNbO_3$. Abscissa reports the channel number, each channel detecting an energy range of backscattered particles. The inset shows an enlargement of the spectrum.

channeling condition with X axis are reported. The Fe peak is clearly distinguishable from the background signal due to Nb backscattering, which rises going from higher to lower energies. Since Fe atoms are located in a very thin layer on the surface, they give rise to a narrow peak whose width depends only on the energy resolution of the detector. By means of the Rutherford cross-section, the solid angle of detector acceptance, the Fe screening factor, and the incident ion charge, it is possible to relate linearly the integral area of the Fe peak to the fluence, the proportionality factor being equal to

$$k = \frac{1}{19.018} \times 10^{15} \frac{\text{atoms}}{\text{cm}^2} \frac{\mu\text{C}}{\text{counts}}$$

This factor was used to derive all the fluence values reported in table 2.1.

Appendix D

X-Rays methods

In this appendix the techniques involving X-rays exploited in this work are briefly described.

D.1 High resolution X-rays diffraction

X-rays diffraction involves probing a crystal with X-ray radiation having a wavelength λ close to the crystal lattice spacing. X-rays are scattered by the electron cloud surrounding each atom in the crystal. Constructive interference occurs between the scattered X-rays whenever Bragg's law is satisfied:

$$n\lambda = 2d \sin\theta$$

which relates the spacing between lattice planes d to the angle at which the incident monochromatic beam probes the planes. Experimentally the angle 2θ is measured. Each set of crystal planes produces diffraction spots, whose position, shape and intensity are related to the characteristics of a given plane family. The scattering process in a crystal can be described by associating to each plane family a vector, normal to the planes and having a length of $1/d$ where d is the interplanar spacing. The endpoints of such vectors originate a lattice in the reciprocal space, called reciprocal lattice. If the incident ($\vec{k_0}$) and diffracted ($\vec{k_h}$) beam vectors make appropriate angles with respect to the crystal, the scattering vector $\vec{S} = \vec{k_h} - \vec{k_0}$ will end at a reciprocal lattice point, as shown in figure D.1: its length can be altered by changing the angle 2θ, whereas its direction is scanned by changing ω, the angle at which the incident beam meets the sample surface. Not all reciprocal lattice points can be accessed: the large circle shows the outer limit which can be reached with S for a given λ and maximum θ. In practise, diffraction spots are broadened in reciprocal space by microstructural defects, instrumental resolution, and the macroscopic size and shape of the sample.

D.1.1 Experimental

Reciprocal space can be investigated by rotating the detector and the sample in a diffractometer. It this work, a four-circle high-resolution diffractometer (PANalytical X'Pert PRO MRD) was employed. A scheme is shown in figure D.2. The X-ray source, a Cu anode sealed tube, generates X-rays at the wavelength of $\mathrm{K}_{\alpha_{II}}$ line of Cu (1.54056 Å) with relative bandwidth $\Delta\lambda/\lambda = 10^{-4}$. The beam has a large angular

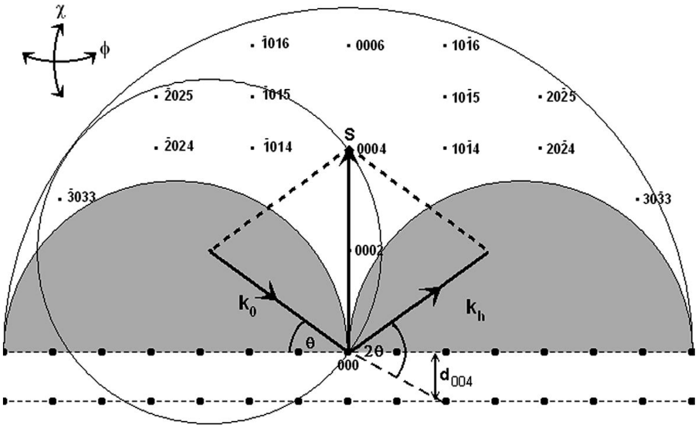

Figure D.1: Section of reciprocal space of a generic crystal. Inaccessible regions, where the sample blocks the beam, are shown in grey. Incident vector, diffracted vector and scattering vector are indicated. The circle represents a section of the Ewald sphere, whose radius is the incident vector's modulus.

divergence and a spectral purity not sufficiently low for high resolution. To convert the divergent beam to a nearly parallel beam a parabolic bent graded multilayer mirror is used, reducing the angular divergence to 0.03°. In order to further improve angular divergence and spectral purity a Bartels four-crystal monochromator is positioned after the mirror: this element consists of two channel-cut germanium crystals, in which the incident beam is diffracted four times by (2 2 0) planes of germanium. The resulting spectral purity is $\Delta\lambda/\lambda = 10^{-5}$ and the angular divergence is 0.0039°. If no other elements are added to this instrument, apart from a Xe gas proportional detector, the so-called *double axis* configuration is obtained: in this configuration the detector is operated with an angular acceptance of 1°. To obtain higher resolution, the acceptance can be reduced putting slits in front of the detector up to 1/32°, and adding an analyser crystal, similar to Bartels monochromator, which reduces the angular acceptance to 0.0039°. This high resolution configuration is called *triple axis*. The angular movements of goniometers are controlled by high precision motors and the reproducibility in the angular positioning is estimated to be better than 0.0002°. The whole system is placed in a temperature controlled housing, keeping the temperature in the measure chamber at (25.0 ± 0.1) °C.

The sample axes of rotation are shown in figure D.2. $\omega - 2\theta$ or $2\theta - \omega$ scans probe the diffraction spot along a direction that generally has less broadening, required for lattice parameter determination: the sample is rotated by ω and the detector is rotated by 2θ with ratio 1:2; in reciprocal space, S moves outwards from the origin, its length changes but its direction remains the same. Both types of scans are called *rocking curves*, as they involve rocking the sample about the ω axis. Much information regarding interplanar spacings and defect-related broadening can be summarised in *reciprocal lattice maps*, which show a 2D section through reciprocal space. They can be obtained by taking a series of $\omega - 2\theta$ scans at successive ω values, or viceversa, and presenting the results in map form, where angles are converted into reciprocal lattice coordinates $\mathring{A}^{-1}$.

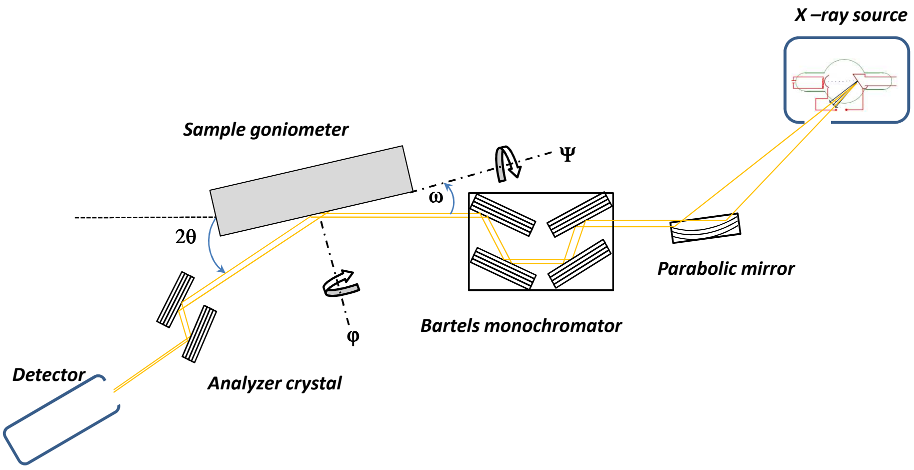

Figure D.2: Scheme of X-rays diffractometer.

D.1.2 Lattice parameter measurement

Lattice parameter measurements provide information on the strain and stress, doping levels, composition and thermal expansion of the films. Relative measurements involve finding the separation of a layer peak from a substrate peak from one or more scans, giving the relative relaxation and/or mismatch.

D.1.3 Reciprocal lattice maps

Many factors may cause broadening of reciprocal lattice spots: reciprocal lattice maps give a two-dimensional representation of broadening that can occur in all three dimensions. The features visible in reciprocal lattice maps may give indications on the crystal structure. In particular, vertical broadening is related to small layer thickness, or small vertical width of coherently diffracting domains. Variations in interplanar spacing due to strain or compositional gradient along the surface normal cause the vertical broadening of reciprocal lattice points. Horizontal broadening is related to small lateral width of coherently diffracting domains, or their misorientation, as well as the presence of lateral strain. Diffuse scattering arises directly from defects.

D.2 X-rays Reflectivity

For measuring the thickness of the iron thin films deposited, the X-ray reflectivity (XRR) technique was used. This non-destructive technique is based upon interference between electromagnetic waves reflected by the film surface and the film-substrate interface. X-rays are suitable for nanometric thicknesses.

The technique consists in sending an X-ray beam on the sample surface in grazing incidence condition, and measuring the X-ray intensity reflected by the sample as a function of the incidence/reflection angle. As the X-ray refractive index is generally less than one, total external reflection occurs below a certain (very small) critical angle θ_c. Above this angle, the beam begins to penetrate the sample and the reflected

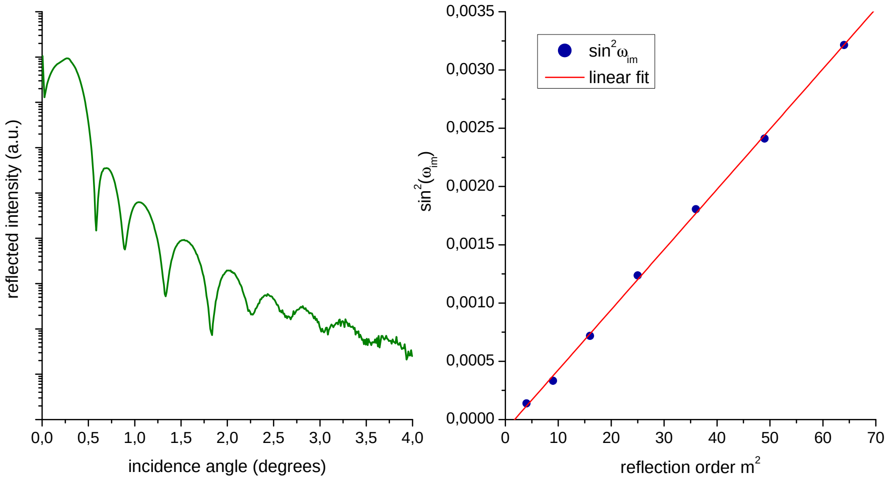

Figure D.3: XRR spectrum from a 10 nm thick Fe layer (a) and plot of values of square sin of angles of maximum reflection against square order of reflection, fitted with a line (b).

intensity drops off with a $1/\theta_i^4$ dependence. If the sample has a thin surface layer, or multilayer, fringes are superimposed to this region, due to differences in electron density, easily understood by analogy to conventional optics. Applying Snell's law and Fresnel's law, constructive interference occurs when:

$$\frac{m^2\lambda^2}{4t^2} = \sin^2\theta_1 - \sin^2\theta_c \tag{D.1}$$

Considering successive maxima i and $i+1$, of order m_i and m_{i+1} (the order is often unknown) and eliminating the critical angle:

$$\frac{(2m_i+1)\lambda^2}{4t^2} = \sin^2\theta_{i+1} - \sin^2\theta_i \tag{D.2}$$

thus a plot of $\sin^2\theta_{i+1} - \sin^2\theta_i$ against m_i has a gradient of $\lambda^2/4t^2$ and gives an accurate measure of thickness of the surface layer. An example of $\theta - 2\theta$ reflectivity scan of a Fe layer on LN is shown in figure D.3, together with data analysis for deriving the thickness of the layer, according to equation D.1. All the thickness data reported in section 2.2.2 have been calculated using this method.

Bibliography

[1] P Günter and J. P. Huignard. *Photorefractive Materials and Their Applications 1*. Springer Science - Business Media, Inc., 2006.

[2] D. Kip. Photorefractive waveguides in oxide crystals: fabrication, properties, and applications. *Appl. Phys. B*, 67:131–150, 1998.

[3] T. Volk and M. Whölecke. *Lithium niobate. Defects, photorefraction and ferroelectric switching*. Springer series in Material Science. Springer, 2008.

[4] F. Abdi, M. D. Fontana, M. Aillerie, and P. Bourson. Coexistence of Li and Nb vacancies in the defect structure of pure $LiNbO_3$ and its relationship to optical properties. *Appl. Phys. A*, 83:427–434, 2006.

[5] O. F. Schirmer, M. Imlau, C. Merschjann, and B. Schoke. Electron small polarons and bipolarons in $LiNbO_3$. *J. Phys. Condens. Matter*, 21:123201, 2009.

[6] L. Kovács, G. Ruschhaupt, K. Polgár, G. Corradi, and M. Wöhlecke. Composition dependence of the ultraviolet absorption edge in lithium niobate. *Appl. Phys. Lett.*, 70:2801–2803, 1997.

[7] J. Frejlich. *Photorefractive Materials*. Wiley Interscience, 2007.

[8] J. Carnicero, M. Carrascosa, G. García, and F. Agulló-López. Site correlation effects in the dynamics of iron impurities Fe^{2+}, Fe^{3+} and antisite defects Nb_{Li}^{4+}, Nb_{Li}^{5+} after a short-pulse excitation in $LiNbO_3$. *Phys. Rev. B*, 72(24):245108, Dec 2005.

[9] K. Buse. Light-induced charge transport processes in photorefractive crystals I: Models and experimental methods. *Applied Physics B: Lasers and Optics*, 64(3):273–291, 1997.

[10] K. Buse, S. Breer, K. Peithmann, S. Kapphan, M. Gao, and E. Krätzig. Origin of thermal fixing in photorefractive lithium niobate crystals. *Phys. Rev. B*, 56(3):1225–1235, 1997.

[11] J. M. Cabrera, J. Olivares, M. Carrascosa, J. Rams, R. Müller, and E. Diguez. Hydrogen in lithium niobate. *Advances in Physics*, 45(5):349–392, 1996.

[12] K. Olimov, M. Falk, K. Buse, T. Woike, J. Hormes, and H. Modrow. X-ray absorption near edge spectroscopy investigations of valency and lattice occupation site of Fe in highly iron-doped lithium niobate crystals. *J. Phys.: Condens. Matter*, 18:5135–5146, 2006.

[13] Th. Gog, P. Schotters, J. Falta, G. Materlik, and M. Grodzicki. The lattice position of Fe in Fe-doped $LiNbO_3$. *J. Phys. Condens. Matter*, 7:6971–6980, 1995.

[14] L. Rebouta, M. F. Da Silva, J. C. Soares, M. Hage-Ali, J. P. Stoquert, P. Siffert, J. A. Sanz-García, E. Diéguez, and F. Agulló-López. Lattice site of iron in $LiNbO_3$ (Fe^{3+}) by the pixe/channeling technique. *Europhys. Lett.*, 14:557–561, 1991.

[15] M. G. Clark, F. J. DiSalvo, A. M. Glass, and G. E. Peterson. Electronic structure and optical index damage of iron-doped lithium niobate. *J. Chem. Phys.*, 59(12):6209–6219, 1973.

[16] B. Dischler, J. R. Herrington, A. Räuber, and H. Kurz. Correlation of the photorefractive sensitivity in doped $LiNbO_3$ with chemically induced changes in the optical absorption spectra. *Solid State Communications*, 14:1233–1236, 1974.

[17] H. Kurz, E. Krätzig, W. Keune, H. Engelmann, U. Gonser, B. Dischler, and A. Räuber. Photorefractive centers in $LiNbO_3$ studied by optical, Mössbauer and EPR methods. *Appl. Phys,*, 12:355–368, 1977.

[18] M. Falk, J. Japs, T. Woike, and K. Buse. Charge transport in highly iron-doped oxidized lithium niobate single crystals. *Appl. Phys. B*, 87:119–122, 2007.

[19] D. Berben, K. Buse, S. Wevering, P. Herth, M. Imlau, and T. Woike. Lifetime of small polarons in iron-doped lithium niobate crystals. *J. Appl. Phys*, 87(3):1034–1041, 2000.

[20] S. A. Basun, D. R. Evans, T. J. Bunning, S. Guha, J. O. Barnes, G. Cook, and R. S. Meltzer. Optical absorption spectroscopy of Fe^{2+} and Fe^{3+} ions in $LiNbO_3$. *J. Appl. Phys.*, 92(12):7051–7055, 2002.

[21] J. R. Carruthers, I. P. Kaminow, and L. W. Stulz. Diffusion kinetics and optical waveguiding properties of outdiffused layers in lithium niobate and lithium tantalate. *Applied Optics*, 13(10):2333–2342, 1974.

[22] J. L. Jackel, V. Ramaswamy, and S. P. Lyman. Elimination of out-diffused surface guiding in titanium-diffused $LiNbO_3$. *Applied Physics Letters*, 38(7):509–511, 1981.

[23] D. Landheer, D. F. Mitchell, and G. I. Sproule. Secondary ion mass spectrometry and auger study of lithium niobate processing for integrated optics. *J. Vac. Sci. Technol. A*, 4:1897–1900, 1986.

[24] D. P. Birnie III. Analysis of diffusion in lithium niobate. *J. Mat. Sci.*, 28:302–315, 1993.

[25] G. J. Griffiths and R.J. Esdaile. Analysis of titanium diffused planar optical waveguides in lithium niobate. *IEEE Journal of Quantum Electronics*, QE-20(2):149–159, 1984.

[26] D. Kip, B. Gather, H. Bendig, and A. Krätzig. Concentration and refractive index profiles of titanium- and iron-diffused planar $LiNbO_3$ waveguides. *Phys. Stat. Sol. A*, 139:241–248, 1993.

[27] A. I. Bashkirov and V. M. Shandarov. Investigation of optical waveguides obtained in lithium niobate by diffusion of iron. *Zh. Tekh. Fiz.*, 59:66–69, 1989.

[28] M. A. McCoy, S. A. Dregia, and W. E. Lee. Evolution of phases and microstructure in optical waveguides of lithium niobate. *J. Mater. Res.*, 9(8):2040–2050, 1994.

[29] M. A. McCoy, S. A. Dregia, and W. E. Lee. Crystallography of surface nucleation and epitaxial growth of lithium triniobate on congruent lithium niobate. *J. Mater. Res.*, 9(8):2029–2039, 1994.

[30] C. Canali, M. N. Armenise, A. Carnera, M. De Sario, P. Mazzoldi, and G. Celotti. Effects of water vapour on TiO_2, $LiNb_3O_8$ and $(Ti_xNb_{1-x})O_2$ compound kinetics during Ti:$LiNbO_3$ waveguide fabrication. *SPIE Processing of Guided Wave Optoelectronic Materials*, 460:34–41, 1984.

[31] R. Mouras, M. D. Fontana, P. Bourson, and A. V. Postnikov. Lattice site of Mg ion in $LiNbO_3$ crystal determined by Raman spectroscopy. *J. Phys.: Condens. Matter*, 12:5053–5059, 2000.

[32] R. Mouras, P. Bourson, M. D. Fontana, and G. Boulon. Raman spectroscopy as a probe of the rare-earth ions location in $LiNbO_3$ crystals. *Optics Communications*, 196:439–444, 2001.

[33] A. Ridah, P. Bourson, M. D. Fontana, and G. Malovichko. The composition dependence of the Raman spectrum and new assignment of the phonons in $LiNbO_3$. *J. Phys.: Condens. Matter*, 9:9867–9693, 1997.

[34] Y. Zhang, L. Guilbert, P. Bourson, K. Polgár, and M. D. Fontana. Characterization of short-range heterogeneities in sub-congruent lithium niobate by micro-Raman spectroscopy. *J. Phys.: Condens. Matter*, 18:957–963, 2006.

[35] Y. Zhang, L. Guilbert, and P. Bourson. Characterization of Ti:$LiNbO_3$ waveguides by micro-Raman and luminescence spectroscopy. *Appl. Phys. B*, 78:355–361, 2004.

[36] M. Tsirlin and M. Dariel. Some peculiarities of Ti in-diffusion in lithium niobate. *Cryst. Res. Technol.*, 42(7):678–683, 2007.

[37] H. Nagata, T. Sakamoto, H. Honda, J. Ichikawa, E. M. Haga, K. Shima, and N. Haga. Reduced thermal decomposition of OH-free $LiNbO_3$ substrates even in a dry gas atmosphere. *J. Mater. Res.*, 11(8):2085–2091, 1996.

[38] M. Cochez, M. Ferriol, P. Bourson, and M. Aillerie. Influence of the dopant concentration on the OH^- absorption band in Fe-doped $LiNbO_3$ single-crystal fibers. *Optical Materials*, 21:775–781, 2003.

[39] I. Mnushkina. *Properties of lithium niobate*, chapter Iron-doped boules of $LiNbO_3$. INSPEC, The Institution of Electrical Engineers, London, United Kingdom, 2002.

[40] J. P. Nisius and E. Krätzig. Stabilization of Fe^{2+} centers in $LiNbO_3$ waveguides. *Solid State Communications*, 53(9):743–746, 1985.

[41] M. Falk and K. Buse. Thermo-electric method for nearly complete oxidation of highly iron-doped lithium niobate crystals. *Appl. Phys B*, 81(6):853–855, 2005.

[42] D. Kip and J. Hukriede. *Infrared Holography for Optical Communications*, volume 86 of *Topics in Applied Physics*, chapter Holographic reflection filters in photorefractive $LiNbO_3$ channel waveguides. Springer Berlin / Heidelberg, 2003.

[43] B. K. Das, R. Ricken, V. Quiring, H. Suche, and W. Sohler. Distributed feedback - distributed Bragg reflector coupled cavity laser with a Ti:(Fe:)Er:$LiNbO_3$ waveguide. *Optics Letters*, 29(2):165–167, 2004.

[44] R. G. Wilson, F. A. Stevie, and C. W. Magee. *Secondary Ion Mass Spectrometry.* John Wiley & Sons, 1989.

[45] M. H. Yang and R. Odom. Accurate modeling of residual recoil-mixing during SIMS measurements. *Mater. Res. Soc. Symp. Proc*, J4.16:669, 201.

[46] L. C. Feldman and J. W. Mayer. *Fundamentals of surface and thin film analysis.* North Holland eds., 1975.

Acknowledgements

Ringrazio di cuore il mio gruppo per tutto quello che abbiamo fatto insieme ed anche per quello che ho potuto fare da sola.

Ringrazio il mio supervisore per avermi messo a disposizione tutti i mezzi e le risorse per la mia formazione e per la mia attività.

Un grande ringraziamento a chi mi ha aiutato con le misure SIMS: a Cinzia, a Renzo Storti per aver risolto molti problemi e molti dubbi, ad Enrico Napolitani per avermi insegnato moltissimo e aiutato nei momenti critici, al prof. Alberto Carnera.

Je voudrais remercier Sabrina Mignoni, Marc Fontana, Michel Aillerie, Laurent Guilbert, Patrice Bourson, Jean Paul Silvestrini, Rachid Hammoum du Laboratoire Matériaux Optiques, Photonique et Systémes (LMOPS) de Metz, pour la collaboration et pour leur chaleureuse hospitalité.

I miei ringraziamenti vanno inoltre a:

- l'efficientissimo personale della biblioteca del dipartimento di Fisica per avermi procurato moltissimi articoli;
- tutto il personale dell'officina meccanica del dipartimento di Fisica per la loro disponibilità e per aver realizzato i pezzi per il magnetron sputtering;
- Marco Bianconi del CNR di Bologna per le misure RBS;
- Davide De Salvador per le misure PIXE-channeling;
- Daniela Dalla Pellegrina per il lavoro svolto durante la sua tesi di laurea;
- prof. Avashti from New Delhi for Fe ion implantation;
- prof. Shandarov from Tomsk, who kindly sent me his articles;
- prof. Bogomolova from Moscow for EPR measurements;
- Andrius, who grew Fe bulk doped boules;
- Daniele Trinari e Matteo Baldoni per la copertina di questa tesi.

Ringrazio i dottorandi che hanno condiviso con me questi anni: Silvia, Massimo, Anna.

Infine ringrazio Matteo per avermi aiutato a realizzare questa tesi, e per essere il mio più grande estimatore.

List of publications

M. Alonzo, F. Pettazzi, M. Bazzan, N. Argiolas, M. V. Ciampolillo, S. H. Batheni, C. Sada, D. Wolfersberger, A. Petris, V. I. Vlad, E. Fazio, Self-confined beams in erbium-doped lithium niobate. *Jornal of Optics A - Pure and Applied Optics*, **12** (1): 015206, 2010.

S. Mignoni, M. D. Fontana, P. Bourson, M. V. Ciampolillo, M. Bazzan, N. Argiolas, C. Sada, Raman investigation of Fe in-diffused photorefractive waveguides on lithium niobate substrates. *Ferroelectrics*, **390**: 3-9, 2009.

M. V. Ciampolillo, M. Bazzan, C. Sada, N. Argiolas, A. Zaltron, E. Cattaruzza, S. Mignoni, P. Bourson, M. D. Fontana, M. Bianconi, Depth resolved study of the composition and polaron puminescence of Fe:$LiNbO_3$ diffused crystals. *Ferroelectrics*, **389**: 142-152, 2009.

A. Arcangeli D. Parisi, A. Toncelli, M. Tonelli, M. Bazzan, N. Argiolas, M. V. Ciampolillo, C. Sada, Growth and characterization of Er-doped single crystal lithium niobate fibers. *Journal of Applied Optics*, **104**: 103114, 2008.

M. Paturzo, S. Grilli, P. Ferraro, A. Finizio, P. De Natale, N. Argiolas, M. Bazzan, M. V. Ciampolillo, C. Sada, Optical characterization of erbium doped $LiNbO_3$ poling properties. *Journal of Applied Physics*, **104**: 014103, 2008.

C. H. Hou, M. P. Bernal, C. C. Chen, R. Salut, C. Sada, N. Argiolas, M. Bazzan, M. V. Ciampolillo, Purcell effect observation in erbium doped lithium niobate photonic crystal structures. *Optics Communications*, **281**: 4151-4154, 2008.

UNIVERSITÀ DEGLI STUDI DI PADOVA

Scuola di Dottorato in Scienza ed Ingegneria dei Materiali

Padova 11-12-2009

Durante il suo triennio di studi di dottorato la dott.ssa Maria Vittoria Ciampolillo ha svolto un lavoro di ricerca sperimentale dal titolo

Diffusion of iron in lithium niobate

La Dottoranda nel corso dei tre anni ha seguito le attività didattiche previste e si è correttamente sottoposta alle verifiche in itinere.

Il Consiglio Direttivo, dopo aver letto un extended abstract della tesi di dottorato ed aver esaminato il giudizio del Supervisore (dott.ssa Cinzia Sada) giudica positivamente il lavoro svolto e ammette la dottoranda all'esame finale per l'acquisizione del titolo di Dottore di ricerca in Scienza ed Ingegneria dei Materiali.

Il Direttore
Prof. Gaetano Granozzi

Gaetano Granozzi